

Contents

Articles

Summary of the Intercomparison of the Force Standard Machines of the National Institute of Standards and Technology, USA, and the Physikalisch-Technische Bundesanstalt, Germany	Simone L. Yaniv, A. Sawla, and M. Peters	529
Accurate and Precise Coulometric Determination of Sulfur Dioxide in Compressed Gas Mixtures	G. D. Mitchell and A. A. Bell	541
Development of a Coulometric Method for Assessing the Concentration of Ambient Levels of CO ₂ /Air in Compressed Gas Mixtures	G. D. Mitchell and A. A. Bell	547
Certification of NIST SRM 1961: 30 μm Diameter Polystyrene Spheres	Arie W. Hartman, Theodore D. Doiron, and Gary G. Hembree	551
Optimization Techniques for Permittivity and Permeability Determination	Paul D. Domich, James Baker-Jarvis, and Richard G. Geyer	565
Taguchi's Orthogonal Arrays Are Classical Designs of Experiments	Raghu N. Kacker, Eric S. Lagergren, and James J. Filliben	577
A Mathematical Model for Dental Caries: A Coupled Dissolution-Diffusion Process	T. M. Gregory, L. C. Chow, and C. M. Carey	593
<i>Program Report</i> The Advanced Technology Program: A New Role for NIST in Accelerating the Development of Commercially Important Technologies	Brian C. Belanger, George A. Uriano, and Raymond G. Kammer	605
<i>Letter to the Editor</i> A List of New Group Divisible Designs	Kishore Sinha	613
<i>Letter to the Editor</i> Silicon Reference Materials Certified for Isotope Abundances	S. Valkiers, P. De Bièvre, G. Lenaers, and H. S. Peiser	617
<i>Letter to the Editor</i> Slovak Metrological Society	Josef Mandak	621

Conference Reports

Second Industry Workshop on Polymer Composite Processing	S. S. Chang and D. L. Hunston	623
Data Administration Management Association Symposium	Judith Newton	633

News Briefs

GENERAL DEVELOPMENTS	637
NIST Helping in Search for a More Fire-Safe Cigarette Scientists Track Pollutants with Rare Isotope Tags First Labs Accredited for GOSIP Conformance Testing	
1991 Annual Directory of Accredited Labs Available Getting More X-Ray Diagnostic Power Report on U.S./U.S.S.R. Standards Working Group Chemical “Dating Game” Pinpoints Air Emissions Directory of State/Local Lab Programs Published	638
Validated Processor List Now Distributed by NTIS NIST Signs CRADA on Network Management Properties of Materials Program Explained Searching for Brakes and Accelerators in Cancer New Guide Can Help Better Design VAVs	639
New Publication Issued on Transparent File Access Update Planned for Catalog of Code Sets Pyrite Ore Standard Available for Bioprocessors On-Line Technology Help for Small Businesses	640
Eight States to Receive Tech Transfer Planning Grants How to Use Diamond Turning with “Impossible” Metals Researcher Cracks Chemical Mysteries of Coal Proposed Digital Signature Standard Published High-Integrity Software Lecture Series Resumes	641
Antenna Measurement Services Improved New “Users’ Guide” to NIST Available Ion Microscope Helps Map Atoms in Aerospace Alloys NIST, Industry to Propose Coatings Consortium Polymer Composites Processing Sensors Identified	642
NIST Updates Time Services Publication OSI Router Interoperability Testing Performed Electrometer Detects Change in Charge One Ten-Thousandth the Charge of an Electron Coherent Oscillation of Josephson-Junction Array Demonstrated for First Time	643
Automated System Developed for Analyzing Performance of Josephson-Junction Integrated Circuits Algorithms Developed for Estimating Permittivity and Permeability of Materials Sonar Transducer Array Acceptance Tests in NIST Acoustic Anechoic Chamber Radiation Dosimetry for Isotactic Neurosurgery with the Leksell “Gamma-Knife”	644

Modeling of Magnetocaloric Effect in Nanocomposites 645
Research Supports the Department of Defense (DoD) Computer-Aided
Acquisition and Logistic Support (CALs) Program

STANDARD REFERENCE MATERIALS 645
Melt Flow Rate Standard Available for Polymers
Thin-Film Depth Profile Standard Available
New Standards Can Improve Medical Lab Accuracy

Newest Botanical Standards are “Just Peachy” 646
Common Commercial Asbestos Standard, SRM 1866a
Trace Elements in Water, SRM 1643c

Summary of the Intercomparison of the Force Standard Machines of the National Institute of Standards and Technology, USA, and the Physikalisch-Technische Bundesanstalt, Germany

Volume 96

Number 5

September–October 1991

Simone L. Yaniv

National Institute of Standards and Technology,
Gaithersburg, MD 20899 USA

and

A. Sawla and M. Peters

Physikalisch-Technische
Bundesanstalt, Germany

A comparison of force measurements performed at the National Institute of Standards and Technology, USA, and at the Physikalisch-Technische Bundesanstalt, Germany is reported. The focus of the study was the intercomparison of the forces realized by the two Institutes rather than the measurement process. The transfer standards used in the comparison consisted of force transducers and associated readout instrumentation. The results of the intercomparison reveal that over a range of 50 kN to 4.5 MN, the forces realized at NIST and at

PTB compare favorably. For forces up to 900 kN the agreement is within ± 40 ppm; above 900 kN the agreement is within ± 100 ppm.

Key words: deadweight machines; force measurements; force standards; force transducers.

Accepted: July 10, 1991

1. Introduction

This paper summarizes the results of a comparison of force measurements performed at the National Institute of Standards and Technology (NIST), USA, and at the Physikalisch-Technische Bundesanstalt (PTB), Germany. A detailed description of the study can be found in Ref. [1].

The objective of the study was to determine the comparability of the forces realized by the two Institutes over a range of 50 kN to 4.5 MN, so that the results of force transducer calibrations performed at one Institute would be more readily accepted by the other. The need for the comparison was acute as there are significant differences in the force machines used by the two Institutes. At NIST the forces applied are generated by deadweights over the entire range included in the study. At PTB forces up to 1 MN are applied by deadweights but higher forces are generated by means of a hydraulic force-multiplication system.

The overall program for the intercomparison was developed jointly by NIST and PTB. The protocol used during the measurements was developed by PTB. Planning for the program began late in 1988. Initial measurements of all the force transducers involved in the comparison were carried out first at PTB in September 1989. These initial measurements were followed by a set of similar measurements at NIST in October 1989. To verify the stability of the force transducers used during the comparison, a final set of measurements was obtained at PTB in November 1989.

2. Force Standard Machines

The force standard machines of both Institutes have been described in details in Refs. [1-4]. Accordingly, only a brief description of the machines is given here.

2.1 The NIST Deadweight Force Standard Machines

Only the three largest NIST deadweight machines were included in the intercomparison. These machines, known as the 1 Mlbf, the 300 klbf and the 112 klbf machines have been described in Refs. [1,2]. The most important features of these machines are summarized in Table 1. Drawings of the two largest machines are given in Figs. 1 and 2, and a photograph of the 112 klbf machine is given in Fig. 3.

The estimated total uncertainty of the vertical component of force applied by any weight is 0.002 percent. If corrections are made for the actual air density during a calibration and for the actual adjusted mass of each weight, the uncertainty of the applied force can be reduced to 0.001 percent.

The schematic drawing in Fig. 4 illustrates the operating principles of the deadweight machines. Each of the three machines has a stack of large weights, represented by the lower stack of larger weights in Fig. 4. Only the 112 klbf machine also has a second stack of smaller weights that are operated by screw jacks. To apply a deadweight load, the hydraulic jack raises the lifting frame and the loading frame, acting through the device being calibrated in either compression or tension.

As the loading frame is raised, the large weights are picked up in sequence, beginning with the top weight of the stack. In the 112 klbf machine, the smaller weights are lowered onto the loading frame

Table 1. Characteristics of the three largest NIST deadweight machines

Capacity: (nominal)			
kN	4448	1334	498
(klbf)	(1000)	(300)	(112)
Minimum load: (nominal)			
kN	222	44	13
(klbf)	(50)	(10)	(3)
Minimum increment: (nominal)			
kN	222	44	4.4
(klbf)	(50)	(10)	(1)
Time to capacity, s	345	292	274
Compression setup space:			
Vertical, m	1.98	1.65	1.02
Horizontal, m	0.86	0.91	0.71
Tension setup space:			
Vertical, m	4.45	2.49	2.16
Horizontal, m	1.17	0.91	0.71

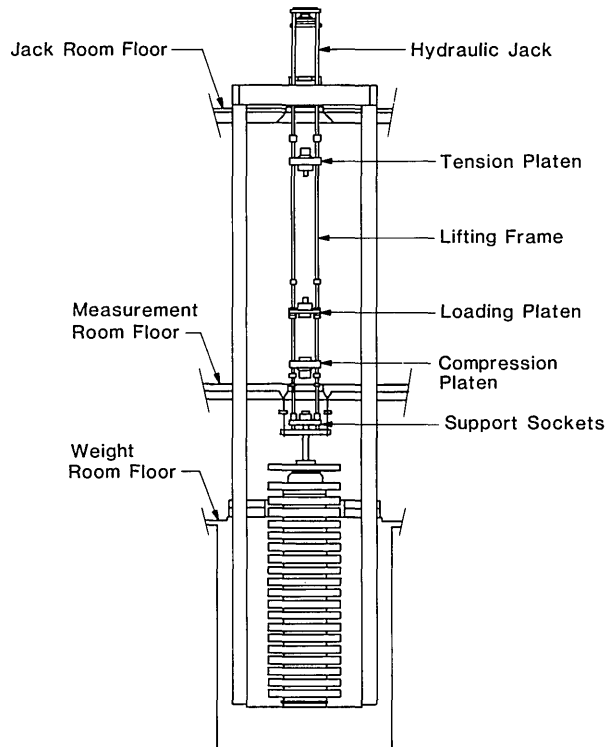


Figure 1. The NIST 1 Mlbf deadweight machine.

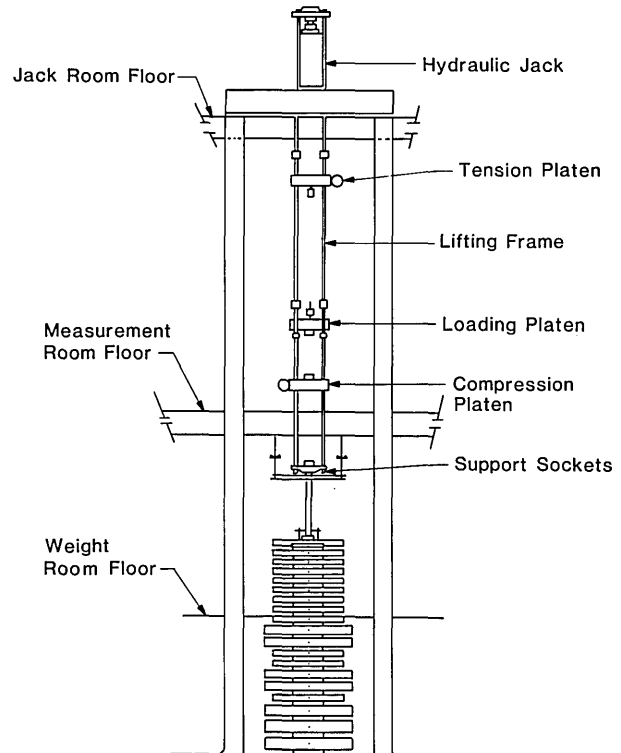


Figure 2. The NIST 300 klbf deadweight machine.

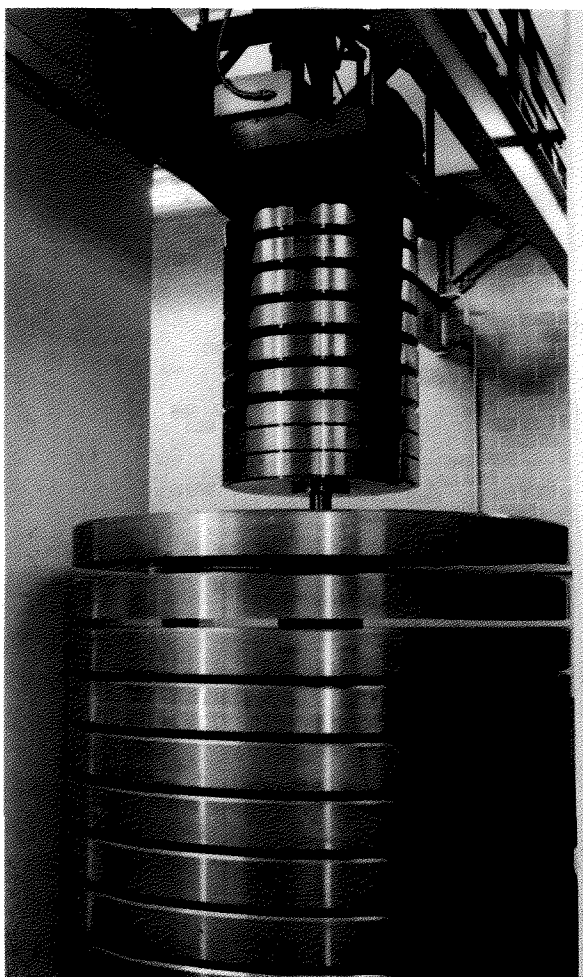


Figure 3. The NIST 112 kbf deadweight machine.

by the screw jacks, in sequence, beginning with the bottom weight of the stack. The time required to apply the capacity load in each machine is given in Table 1. The vertical positions of the compression and tension platens of the lifting frame are adjusted as required to fit each calibration setup. The maximum setup space in each machine is given in Table 1. The safety nuts are adjusted so that they will support the deadweight load if the calibration setup becomes unstable. The vertical members of the loading frames are not clearly visible in Figs. 1 and 2 because the widths of the loading frames are approximately equal to the widths of the respective lifting frames.

2.2 The PTB Force Standard Machines

To cover the force range included in the intercomparison, two PTB force standard machines were utilized. In the first machine, the 1 MN ma-

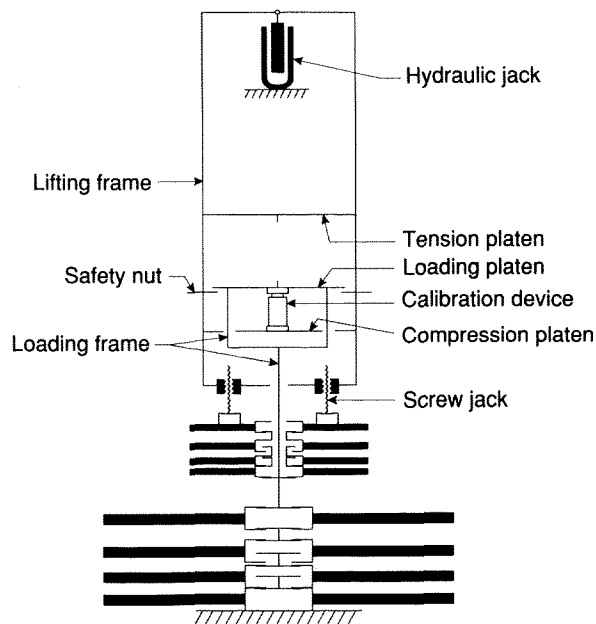


Figure 4. Schematic drawing of the three largest NIST deadweight machines.

chine, forces are generated by deadweights. In the second machine, the 15 MN machine, forces are generated by means of a hydraulic force multiplication system. These machines have been described in detail in Refs. [1,3,4].

A schematic diagram of the 1 MN deadweight machine is shown in Fig. 5. A schematic view of the 15 MN hydraulic force standard machine is shown in Fig. 6.

The overall uncertainty of the force realized in the hydraulic standard force machine has been estimated to be about 100 ppm [5]. The uncertainty of the 1 MN machine is comparable to that of the NIST deadweight machines.

3. Force Transfer Standards

A total of six force transducers were used in the intercomparison. Among these, five force transducers, having capacities of 100 kN, 200 kN, 500 kN, 1 MN, and 5 MN, have been in use at PTB over a substantial period of time. Accordingly, the behavior of these five force transducers is well known as is their long-term stability [1]. The history of the sixth transducer used, the 4.7 MN transducer, is not well documented. A complete description of each transducer can be found in Ref. [1].

To minimize the uncertainty associated with the indicating instrument a high-resolution indicator having a good stability was chosen. The resolution of the selected indicator is 1 ppm.

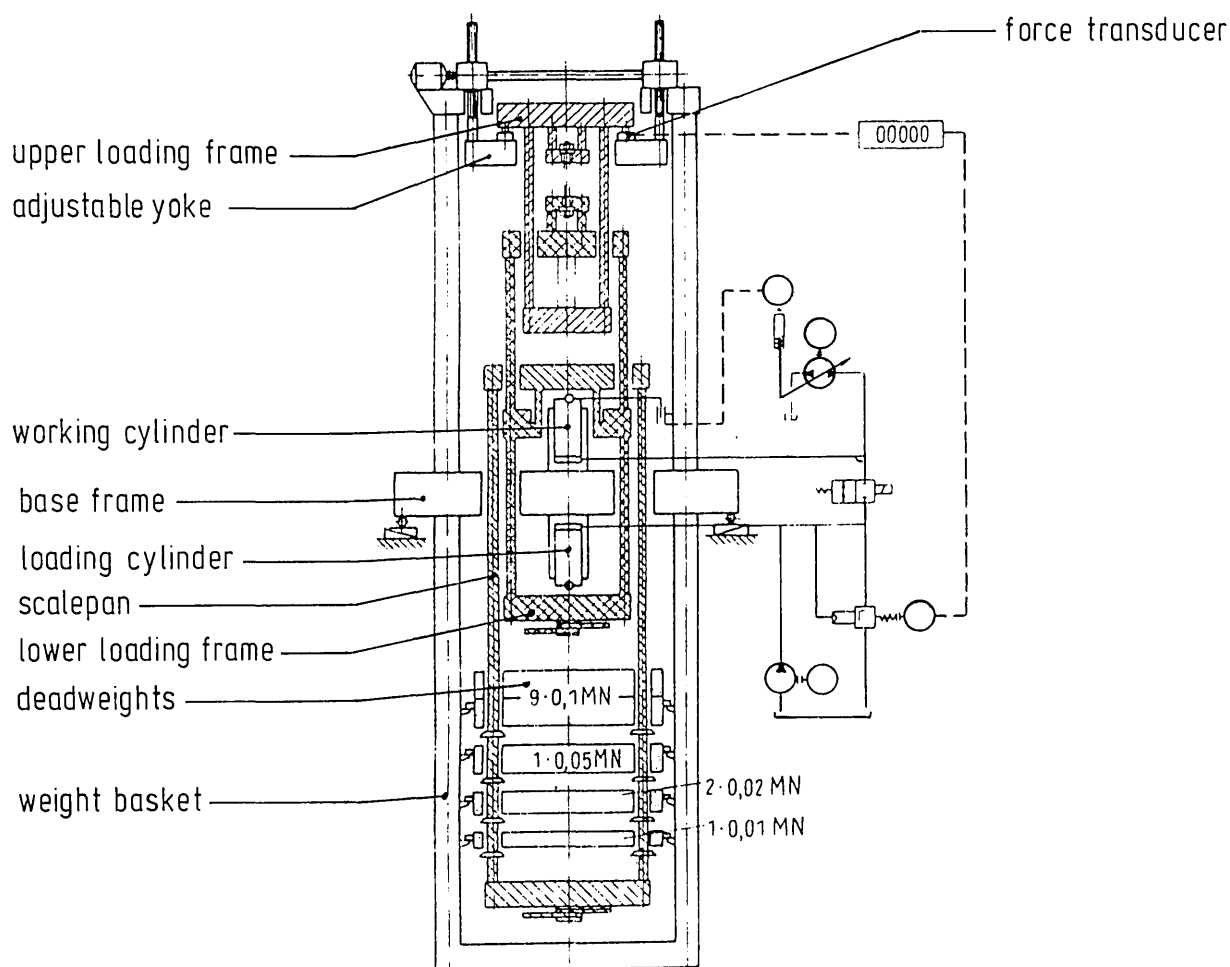


Figure 5. Schematic diagram of the PTB 1MN deadweight machine.

Prior to the start of the intercomparison, measurements were conducted at PTB, using a calibrating standard bridge to ascertain the reliability of the indicator when different main frequencies (50 and 60 Hz in Germany and USA, respectively) and different voltages (220 and 115 V in Germany and USA, respectively) are used. No significant differences were found.

4. Measurement Procedure

In developing the procedure utilized to perform the intercomparison, great care was given to minimize the effects of those parameters that are known to contribute to the measurement uncertainty. The following subsections describes these parameters and the ways in which their effects were minimized.

4.1 Time Interval

The difference between the output of a transducer at a load and its output when no load is applied represents the response of the transducer to that load. When a load is applied to a force transducer or when the force transducer is unloaded, there are initial mechanical, thermal and electrical responses in the various interconnected elements, followed by a delayed creep response or drift in the output of the transducer as the elements approach a new equilibrium condition. The process may be further complicated by local heating due to electrical-power dissipation by the strain-measuring bridge.

Although different force transducers exhibit different creep patterns [6], in general, the creep rate decreases greatly during the first few minutes following loading or unloading. To minimize the effect of creep, for each force transducer included in

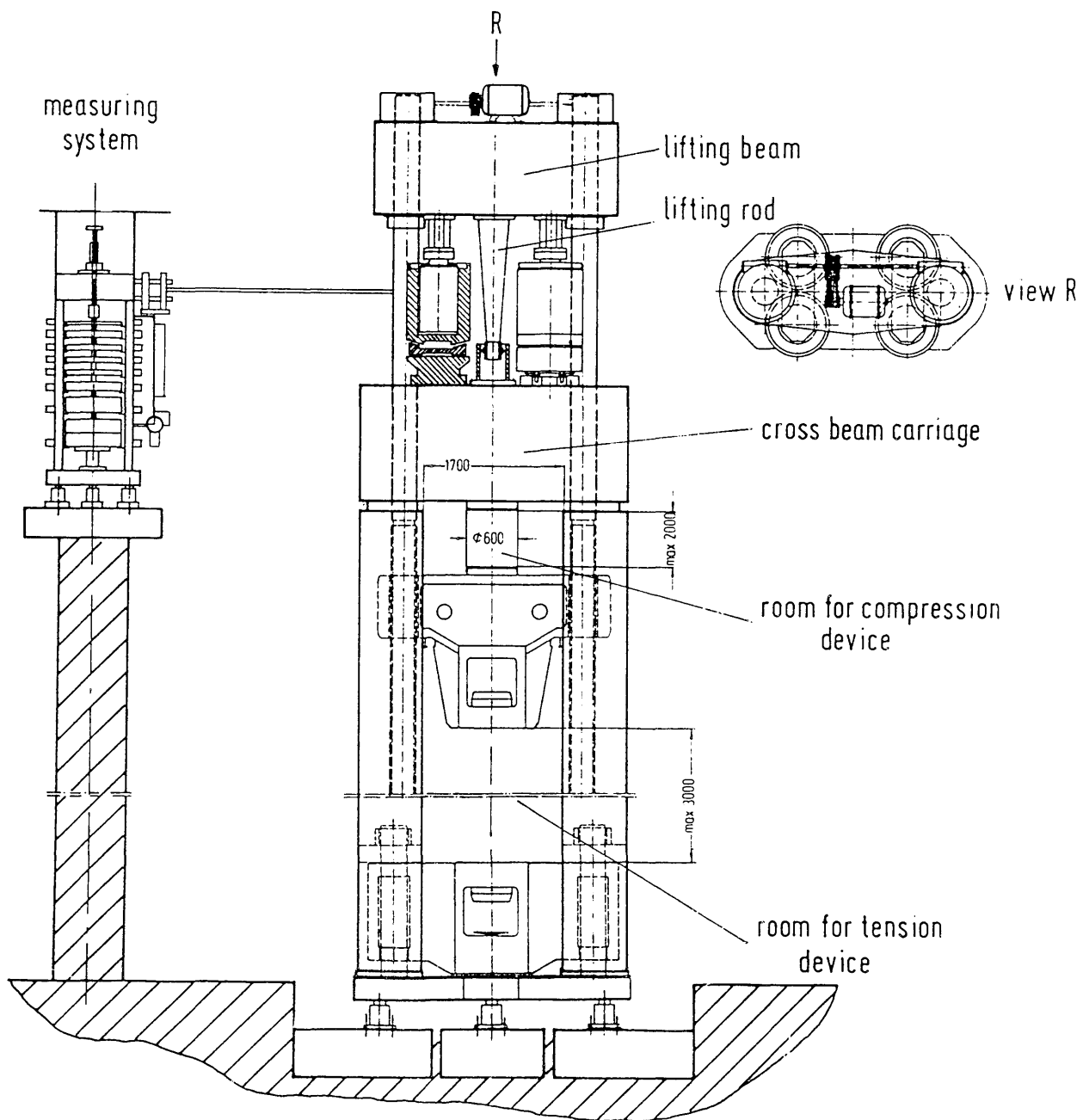


Figure 6. Schematic diagram of the PTB 15 MN hydraulic force standard machine.

the intercomparison, the time required to achieve a stable response following loading and unloading was determined prior to the start of the intercomparison. In most instances it was found that a 3 min time delay between the initiation of the loading (or unloading) and the actual reading was adequate. When tests were conducted in the NIST 300 klf and 1 Mlbf standard machines an additional 1.5

min was allowed to account for the longer loading and unloading times of these very-large deadweight machines.

In each instance, each set of measurements was duplicated once. In all cases a 3 min delay time was introduced between the completion of the initial set of measurements and the initiation of the duplicate set of measurements.

4.2 Machine-Transducer Interaction

Machine-transducer interactions can significantly influence measurement accuracy. Normal imperfections in the alignment of loading machines and force transducers can result in significant bending, shear, and twist components of deformation in the force transducer. To minimize the errors due to these nonaxial components of deformation, it is desirable to sample the response of the force transducer at several symmetrically distributed positions [7,8]. For this reason, the response of each force transducer was obtained at five positions relative to the axis of the machine (0°, 90°, 180°, 270°, 360°).

While at the 0° position and prior to the start of a measurement cycle, the force transducer was exercised by applying the maximum test load three times, returning to zero after each maximum load application. After a 3 min delay, with the force transducer still in the same position, two sets of measurements were obtained, each separated by a 3 min interval. Then, the force transducer was rotated by 90° and two new sets of measurements, each separated by a 3 min interval, were obtained, and so on. A special rotating mechanism, installed underneath the force transducer, allowed the transducer to be rotated rapidly through all the positions. During a measurement cycle (two sets of measurements at five positions) the force transducer was exercised only once at the beginning of the cycle at the 0° position.

4.3 Ambient Conditions

The measurements were carried out at (23±0.5) °C, the usual laboratory conditions at NIST. Normally at PTB the laboratories are maintained at (20±1) °C. However, a week prior to the initiation of the measurements, the temperature of the PTB laboratories was increased to (23±1) °C. Both the force transducers and the indicator were kept at this temperature for a week prior to the initiation of measurements.

4.4 Force Steps

The forces realized in the PTB 15 MN standard machine were compared to the forces realized in the NIST 1 Mlbf deadweight machine. The forces realized in the PTB 1 MN deadweight machine were compared to those realized in the NIST 112 klf, 300 klf, and 1 Mlbf deadweight machines. The loads selected for machine intercomparison

are listed in Tables 2, 3, and 4. Load selection was dictated by the constraints of the force standard machines intercompared, and the following criteria:

1. Limit the measurement range so that no measurements are made below 40% of the force transducer capacity. However, because of the limitation of the machines in some instances data were taken with loads as low as 20%.
2. Use only load sequences that can be applied monotonically;
3. For each force standard machine intercompared, select the same loads.

The following relationship was used to convert pound force to newtons:

$$1 \text{ lbf} = 4.448222 \text{ N.}$$

Table 2. Load chosen to intercompare the PTB 1 MN and the NIST 112 klf standard machines

Force transducer capacity, kN	Selected loads in PTB machine, kN	Selected loads in NIST machine	
		kN	(klbf)
100	50	48.9304	(11)
	100	97.8609	(22)
200	100	102.3091	(23)
	150	151.2395	(34)
	200	200.1700	(45)
500	200	200.1700	(45)
	300	298.0309	(67)
	400	400.3400	(90)
	500	498.2009	(112)

Table 3. Loads chosen to intercompare the PTB 1 MN and the NIST 300 klf standard machines

Force transducer capacity, kN	Selected loads in PTB machine, kN	Selected loads in NIST machine	
		kN	(klbf)
200	90	88.9644	(20)
	130	133.4467	(30)
	180	177.9289	(40)
500	220	222.4111	(50)
	310	311.3755	(70)
	400	400.3400	(90)
1000	410	400.3400	(90)
	540	533.7866	(120)
	670	667.2333	(150)
	800	800.6800	(180)
	930	934.1266	(210)

Table 4. Load chosen to intercompare the PTB 1 MN, 15 MN and the NIST 1 Mlbf standard machines

Force transducer capacity, kN	Selected loads in PTB machine, kN	Selected loads in NIST machine	
		kN	(klbf)
1000	220	222.4111	(50)
	440	444.8222	(100)
	660	667.2333	(150)
	880	889.6444	(200)
4700	900	889.6444	(200)
	1800	1779.2888	(400)
and	2700	2668.9332	(600)
	3600	3558.5776	(800)
5000	4500	4448.2220	(1000)

5. Measurements Results

An effort was made to select for inclusion in the intercomparison similar loads at both PTB and NIST. However, because of machine limitations, the loads actually used, while similar, were significantly different as can be seen in Tables 2 through 4. For this reason, the NIST readings were normalized to correspond to the PTB applied force steps in accordance with the following equation:

NIST normalized indicator reading

$$= \frac{\text{PTB applied force kN}}{\text{NIST applied force kN}}$$

× NIST indicator reading,

where the NIST indicator reading is the net indicator reading obtained by subtracting the zero indicator reading from the reading at load.

5.1 Comparison of Forces in the Range of 50 to 500 kN

Three force transducers having nominal capacities of 100, 200, and 500 kN were used to intercompare, over a range of 50 to 500 kN, the forces realized in the NIST 112 klbf deadweight machine and the forces realized at PTB. The force steps selected for this intercomparison were 50, 100, 150, 200, 300, 400, and 500 kN.

The measurement variability in each series of measurements, at each force step and at each force transducer position, expressed as the relative data spread between runs, is given in Tables 5, 6, and 7 for the 100, 200, and 500 kN force transducers,

Table 5. Relative data spread between runs for the 100 kN force transducer as a function of rotational position: 50 to 500 kN range

Institute	Applied force	Rotational position			
		0° ppm	90° ppm	180° ppm	270° ppm
PTB initial	50 kN	0	6	24	6
	100 kN	2	0	1	4
NIST	11 klbf	4	9	9	8
	22 klbf	4	17	11	6
PTB final	50 kN	14	29	31	5
	100 kN	4	6	2	9

Table 6. Relative data spread between runs for the 200 kN force transducer as a function of rotational position: 50 to 500 kN range

Institute	Applied force	Rotational position			
		0° ppm	90° ppm	180° ppm	270° ppm
PTB initial	100 kN	9	3	7	6
	150 kN	9	3	2	6
	200 kN	15	3	23	5
NIST	23 klbf	21	14	4	47
	34 klbf	8	4	1	5
	45 klbf	9	2	2	14
PTB final	100 kN	12	2	5	5
	150 kN	12	2	18	3
	200 kN	44	11	1	6

Table 7. Relative data spread between runs for the 500 kN force transducer as a function of rotational position: 50 to 500 kN range

Institute	Applied force	Rotational position			
		0° ppm	90° ppm	180° ppm	270° ppm
PTB initial	200 kN	1	4	1	10
	300 kN	8	2	3	7
	400 kN	10	2	1	3
	500 kN	9	1	0	1
NIST	45 klbf	13	1	9	21
	67 klbf	8	18	2	0
	90 klbf	5	7	4	4
	112 klbf	7	3	1	3
PTB final	200 kN	9	6	6	1
	300 kN	5	3	0	4
	400 kN	9	0	1	1
	500 kN	2	2	0	1

respectively. The relative spread between runs was calculated by taking the difference between the first and second readings and dividing the result by the initial reading. Tables 5 through 7 show that, for each force step, the spread in the data, for all measurements performed at both NIST and PTB, is below 50 ppm.

The net mean force transducer outputs measured during the NIST measurements, the initial and final PTB measurements, and those obtained by averaging the initial and final PTB measurements are presented in Table 8. The values in Table 8 are in indicator units.

The relative differences between the average indicator readings at NIST and the corresponding average indicator readings at PTB are listed in Table 9 as a function of force transducer and force step. The values shown in Table 9 were obtained by taking the mean reading at NIST, subtracting from it

the corresponding mean reading at PTB, and then dividing the result by the corresponding mean value of initial and final PTB readings. The values shown are rounded to the nearest ppm.

The average deviations in the mean PTB data relative to the mean NIST data for all force transducers and force steps examined (i.e., last column in Table 9) are given in Fig. 7. Figure 7 shows that the agreement between the data obtained at NIST and PTB is excellent. The deviations fall within a band ranging from -31 to 12 ppm.

5.2 Comparison of Forces in the Range of 90 kN to 1MN

Three force transducers having nominal capacities of 200 kN, 500 kN, and 1 MN were used to intercompare, over a range of 90 kN to 1 MN, the forces realized in the NIST 300 kN deadweight machine and the forces realized at PTB. The force steps selected for this intercomparison were 90, 130, 180, 220, 310, 400, 410, 540, 670, 800, and 930 kN. When the program was planned originally, it was not anticipated that the 90, 130, and 180 kN force steps would be included in this subset of intercomparison. Accordingly, the first series of measurements performed at PTB did not include measurements for these force steps.

The measurement variability in each series of measurements, at each force step and each force transducer position, expressed as the relative data spread between runs, is given in Tables 10, 11, and 12 for the 200 kN, 500 kN, and 1 MN force transducers, respectively. The relative spread between

Table 8. Force transducer outputs measured at NIST and PTB: 50 to 500 kN range

Transducer kN	Force step kN	PTB initial	PTB final	PTB mean	NIST
100	50	1.069592	1.069593	1.069593	1.069559
	100	2.137819	2.137841	2.137830	2.137778
200	100	0.999438	0.999449	0.999444	0.999440
	150	1.499222	1.499257	1.499240	1.499246
	200	1.999049	1.999081	1.999065	1.999087
500	200	0.799180	0.799230	0.799205	0.799214
	300	1.198875	1.198944	1.198909	1.198908
	400	1.598594	1.598667	1.598630	1.598628
	500	1.998344	1.998420	1.998382	1.998382

Table 9. Relative differences between the NIST and PTB mean readings for the force transducer tested in the 112 kN deadweight machine

Transducer kN	Force step kN	PTB initial ppm	PTB final ppm	PTB mean ppm
100	50	-31	-32	-31
	100	-19	-29	-24
200	100	2	-10	-4
	150	16	-8	4
	200	19	3	11
500	200	43	-19	12
	300	28	-30	-1
	400	21	-24	-1
	500	19	-19	0

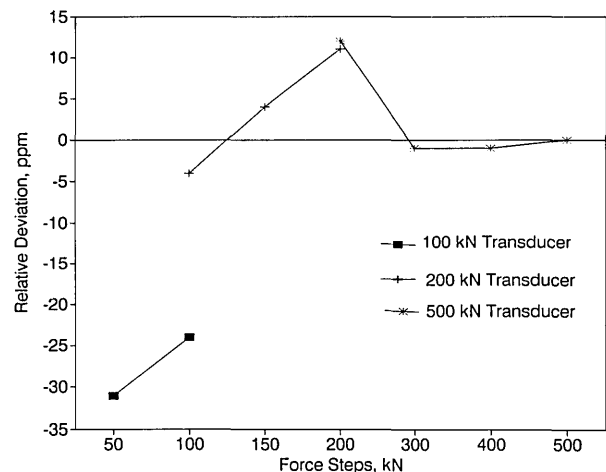


Figure 7. Deviations in the mean PTB data relative to the mean NIST data for the 50 to 500 kN range.

Table 10. Relative data spread between runs for the 200 kN force transducer as a function of rotational position: 90 kN to 1 MN range

Institute	Applied force	Rotational position			
		0° ppm	90° ppm	180° ppm	270° ppm
PTB final	90 kN	3	11	6	23
	130 kN	21	8	3	8
	180 kN	1	13	3	2
NIST	20 klb	0	1	3	3
	30 klb	6	4	1	4
	40 klb	11	4	2	1

Table 11. Relative data spread between runs for the 500 kN force transducer as a function of rotational position: 90 kN to 1 MN range

Institute	Applied force	Rotational position			
		0° ppm	90° ppm	180° ppm	270° ppm
PTB initial	220 kN	5	5	1	16
	310 kN	9	2	10	13
	400 kN	1	1	13	9
NIST	50 klb	0	4	4	4
	70 klb	2	3	5	5
	90 klb	5	10	2	4
PTB final	220 kN	2	1	3	6
	310 kN	2	6	2	2
	400 kN	6	1	3	1

Table 12. Relative data spread between runs for the 1 MN force transducer as a function of rotational position: 90 kN to 1 MN range

Institute	Applied force	Rotational position			
		0° ppm	90° ppm	180° ppm	270° ppm
PTB initial	410 kN	2	17	0	0
	540 kN	3	25	25	31
	670 kN	3	9	2	10
	800 kN	1	10	2	4
	930 kN	3	2	2	6
NIST	90 klb	5	27	5	20
	120 klb	0	7	2	2
	150 klb	4	0	3	2
	180 klb	5	1	1	4
	210 klb	2	4	4	5
PTB final	410 kN	2	0	1	6
	540 kN	12	8	1	4
	670 kN	2	8	7	4
	800 kN	10	4	2	1
	930 kN	13	8	4	2

runs was calculated by taking the difference between the first and second readings and dividing the result by the initial reading. Tables 10 through 12 show that, for each force step, the spread of the data is below 35 ppm for all measurements performed at both PTB and NIST.

The net mean force transducer outputs measured during the NIST measurements, the initial and final PTB measurements, and those obtained by averaging the initial and final PTB measurements are presented in Table 13. The values shown are in indicator units.

The relative differences between the average indicator readings at NIST and the corresponding readings at PTB are listed in Table 14 as a function of force transducer and force step. The values shown in Table 14 were obtained as described in Sec. 5.1 except that, for the 200 kN force transducer, the values shown were obtained by taking the mean reading at NIST, subtracting from it the corresponding mean final PTB reading, and dividing the result by the mean final PTB reading. All the values in Table 14 were rounded to the nearest ppm.

When evaluating the differences in the forces realized at PTB and NIST in the range between 220 and 400 kN, that is the forces determined using the 500 kN force transducer, only the relative differences between NIST and the final PTB data are meaningful because the initial set of measurements obtained at PTB were found to contain systematic errors. This is the reason why the decision was

Table 13. Force transducer outputs measured at NIST and PTB: 90 kN to 1 MN range

Transducer kN	Force step kN	PTB initial	PTB final	PTB mean	NIST
200 ^a	90		0.899500		0.899500
	130		1.299331		1.299366
	180		1.799171		1.799204
500 ^b	220	0.879081	0.879165	0.879123	0.879184
	310	1.238808	1.238898	1.238853	1.238927
	400	1.598538	1.598644	1.598591	1.598666
1000	410	0.835596	0.835609	0.835602	0.835623
	540	1.100592	1.100621	1.100607	1.100618
	670	1.365630	1.365669	1.365649	1.365654
	800	1.630647	1.630694	1.630670	1.630684
	930	1.895624	1.895674	1.895649	1.895656

^a No initial PTB measurements were taken with this transducer.

^b Initial PTB measurements contained systematic errors and should not be used to intercompare the forces achieved in the NIST 300 klb deadweight machine with those achieved at PTB.

Table 14. Relative differences between NIST and PTB readings for the force transducers tested in the 300 klbf deadweight machine

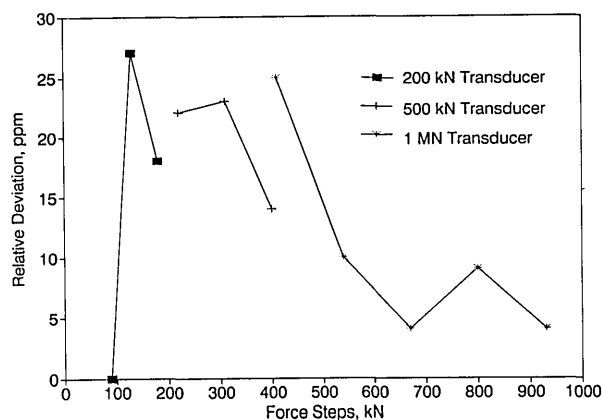
Transducer kN	Force step kN	PTB initial ppm	PTB final ppm	PTB mean ppm
200 ^a	90		0	
	130		27	
	180		18	
500 ^b	220	117	22	69
	310	96	23	60
	400	80	14	47
1000	410	32	17	25
	540	24	-3	10
	670	18	-11	4
	800	23	-6	9
	930	17	-9	4

^a No initial PTB measurements were taken with this transducer.

^b Initial PTB measurements contained systematic errors and should not be used to intercompare the forces achieved in the NIST 300 klbf deadweight machine with those achieved at PTB.

made to include the 200 kN force transducer in the set of force transducers measured in NIST 300 klbf deadweight machine.

The average deviations in the mean PTB data relative to the mean NIST data for all force steps and all force transducers included in the 90 kN through the 1 MN range are shown in Fig. 8. For both the 200 and 500 kN force transducers, the values shown are based on the final PTB measurements only. The data shown for the 1 MN transducer are based on both the initial and final PTB measurements. Figure 8 shows that the agreement between the data obtained at NIST and PTB is very good. The deviations fall within a band from 0 to 30 ppm.

**Figure 8.** Deviations in the mean PTB data relative to the mean NIST data for the 90 to 1 MN range.

5.3 Comparison of Forces in the Range of 220 to 4500 kN

Three force transducers having nominal capacities of 1, 4.7, and 5 MN were used to intercompare, over a range of 220 to 4500 kN, the forces realized in the NIST 1 Mlbf machine and (a) the forces realized in the 1 MN PTB deadweight machine, and, (b) for forces above 1 MN, those achieved in the 15 MN PTB hydraulic multiplication standard machine. The force steps selected for this intercomparison were 220, 440, 660, 880, 900, 1800, 2700, 3600, and 4500 kN.

The measurement variability in each series of measurements, at each force step and at each force transducer position, expressed as the relative data spread between runs, is given in Tables 15, 16, and 17 for the 1, 4.7, and 5 MN force transducers, respectively. The relative spread between runs was calculated in accordance with the procedure described in Sec. 5.1. Tables 15 through 17 show that for the 1 MN force transducer the largest spread, 57 ppm, was obtained at NIST at the 50 klbf force step. With the other two transducers, the largest spread was obtained at PTB with the maximum, 240 ppm, occurring with the 5 MN transducer at the 900 kN force step.

The net mean force transducer outputs measured at NIST and at PTB, and those obtained by averaging the initial and final PTB values are shown in Table 18. The values are in indicator units.

The relative differences between the average indicator readings at NIST and the corresponding average indicator readings at PTB are listed in Table 19 as function of force transducer and force step.

Table 15. Relative data spread between runs for the 1 MN force transducer as a function of rotational position: 220 to 880 kN range

Institute	Applied force	Rotational position			
		0° ppm	90° ppm	180° ppm	270° ppm
PTB initial	220 kN	4	2	13	7
	440 kN	3	11	10	8
	660 kN	16	5	8	5
	880 kN	3	3	2	1
NIST	50 klbf	31	51	53	57
	100 klbf	17	19	19	13
	150 klbf	4	1	9	25
	200 klbf	4	0	14	9
PTB final	220 kN	0	4	9	27
	440 kN	2	4	4	7
	660 kN	1	11	9	1
	880 kN	5	6	7	0

Table 16. Relative data spread between runs for the 4.7 MN force transducer as a function of rotational position

Institute	Applied force	Rotational position			
		0° ppm	90° ppm	180° ppm	270° ppm
PTB initial	900 kN	95	54	27	27
	1800 kN	48	34	27	14
	2700 kN	64	130	140	27
	3600 kN	37	58	51	20
	4500 kN	35	38	44	14
NIST	200 klbf	25	33	39	33
	400 klbf	17	29	25	18
	600 klbf	34	2	6	6
	800 klbf	28	6	2	2
	1000 klbf	32	8	0	5
PTB final	900 kN	27	110	68	95
	1800 kN	0	14	48	0
	2700 kN	0	59	23	32
	3600 kN	7	37	10	24
	4500 kN	3	16	22	38

Table 17. Relative data spread between runs for the 5 MN force transducer as a function of rotational position

Institute	Applied force	Rotational position			
		0° ppm	90° ppm	180° ppm	270° ppm
PTB initial	900 kN	81	90	18	27
	1800 kN	4	27	13	27
	2700 kN	6	42	15	18
	3600 kN	20	2	20	16
	4500 kN	14	29	7	13
NIST	200 klbf	11	38	42	82
	400 klbf	33	25	25	25
	600 klbf	1	51	1	16
	800 klbf	0	37	28	1
	1000 klbf	12	29	29	14
PTB final	900 kN	110	54	170	240
	1800 kN	0	130	9	130
	2700 kN	99	27	110	99
	3600 kN	36	72	83	130
	4500 kN	23	23	63	22

The values shown were obtained in accordance with the procedure given in Sec. 5.1. All values shown in the table were rounded to the nearest ppm. Table 19 shows that overall there was good agreement between the data obtained at PTB and NIST. However, the response of the largest two transducers drifted somewhat during the course of the intercomparison. This drift was most significant with the 5 MN force transducer.

Table 18. Force transducer outputs measured at NIST and PTB: 220 to 4500 kN range

Transducer MN	Force step kN	PTB initial	PTB final	PTB mean	NIST
1	220	0.448320	0.448304	0.448312	0.448302
	440	0.896749	0.896739	0.896744	0.896757
	660	1.345272	1.345269	1.345270	1.345285
	880	1.793741	1.793745	1.793743	1.793748
4.7	900	0.557929	0.557866	0.557898	0.557926
	1800	1.115960	1.115896	1.115928	1.115971
	2700	1.673944	1.674003	1.673974	1.673927
	3600	2.231629	2.231759	2.231694	2.231717
5	4500	2.789248	2.789319	2.789284	2.789406
	900	0.367344	0.367306	0.367325	0.367351
	1800	0.734166	0.734051	0.734108	0.734212
	2700	1.101155	1.100933	1.101044	1.101248
	3600	1.468967	1.468721	1.468844	1.469005
	4500	1.837706	1.837474	1.837590	1.837671

Table 19. Relative differences between the NIST and PTB readings for the force transducers tested in the 1 Mlbf dead-weight machine

Transducer MN	Force step kN	PTB initial ppm	PTB final ppm	PTB mean ppm
1	220	-40	-5	-23
	440	9	20	14
	660	10	12	11
	880	4	2	3
4.7	900	-5	110	51
	1800	10	68	39
	2700	-11	-46	-28
	3600	40	-19	10
5	4500	57	31	44
	900	17	120	69
	1800	63	220	140
	2700	84	290	190
	3600	26	190	110
	4500	-19	110	44

The average deviations in the mean PTB data relative to the mean NIST data for the 1 and 4.7 MN force transducers and force steps examined are shown in Fig. 9. Because of the drift observed in the 5 MN force transducer, the results obtained with this transducer were not included in the generation of Fig. 9. The average deviations fall within a band from -30 to 50 ppm.

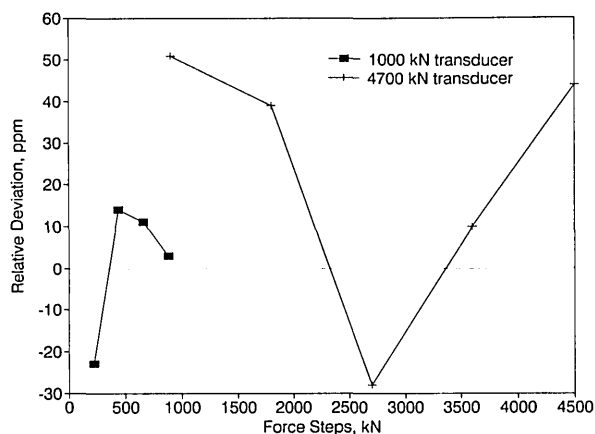


Figure 9. Deviations in the mean PTB data relative to the mean NIST data for the 220 kN to 4.5 MN range.

6. Conclusions

Over a range of 50 to 4500 kN, the forces realized in the NIST deadweight machines compare favorably with those realized at PTB. Comparison of forces up to 900 kN indicate that the forces realized in the NIST deadweight machines and the forces realized in the PTB 1 MN deadweight machines agree within ± 40 ppm. Peters et al. [7] have reported that theoretically the uncertainty in the forces realized by deadweight force machines is on the order of ± 20 ppm. Accordingly, for the 50 to 900 kN force range, the agreement between the forces realized at NIST and PTB is close to what is theoretically achievable.

Comparison of forces in the range of 1 to 4.5 MN indicate that the forces realized in the PTB hydraulic force multiplication system compare favorably with the forces realized in the NIST deadweight machines. In this range, the agreement between the PTB data and the NIST data is within ± 100 ppm, a remarkable agreement considering that the uncertainty of hydraulic force standard machine is inherently greater than that associated with deadweight machines.

7. References

- [1] A. Sawla, M. Peters, S. L. Yaniv, and R. A. Mitchell, Inter-comparison of Force Standard Machines of the National Institute of Standards and Technology, USA, and the Physikalisch-Technische Bundesanstalt, Braunschweig, Germany, PTB-Bericht MA-20 (1991).
- [2] R. A. Mitchell, Force Calibration at the National Bureau of Standards, NBS Technical Note 1227, U.S. Department of Commerce, Gaithersburg MD (1986).

- [3] W. Weiler, M. Peters, H. Gassmann, H. Fricke, and W. Ackerschott, Die 1-MN-Kraft-NormalmeBeinrichtung der PTB Braunschweig, VDI-Z, 120, 1-6 (1978).
- [4] W. Weiler, A. Sawla, and M. Peters, Design and Calibration Problems of the 15 MN Hydraulic Force Standard Machine, VDI-Bericht 212 (1974).
- [5] M. Peters and W. Weiler, Zur Kalibrierung der 15-MN-Kraft-NormalmeBeinrichtung der Physikalisch-Technischen bundesanstalt, PTB-Mitt 83 (1973).
- [6] R. A. Mitchell and S. M. Baker, Characterizing the Creep Response of Load Cells, VDI-Berichte 312 (1978).
- [7] M. Peters, A. Sawla, and D. Peschel, Uncertainty in Force Measurement, Report of the CCM Working Group Force, PTB-Bericht MA-17 (1990).
- [8] P. E. Pontius and R. A. Mitchell, Inherent Problems in Force Measurement, *Exper. Mech.* 22, 81-88 (1982).

About the authors: Simone L. Yaniv is a physical scientist in charge of the Force Group in the NIST Manufacturing Engineering Laboratory. M. Peters is in charge of the PTB Force Laboratory in Braunschweig, Germany where A. Sawla is a senior researcher.

Accurate and Precise Coulometric Determination of Sulfur Dioxide in Compressed Gas Mixtures

Volume 96

Number 5

September-October 1991

**G. D. Mitchell and
A. A. Bell**

National Institute of Standards
and Technology,
Gaithersburg, MD 20899

Coulometry has been established as an important and reliable method for the determination of acidic compounds. The analytical method and simple apparatus described here are applied to the precise and accurate determination of sulfur dioxide in nitrogen, specifically in compressed gas cylinders at nominal concentrations of 50 and 100 $\mu\text{mol/mol}$ (ppm). This method is constant current coulometry where the magnitude of the current is set by the balance between

the electrochemical generation of OH^- , the flow of SO_2 , and the chemical reaction of the solution. The method is direct, rapid, and can be refined further to provide analysis at the nanomol/mol level.

Key words: acid rain; analysis of gases; compressed gas; coulometry; sulfur dioxide.

Accepted: July 10, 1991

1. Introduction

Sulfur dioxide (SO_2) in the atmosphere is a common pollutant and is a major contributor to the formation of acid rain. Accurate and precise determinations of SO_2 in the atmosphere are essential to determine the magnitude of the problem. Reference gas mixtures such as NIST SRMs are an important part of the measurement procedure. The method presented here is intended for the analysis of cylinder gas mixtures of SO_2 in nitrogen. The determination of SO_2 has been accomplished by a variety of techniques [1,2,3,4,5,6,7]. Most of the methods are time consuming, employ expensive instrumentation, and need sample pretreatment. The coulometric titration method described here, for the determination of SO_2 in compressed gas mixtures of SO_2/N_2 , is sensitive, requires a modest investment in instrumentation, is applicable to other reactive gases, and under explicit experimental conditions is independent of calibration standards.

The accuracy of constant current coulometry is dependent upon several factors: the Faraday, elec-

trode processes, electrode kinetic parameters, and the current efficiencies. These critical factors and their importance in coulometry are discussed in detail in Ref. [7]. The coulometric determination of strong acids or bases most nearly approaches the ideal measurement situation [8,9,10] in aqueous media completely free of reactive impurities. However, no matter what the working conditions are, at least one secondary reaction occurs in competition with the desired electrode reaction, even though it may be very slight. The current efficiency is thereby, in the limit, set by the relative rate of the desired electrode reaction and the competing background electrode processes. The goal in constant current coulometry is therefore to characterize the current efficiency under specific experimental conditions, thus delineating any systematic bias associated with the method.

Calibration mixtures of SO_2 in N_2 in compressed gas cylinders are generally characterized by using precise instrumental techniques that have been

calibrated with accurately prepared standards, or with standards that have been characterized using independent reference methods. The reference method for SO₂ analysis is acid-base titration accomplished by the absorption of SO₂ gas by a solution of hydrogen peroxide (H₂O₂) followed by the titration of the resultant H₂SO₄ with a standard base [11]. The method, however, has three inherent sources of error: 1) the measurement of the volume of gas mixture passed through the absorbing solution, 2) the accuracy associated with the standard base, and 3) the imprecision of titration. To overcome these limitations, a coulometric based titration system with optical detection has been developed.

The coulometric method described here provides experimental data that are directly related to the Faraday constant. To evaluate the accuracy of the method, it is necessary to evaluate the various aspects of the overall approach. The three criteria that define the approach are:

- a quantitative reaction scheme for SO₂
- accurate SO₂ sample delivery
- an independent determination of the current efficiency.

The reaction scheme selected for the coulometric determination of SO₂/N₂ is analogous to that used by the Peroxide Method [11]. The coulometry-based acid-base neutralization is accompanied by both complete absorption of the analyte and near 100% current efficiency.

2. Experimental Methods

2.1 Reagents

All solutions are prepared from reagent grade materials and distilled H₂O that has been passed through an adsorption/ion exchange filtration process. The absorption solution is prepared by dissolving 20 g of KCl in water and adding 5 mL of 30% hydrogen peroxide and 25 mL of a bromocresol green solution (0.1% by volume), followed by dilution to 1 L. The pH of the solution is adjusted to 4.0 by the addition of 1% hydrochloric acid, if needed. A 2% KCl solution adjusted to a pH of 4.0 was prepared for the anode compartment of the electrochemical cell. The cell compartments are separated by a sintered glass disc and a 3% KCl-Agar plug.

2.2 Apparatus

The coulometric system consists of essentially three components: a reaction chamber (the cell), an absorption solution, and an amplified photometric feedback circuit for end-point detection. The reaction chamber is an "H-base" glass cell with two electrode compartments separated by a glass frit and a salt-agar bridge (Fig. 1). The hydrogen peroxide absorption solution contains a pH indicator and the electrolyte. Detection of the coulometric titration end-point is achieved through a current feedback circuit. The feedback current to the working electrode is supplied by the optical detection system which consists of photodiodes and interference filters. The method calls for a silver rod anode (7 mm diameter, 100 mm length) and a platinum cathode with 2 cm² surface area. The cathode compartment is 31 mm in diameter and 95 mm in height. The compartment contains two windows 15 mm in diameter for use with the optical detection system. The compartment is fitted with a rubber stopper through which the platinum electrode and a gas delivery tube are inserted. The anode compartment, 95 mm in height and 25 mm in diameter, contains the silver rod electrode and the 2% KCl electrolyte solution. The cathode and anode compartments are filled approximately 50 mm above their bases with the absorption solution and the 2% KCl electrolyte, respectively.

The dc amplifier circuit [12] operates by using the output signal from the photodiode detectors as a titration current through a feedback loop. The system is powered by a 15 V regulated power supply. An auto-ranging DVM with an IEEE interface is used to monitor the current output from the titration cell.

A mass flow controller (MFC) capable of measuring gas flow rates up to 100.0 ± 0.1 mL/min is used. The MFC is periodically calibrated using a wet test meter that has been calibrated by gravimetry.

A three-way solenoid valve is used to direct the flow of sample gas or zero gas (N₂) through the reaction cell.

A 10 turn potentiometer is used to control the nulling circuit, which balances the detectors for ambient light conditions. An on/off switch empowers the detector light source.

The optical system consists of two 620 nm interference filters, two photodiodes, a single biconvex glass lens, and a dc lamp, all mounted on an optical bench.

The entire system is controlled by a computer.

- A. Platinum Electrode
- B. Gas Inlet Tube
- C. Vent
- D. Agar Gel
- E. Glass Frit
- F. Silver Electrode
- G. Optical Windows
- H. Glass Cell

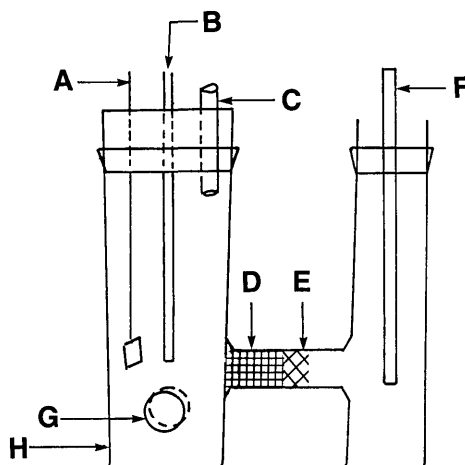


Figure 1. Coulometric titration cell.

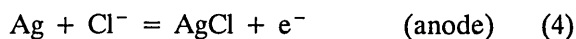
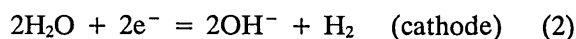
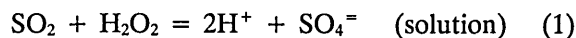
2.3 Procedure

The absorption cell compartments are filled with the appropriate solutions. The cell is placed in the optical system (Fig. 2) so that the light from the lamp strikes the cell at the window and passes through the absorption solution without any obstructions. The appropriate connections are made to the gas inlet tube, and to the anode and cathode of the cell. The cover is placed over the cell to eliminate as much background light as possible. The current flow is adjusted to zero using the nulling potentiometer and SO_2 -free zero gas (N_2) is allowed to flow through the cell. At this point the system is ready, and the entire analysis can be controlled by the computer.

The computer is interfaced to a current meter in series with the cell and a printer. The computer control is a menu driven central utility program that not only controls the experiment, but also has data reduction capabilities. The Central Control program is selected, all necessary parameters are specified (date, cylinder identification, barometric pressure, temperature, type of analysis (SO_2), estimated concentration, flow rate of gas, number of replicates, and the disk storage file) and the program is started. The computer energizes a solenoid, thus selecting the analyte gas mixture. During the analysis, time (min) and current (mA) are stored in the run file at 30 s intervals for 15 min. At the end of 15 min, the program collects 200 current readings of the cell in a 2 min interval and reports the mean value as the cell current. The solenoid is de-energized and nitrogen gas is passed through the cell, decreasing the cell current to a

predetermined level, where the software either replicates or ends the analysis.

The method described for the determination of $\text{SO}_2(\text{g})$ in a N_2 matrix is based on the following series of reactions:



Sulfur dioxide reacts with the hydrogen peroxide to form sulfuric acid. The acid causes a change in the color of the indicator in the absorption solution, thus bringing about a change in the electronic null circuit. The shift in pH and color of the absorption solution causes an increase in the amount of light striking a photodiode detector whose output is fed back to the cell as a titration current. At the cathode, hydroxide is produced to neutralize the acid formed in reaction [1]. The rate of formation of hydroxide at the cathode is equivalent to the rate of formation of the sulfuric acid. At steady state the current is proportional to the original SO_2 concentration of the sample gas. The accuracy of the entire process is dependent upon two factors 1) stoichiometric conversion of SO_2 to H_2SO_4 and 2) near 100% current efficiency.

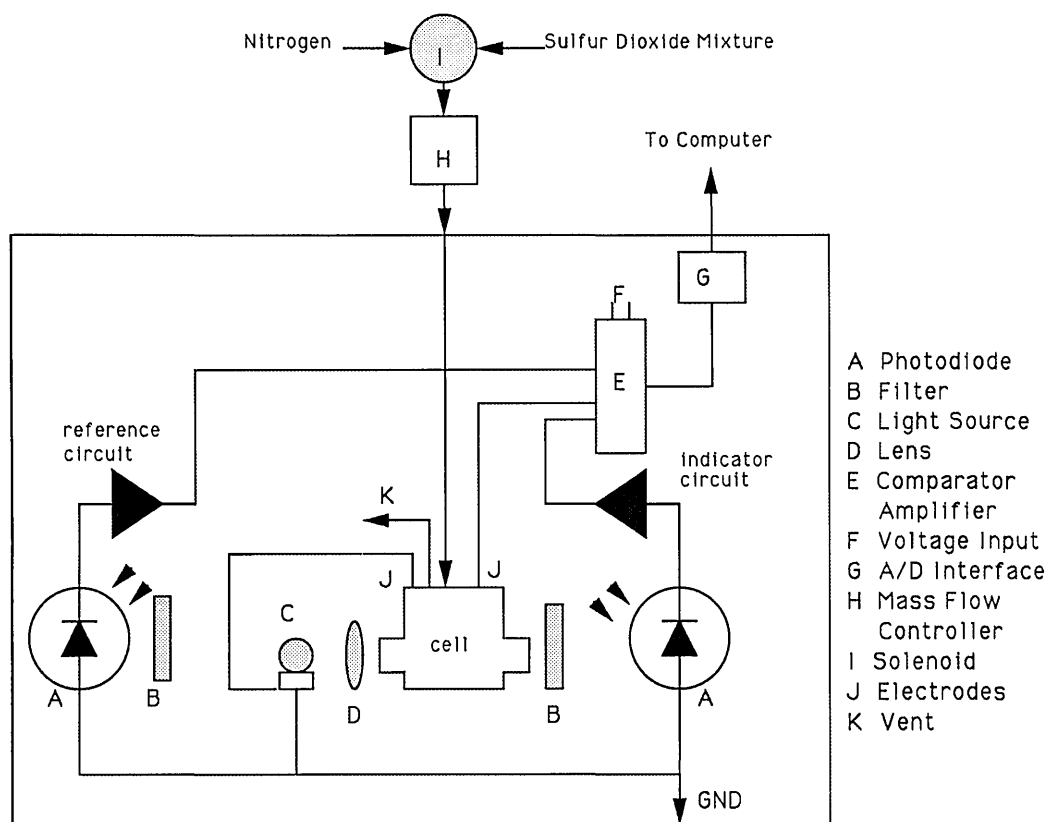


Figure 2. Diagram for apparatus.

3. Results and Discussion

The absorption efficiency of SO₂ in 1.5% H₂O₂ was determined during "wet chemistry" titration using the reference method [11]. Using dual impingers arranged in series, 15 L of 100 ppm SO₂/N₂, at a flow rate of 1 L/min, were passed through the two impingers, each containing 20 mL of 1.5% H₂O₂. Analysis of the contents of the first impinger showed that the amount of SO₂ in the flowing stream was 100 ppm. A titration of the contents of the second impinger revealed no H₂SO₄, which means that all of the SO₂ was absorbed in the first impinger. In this system the sample gas flows at a rate of 50 mL/min for about 15 min, which amounts to less than 1 L of SO₂/N₂ mixture per determination. The working electrode compartment of the cell (Fig. 1) is similar to the impingers used for the absorption studies.

Current efficiency studies were performed using a permeation tube calibration system consisting of a thermostatically-controlled chamber containing a gravimetrically-calibrated SO₂ permeation device and a calibrated mass flow controller. The calibrated permeation tube serves as an accurate

and independent source of SO₂ gas. From the known output of the permeation tube and calibrated flow of dry N₂ or air over it, concentrations of SO₂ are obtained with an uncertainty of 0.5%. The results of the current efficiency study are summarized in Table 1. Many factors contribute to inaccuracies in the generation and measurement of standards. These include: 1) a bias in the current measurement, 2) a bias in the critical components of the electronic circuit, 3) the interference of a competing background reaction, and 4) the imprecision of the dynamic dilution system. Based on the result presented in Table 1, the current efficiency is considered to be 101.1 ± 0.6%, within the limit of its experimental determination. As mentioned before, the coulometric determinations of strong acids or bases most nearly approach the ideal measurement situation [8,9,10] in aqueous media completely free of reactive impurities. A current efficiency of 100% is only obtainable for one type of electrode reaction: the electrolysis of a molten salt or of a pure solvent; and this only holds when the products of the anode and cathode reactions

are prevented from reaching the other electrode. Therefore, except for the ideal case, there is always at least one secondary competing reaction at the electrode [13]. The estimated uncertainty of the SO₂ concentration from the dynamic dilution system is approximately ±0.5%. For the coulometric method the 101.1% current efficiency is a measure of a systematic bias in the analysis for which a correction has to be applied.

Table 1. Current efficiency determination^a

Permeating tube concentration (μmol/mol)	Coulometric concentration (μmol/mol)	Current efficiency (%)
48.0 ± 0.6	48.6 ± 0.2	101.1 ± 0.6

$$^a \text{Current efficiency} = \frac{\text{Coulometric current (mA)}}{\text{Theoretical current (mA)}} \times 100.$$

All uncertainties are expressed at the 95% confidence level.

Results of a series of analyses of SO₂/N₂ Standard Reference Materials (SRM), at the nominal 50 and 100 ppm level are given in Table 2. The certified values are concentrations placed on the individual SO₂/N₂ mixtures as determined by acid-base peroxide titration [11] and non-dispersive infrared analysis. They are presented here only as a frame of reference for the coulometric values. The uncertainties reported for the coulometrically determined cylinders in Table 2 are representative of the overall analytical imprecision at the 95% level of confidence. These uncertainties are the result of the uncertainty placed on the method at its present stage of development following the long-term study of the control cylinder (cylinder A, Table 2). The uncertainty of a single analysis of cylinder gas mixtures of SO₂ in N₂ at the 50 to 100 μmol/mol level is ±6% at the 95% confidence level.

Table 2. Coulometric titration results

Cylinder identification	Coulometric ^a value (μmol/mol)	Coulometric ^c value (μmol/mol)	Certified ^b value (μmol/mol)	Ratio (corrected to certified)
A	47.5	47.0	46.7	1.006
B	48.0	47.5	46.7	1.017
C	49.5	49.0	48.2	1.017
D	97.2	96.1	95.7	1.004
E	96.4	95.3	95.7	0.996

^a The uncertainty at the 95% confidence level is 6%.

^b The uncertainty at the 95% confidence level is 2%.

^c Corrected for current efficiency bias.

To evaluate this particular method for its independence, and as a companion to the standard reference method [11], one must look critically at the factors that are important. The equation used in the final calculation of concentration is:

$$\text{SO}_2 \left(\frac{\mu\text{mol SO}_2}{\text{mol N}_2} \right) = \frac{C_{\text{cell}} \cdot K}{Q} \quad (1)$$

where C_{cell} = Cell current (A)
 Q = Flow rate of sample (mL/min)

and

$$K = \frac{6 \cdot 10^7 \cdot MV_T}{n \cdot F} \quad (2)$$

MV_T = Molar volume of air (corrected for temperature) mL/mol
 (24470.69 @ 298 K)

n = Number of electron change (e⁻)
 ($n = 2$)

F = The Faraday constant (96485.38 A s/mol)

$6 \cdot 10^7$ is a unit conversion factor

$$\left(\frac{\text{s} \cdot \mu\text{mol}}{\text{min} \cdot \text{mol}} \right)$$

From a review of Eq. (1), it becomes clear that the two important experimental variables are current and flow rate. To assure the accuracy of these two variables the current meter and mass flow controller described earlier are periodically calibrated. The coulometric method is capable of both precision and accuracy. This is supported by the data presented in Table 2. Once the bias correction is applied to the coulometric results the difference between the coulometric values and the certified values for all of the samples fall within the 2% uncertainty placed on the cylinders by peroxide titration and NDIR. The absolute difference between the corrected coulometric value and the certified value for all samples measured range from 0.2 to 0.4 μmol/mol.

4. Conclusion

The coulometric method described can be used to determine low concentrations (μmol/mol) of SO₂ in nitrogen, at low flow rates and with a coulometric

current efficiency near 100%. It offers a simple yet independent method for determining SO₂/N₂ in compressed gas cylinders at the μmol/mol level. The intercomparison of the results obtained by coulometry with those of the acid-base peroxide titration method shows that there is no statistical difference between the methods. However, coulometry is capable of the same degree of precision and accuracy as the acid-base peroxide titration method in less time and with less effort and, at the same time, gives results that are independent of calibration standards. The method presented here for the analysis of SO₂/N₂ compressed gas cylinders is easily adaptable to other analyte species such as CO, CO₂, NH₃, NO₂, H₂S, and others. In the companion paper the method is modified for the analysis of cylinder gas mixtures of CO₂ in Air.

5. References

- [1] D. Weber, K. Olsen, and J. B. Ludwick, *Talanta* **27**, 665-668 (1980).
- [2] J. F. Alder and K. Kargosha, *Anal. Chim. Acta* **111**, 145-153 (1979).
- [3] C. D. Frazier, *Ion Chromatogr. Anal. Environ. Pollut.* **2**, 211-221 (1979).
- [4] P. Bruno, N. Caselli, M. Della Monica, and A. DiFano, *Talanta* **26**, 1011-1014 (1979).
- [5] A. Ríos, M. D. Luque de Castro, and M. Valcarcel, *Anal. Chem.* **59**, 666-670 (1987).
- [6] H. Okabe and F. P. Schwartz, *Anal. Chem.* **46**, 1024-1028 (1974).
- [7] E. Bishop, *Coulometric Analysis*, Volume 11D, C. L. Wilson and D. W. Wilson, eds., *Comprehensive Analytical Chemistry*, Elsevier, Amsterdam (1973).
- [8] J. K. Taylor and S. W. Smith, *J. Res. Natl. Bur. Stand. (U.S.)*, **63C**, 65-67 (1959).
- [9] G. Marinenko and J. K. Taylor, *Anal. Chem.* **40**, 1645-1648 (1968).
- [10] G. Marinenko and C. E. Champion, *Anal. Chem.* **41**, 1208-1212 (1969).
- [11] H. H. Hughes and J. Mandel, *NBSIR 81-2227* 43-46 (1981).
- [12] H. J. Boniface and R. H. Jenkins, *The Analyst* **103**, 1185-1194 (1978).
- [13] E. Bishop, *Chemia Analit.* **17**, 511-555 (1972).

About the authors: Gerald D. Mitchell is an analytical chemist in the Organic Analytical Research Division and Adville A. Bell is a computer analyst with the Surface Microanalysis Science Division, both of which are in the Chemical Science and Technology Laboratory of NIST.

Development of a Coulometric Method for Assessing the Concentration of Ambient Levels of CO₂/Air in Compressed Gas Mixtures

Volume 96

Number 5

September-October 1991

**G. D. Mitchell and
A. A. Bell**

National Institute of Standards
and Technology,
Gaithersburg, MD 20899

The coulometric method presented here is a reliable method for the direct analysis of CO₂/air cylinder gas mixtures. It is based on Faraday's laws of electrolysis and therefore no external standardization is required. A series of CO₂/air cylinder gas mixtures ranging in concentration from 300 to 375 μmol/mol (ppm) were analyzed and the results compared to those results obtained by non-dispersive infrared (NDIR) analysis with traceability to gravimetric stan-

dards. The coulometric method is rapid, sensitive, precise, and with the proper experimental controls, will yield accurate results.

Key words: carbon dioxide; coulometry; current efficiency; cylinder gases; monoethanolamine; N,N-dimethylformamide.

Accepted: July 10, 1991

1. Introduction

The understanding of global "greenhouse" issues as they relate to CO₂ in the atmosphere is a current environmental concern [1,2]. To assess changes in the levels of CO₂ in the atmosphere, three considerations are important: 1) a substantial history of the global levels of CO₂ over an extended period of time, 2) the fidelity of standards upon which the analyses are based, and 3) accuracy and reproducibility of methods used. At the National Institute of Standards and Technology there is a continuous search for methods of analysis that yield results that are traceable to fundamental quantities. The present method used for the certification of CO₂/air cylinder gas mixtures as Standard Reference Materials is nondispersive infrared analysis which is calibrated with CO₂ in air standards prepared by gravimetry [3]. In this work we present an analytical technique based on coulometry that provides accurate CO₂ analysis for ambient-air standards having negligible quantities of other acid components. This technique can be used to assist

in the validation of CO₂/air SRMs.

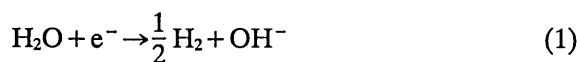
In our companion paper [4] we described the design, construction, and use of an apparatus for the determination of SO₂ in gas cylinder mixtures at the μmol/mol level. Here, the apparatus has been modified to demonstrate the potential utility of coulometry as an accurate and reliable method for assessing the concentration of CO₂ at the 300 to 375 μmol/mol level in cylinder gas mixtures.

2. Experimental Methods

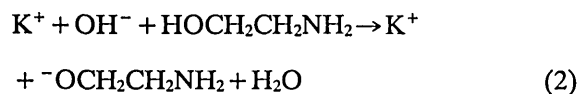
The apparatus and experimental details have been previously described [4] and will not be discussed fully here. However, because the analytical technique is being applied to CO₂/air and not SO₂/N₂, the experimental differences will be delineated. The experimental method is based on acid-base coulometric titration with photometric end-point detection. The experimental objectives are to: (a) select a reaction scheme; (b) develop an accurate

and precise sample delivery and absorption system; and (c) determine the current efficiency independently. The absorption system selected is designed to meet the two major criteria for coulometric titration, i.e., complete absorption of the CO₂ analyte gas and near 100% current efficiency [5,6,7].

The absorbing solution consists of 78 mL N,N-dimethylformamide [HCON-(CH₂)₂], 2 mL 0.1% thymolphthalein (5',5''-diisopropyl-2',2''-dimethylphenolphthalein) dissolved in dimethylformamide, 3 g potassium iodide dissolved in 3 mL water, and 3 mL monoethanolamine (HOCH₂CH₂NH₂). The solution is prepared in a 100 mL flask. The pH indicator, thymolphthalein, operates over the pH range from 9.3 to 10.5 and has an absorption maximum at 598 nm. All chemicals are reagent grade and are used without further purification. A possible reaction scheme involves the reduction of H₂O at the cathode,



then



Alternative schemes are presented in Ref. [5].

2.1 Procedure

The apparatus for CO₂ analysis uses a narrow band interference filter (599 ± 10 nm) and a titration cell, filled with the absorbing solution described above. Light passing through the clear gas-absorbing solution causes the photodiode detector to generate a titration current that is fed back to the cathode, thus causing reaction [1] to occur. The pH indicator thymolphthalein is activated by the production of the base and the absorbing solution turns blue, which decreases the output of the photodiode. When the color of the absorbing solution reaches a selected level of intensity, the feedback circuit is adjusted to give a zero current output for the cell. The CO₂/air mixture is introduced, metered by a mass flow controller calibrated to 0.1 mL/min. When the feedback circuit is adjusted to zero and the CO₂/air mixture is introduced into the cell, the analytical procedure and data analysis are identical to those discussed in Ref. [4].

The critical measurement parameters are cell current (A) and flow rate (mL/min). The current is measured using a calibrated digital current meter

and the flow rate is monitored using a calibrated mass flow controller. The relationship of cell current and flow rate of CO₂ is linear over the experimental range. Equation (3) gives the relationship of cell current and flow rate as it is used to determine CO₂ concentration in μmol/mol.

$$\text{CO}_2 \left(\frac{\mu\text{mol CO}_2}{\text{mol air}} \right) = \frac{C_{\text{cell}} \cdot K'}{Q} \quad (3)$$

where C_{cell} = Cell current (A)
 Q = Flow rate of sample (mL/min)

and

$$K' = \frac{6 \cdot 10^7 \cdot MV_T}{n \cdot F} \quad (4)$$

MV_T = Molar volume of air (corrected for temperature) mL/mol
 ($MV_T = 24475.59$ @ 298 K)

n = Number of electron change (e⁻)
 ($n = 1$)

F = The Faraday constant (96485.38 A s/mol)

$6 \cdot 10^7$ is a unit conversion factor

$$\left(\frac{\text{s} \cdot \mu\text{mol}}{\text{min} \cdot \text{mol}} \right)$$

3. Results and Discussion

Ten compressed gas cylinders with CO₂ concentrations from 300 to 375 μmol/mol were previously analyzed by a non-dispersive infrared (NDIR) analyzer calibrated with gravimetrically prepared standards [3]. A cylinder representing the mid-range of the set of 10 cylinders was selected as a control (cylinder 4, Table 1) to be used throughout this study to evaluate the overall uncertainty associated with the coulometric method and the day to day imprecision of the analysis. The control was studied over a variety of experimental conditions and for an extended period of time. The control cylinder was analyzed by the coulometric method on 17 separate occasions. Figure 1 shows the uncorrected data for the control cylinder as they were obtained chronologically over a 11 month period. The mean and the 95% confidence interval are indicated by the horizontal solid and dashed lines, respectively. The best estimate of the true mean concentration

Table 1. Comparison of CO₂ coulometric^a and NDIR data

Cylinder number	Direct coulometric concentration μmol/mol	Corrected ^b concentrations μmol/mol	NDIR concentration ^c μmol/mol	Ratio Coul/ NDIR
1	307.3	303.3	303.8	0.998
2	337.5	333.1	335.9	0.992
3	338.1	333.7	335.9	0.993
4*	346.4	341.9	341.7	1.001
5	344.8	340.3	342.8	0.993
6	348.2	343.7	343.2	1.001
7	349.8	345.2	347.6	0.993
8	352.7	348.1	351.5	0.990
9	380.2	375.3	375.2	1.000
10	380.7	375.8	375.3	1.001

^a Uncertainty ± 4.2 μmol/mol.^b Direct coulometric data corrected for current efficiency.

$$\text{Current efficiency} = \frac{\text{Coulometric current (mA)}}{\text{Theoretical current (mA)}} \times 100.$$

^c Uncertainty ± 0.4 μmol/mol.

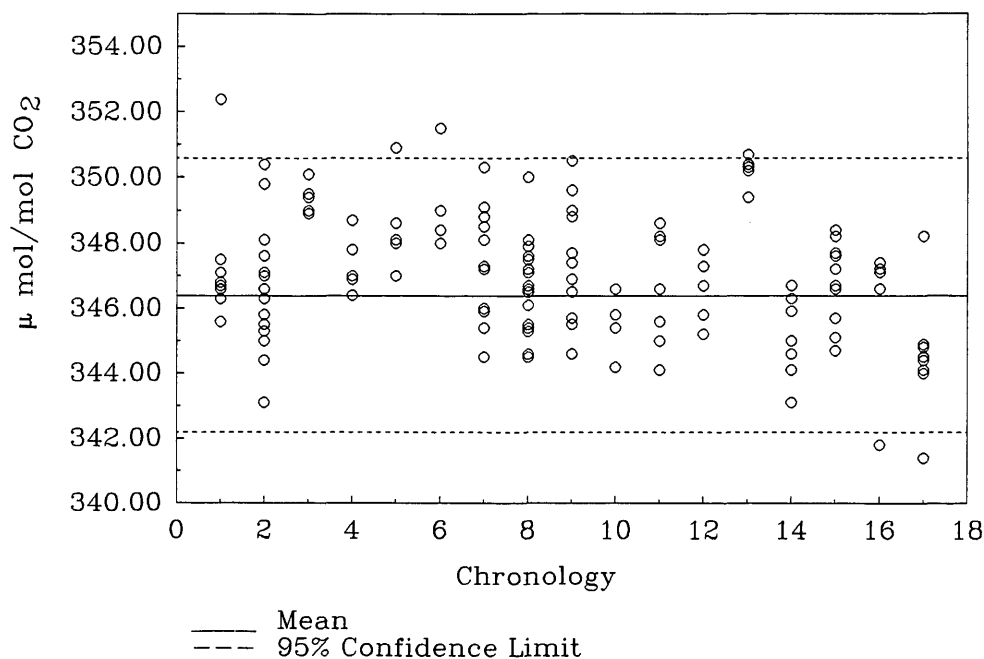
and its uncertainty at the 95% level of confidence is 346.4 ± 4.2 μmol/mol. For any given day, the standard deviation of a single measurement for the concentration range from 300 to 375 μmol/mol CO₂/air is 2.1 μmol/mol. The reported NDIR concentration of the control cylinder was 341.7 ± 0.4 μmol/mol. The comparison of this value to the coulometrically determined value is a measure of the current effi-

ciency. At the 95% level of confidence, the current efficiency is calculated to be $101.3 \pm 1.0\%$. This value represents a systematic bias in the measurement system and gives the factor by which the experimental data should be corrected.

Results for the coulometric analysis of the 10 CO₂/air gas cylinders mixtures as well as those obtained by NDIR are given in Table 1. The difference between the NDIR and corrected coulometric analytical values range from 0.003 to 1.1%. These results, however, show that at the present stage of development the method is capable of producing results that are comparable to those of the reference method. Figure 1 shows that the resulting analysis of the control cylinder is biased by 1.3%. No explanation for the bias is being offered at the present, however, future work is planned to improve both the precision and accuracy of the method.

4. Conclusion

A coulometric method for the direct analyses of reference cylinder gas mixtures has been demonstrated. It has been shown to be sensitive, potentially precise and accurate for determining CO₂ in air at atmospheric concentrations, as well as a viable method of assessing the concentration of CO₂

**Figure 1.** Chronological study.

cylinder gas mixtures. The system presented here provides rapid analyses, and is capable of being independent in the determination of CO₂ at ambient air levels. The upper and lower limits of detection have not yet been fully explored. However, on the upper end, the limiting critical component of this approach is the ability of the absorbing solution to handle higher concentrations of CO₂. On the low end, preliminary tests have provided detection limits of approximately 1 μmol/mol CO₂/air. This method of analysis is traceable to the Faraday constant and therefore no standardization against analyzed samples or pure materials is required. At the present state of development, the imprecision of a single analysis by the coulometric method is approximately 1.3%.

Acknowledgment

We acknowledge W. Dorko and M. Verkouteren for their useful discussions and R. Paule for his assistance with the statistical analysis of the data and the Standard Reference Materials Program at the National Institute for Standards and Technology for its financial support of this work.

6. References

- [1] M. C. MacCracken and F. M. Luther, eds., DOE/ER-0237, U. S. Department of Energy, Government Printing Office, Washington, DC (1985a).
- [2] M. C. MacCracken and F. M. Luther, eds., DOE/ER-0235, U. S. Department of Energy, Government Printing Office, Washington, DC (1985b).
- [3] R. C. Myers, W. D. Dorko, and R. A. Velapoldi, Report of Analysis (NIST internal report), 553-65-88, National Institute of Standards and Technology, Gaithersburg, MD (1988).
- [4] G. D. Mitchell and A. A. Bell, *J. Res. Natl. Inst. Stand. Technol.* **96**, 541 (1991).
- [5] H. J. Boniface and R. H. Jenkins, *Analyst* **103**, 1185-1194 (1978).
- [6] P. Braod, et al., *Analyst* **91**, 439-444 (1966).
- [7] D. C. White, *Talanta* **13**, 1303-1311 (1966).

About the authors: Gerald D. Mitchell is an analytical chemist in the Organic Analytical Research Division and Adville A. Bell is a computer analyst with the Surface Microanalysis Science Division, both of which are in the Chemical Science and Technology Laboratory of NIST.

Certification of NIST SRM 1961: 30 μm Diameter Polystyrene Spheres

Volume 96

Number 5

September–October 1991

Arie W. Hartman, Theodore D. Doiron, and Gary G. Hembree¹

National Institute of Standards and Technology,
Gaithersburg, MD 20899

This report describes the certification of SRM 1961, an NIST Standard Reference Material for particle diameter. It consists of an aqueous suspension of monosize 30 μm diameter polystyrene spheres. The primary technique used optical microscopy; it gave a mean diameter value $\bar{D} = 29.62 \pm 0.04 \mu\text{m}$ and a standard deviation of the size distribution $\sigma_D = 0.21 \mu\text{m}$. Over 2000 spheres were measured. The supporting tech-

nique used electron microscopy, which yielded $\bar{D} = 29.68 \pm 0.11 \mu\text{m}$. Ninety spheres were measured.

Key words: electron microscopy; microspheres; optical microscopy; particle size; polystyrene; standard reference materials.

Accepted: July 16, 1991

1. Introduction and Summary

This report contains the procedures, measurement results, and error analysis for the certification of SRM 1961, a Standard Reference Material for particle diameter. The SRM consists of a 0.5% aqueous suspension of monosize polystyrene microspheres with a nominal mean diameter of 30 μm .

The calibration was carried out by two independent methods: specialized forms of optical and electron microscopy. The first method is referred to as Center Distance Finding, or CDF; the second method is named Metrology Electron Microscopy, or MEM. The two methods are described in Sec. 2, the measurement results are shown in Sec. 3, and the error analysis is given in Sec. 4.

The results of the calibration are as follows:

- mean diameter: $\bar{D} = 29.62 \pm 0.04 \mu\text{m}$
- diameter distribution: Gaussian from 3 to 97%
Standard deviation $\sigma_D = 0.21 \mu\text{m}$
- number of outliers (defined as $|D - \bar{D}| > 4 \sigma_D$):
1% for oversize
1% for undersize

Ten samples totaling over 2000 spheres were measured.

2. Methods

The two methods used in the calibration of SRM 1961 are described next.

2.1 Optical Microscopy (CDF)

A drop of microsphere suspension is placed on a microscope slide, allowed to flow out and dry.

¹ Now with the Department of Physics, Arizona State University, Tempe, AZ 85281.

During drying the drop breaks up into numerous smaller droplets that dry individually. The spheres that these droplets contain are pulled together by surface tension forces, resulting in strands and small clusters of contacting spheres (Fig. 1). The contacting spheres are illuminated by near-parallel light (condenser stopped down), and as shown in Fig. 2 a number of small and circular “focal spots” form in the common back-focal plane. When a photomicrograph is taken of this back-focal plane, each recorded spot marks a sphere center. The distances C between adjacent spots represent the sum of two sphere radii. If the sphere diameters D are distributed normally (Gaussian), the C -values will be distributed normally also. The mean value \bar{C} then equals \bar{D} and the standard deviation σ_C of the C -distribution equals $\sigma_D/\sqrt{2}$. In this way \bar{D} and σ_D are found. This technique is called Center Distance Finding, or CDF [1].

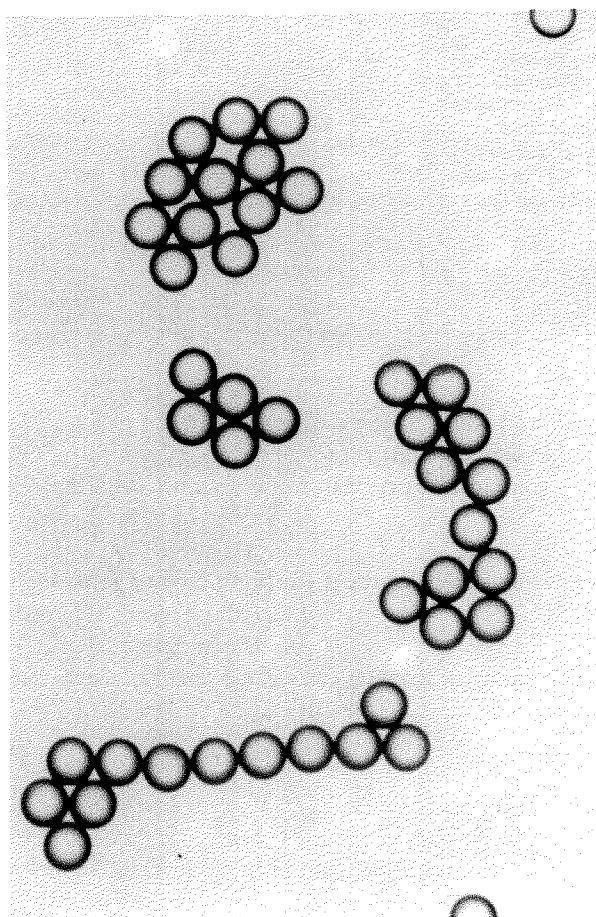


Figure 1. Strands and clusters of 30 μm spheres.

As shown in Fig. 3 the focal spots are small (about 1 μm in the object plane), uniform, and circular, permitting center distances C to be measured with high precision: a few hundredths of a μm in the object plane. It thus allows a measurement of the diameter distribution, which would be difficult to do from measurements of the sphere images themselves.

For the measurements, a number of microsphere slides are prepared and photographed. A large number of photographs are measured under computer control (see Appendix A). The film scale (image magnification) is measured, as outlined in Appendix B. The image distortion, which for high-quality optics is a function of off-axis distance only, is measured also (see Appendix B). The computer then applies a radial correction to each measured focal spot position. The corrected center distances C are determined, which leads to \bar{D} and σ_D .

2.2 Electron Microscopy (MEM)

With this method, called Metrology Electron Microscopy or MEM, the focused beam of a scanning electron microscope (SEM) is held stationary while a single-axis scanning stage with interferometric position readout moves the specimen such that the electron beam traverses a diameter of a sphere to be measured. An interferometer system measures stage travel versus time during a constant-speed scan, and the secondary electron detection system measures the electron output varying with time, all under computer control. The two data streams are combined, resulting in a value for the edge-to-edge diameter of the sphere [2]. The operation resembles that of an optical measuring microscope, where a set of crosshairs defines a stationary reference point in the field of view and a micrometer screw measures stage travel. See also Refs. [2] and [3], and Fig. 4.

3. Measurements

In this section are given details of the specimen preparation, data collection and reduction, and the measurement results. Section 3.1 covers optical microscopy, Sec. 3.2 treats electron microscopy.

3.1 Optical Microscopy (CDF)

Four samples were taken from one vial of SRM 1961 microsphere suspension, and one sample from

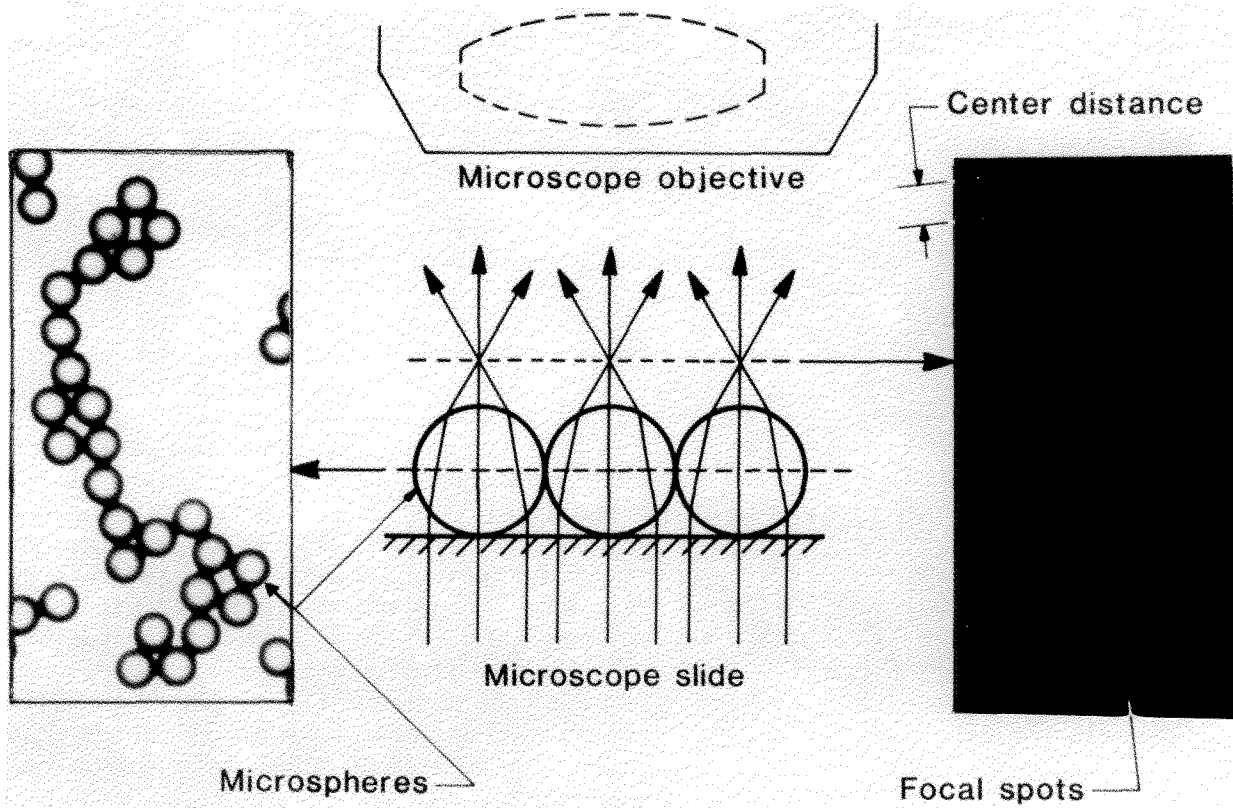


Figure 2. The CDF microsphere sizing scheme.

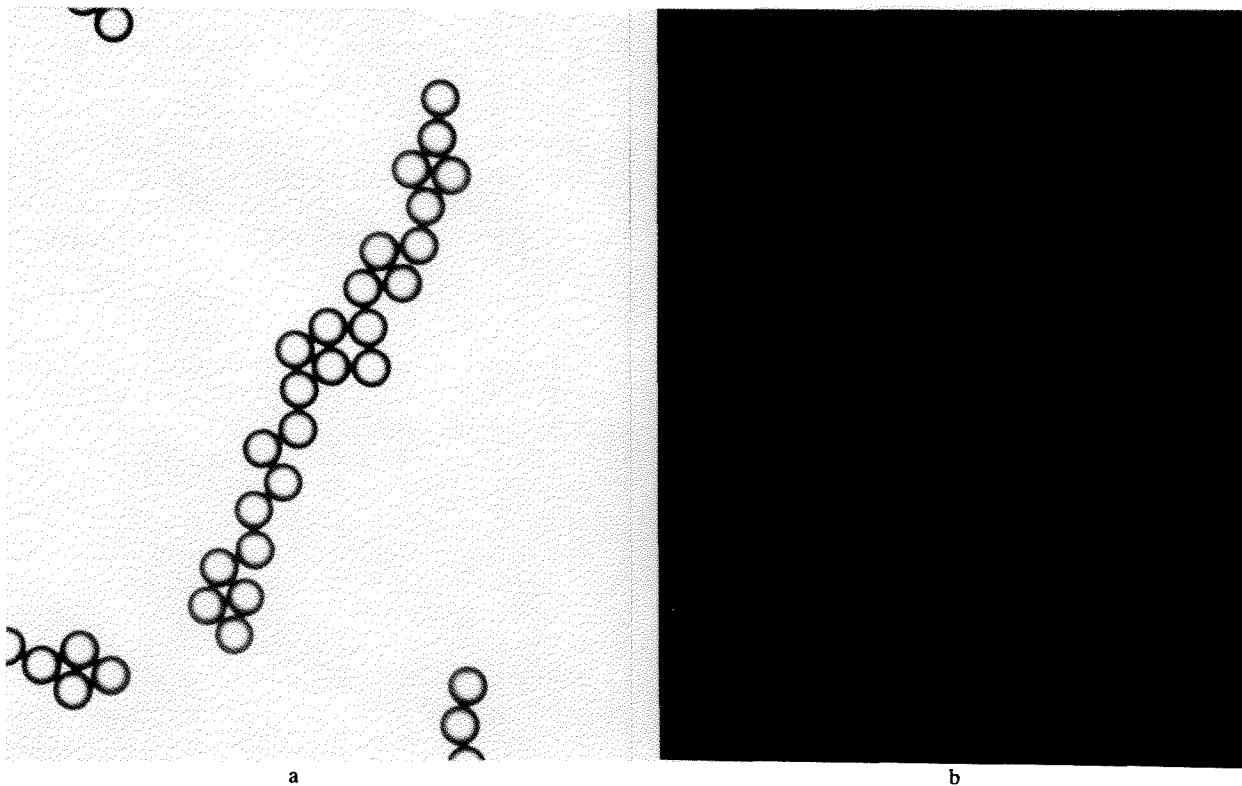


Figure 3. a) A microsphere grouping. b) Its focal spot pattern.

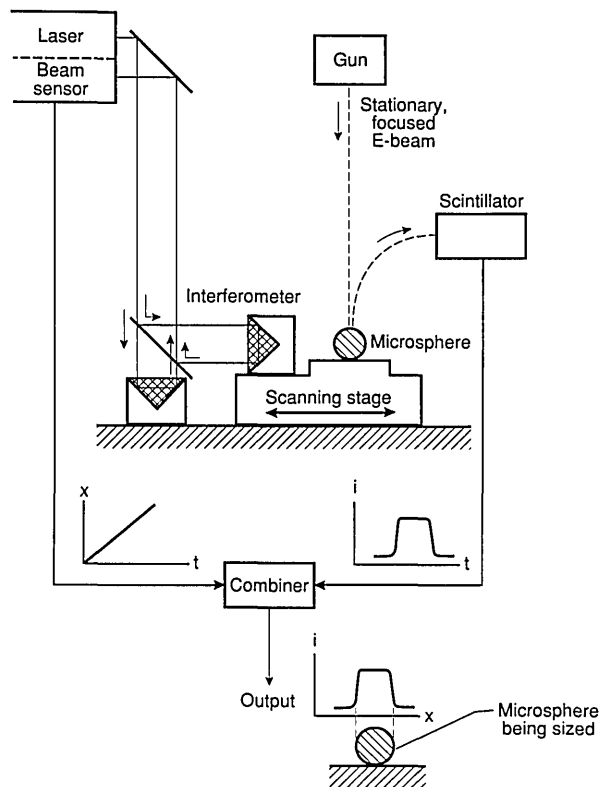


Figure 4. Diagram of the Metrology Electron Microscope (MEM).

each of three other vials. The vial contents were homogenized by rolling and shaking for two minutes, prior to dispensing a drop of suspension for analysis.

The microscope used was an Olympus Model BH-2² with a 20 \times /0.46NA objective, producing images with 200 \times magnification on 4 \times 5 in Polaroid sheet film.

Focal spot patterns from the contacting microsphere structures were photographed on Polaroid Type 57 positive film. This high-speed material (3000 ASA) has adequate dimensional stability [1] and low granularity, permitting its use for this SRM calibration. Ninety-nine photographs were taken, containing over 2000 focal spots. The center distances between adjacent focal spots were measured by means of a coordinate measuring machine (see Appendix A). The measurement path through each microsphere grouping was selected such that

each sphere was measured only once. The groupings of contacting spheres were examined first for overdeterminedness, to indicate where small air gaps between apparently contacting spheres could have formed during the drying process. Such gaps have minimum widths ranging from 0 to typically 1 σ_D [4,5]. Air gap formation can occur in microsphere groupings, such as hexagonal arrays where six neighboring spheres surround a center sphere while the spheres have slightly different diameters. Such sphere groupings were avoided in the measurement phase. An example of a measured microsphere grouping is shown in Fig. 3, while a selected measurement path is given in Fig. 5.

The measured photographs had a nominal print magnification of 200 \times . The measured focal spots had 0.2–0.3 mm diameters, their 6 mm center spacings were measured with 0.01 mm resolution. The microscope image calibration for magnification and image distortion is detailed in Sec. 4.1.1 and in Appendix B.

Measurement results are given in Table 1 and in Fig. 6. The data were originally plotted with center distances as the horizontal axis. This was then converted into a diameter scale by compressing the horizontal scale by $\sqrt{2}$ to reflect the fact that for normal distributions $\sigma_D = \sigma_C \sqrt{2}$, and by centering the D -scale such that the mean diameter \bar{D} coincides with the mean center distance \bar{C} . As assumed above, the resulting “diameter distribution” of Fig. 6b already implies that this distribution is considered a normal one. The information extracted from Fig. 6 is: a) the median diameter (which corresponds with the average diameter \bar{D} if the distribution is normal), b) the diameter range over which it actually is normal, and c) the value for the standard deviation σ_D associated with that diameter range.

Sample 1 was covered by four photomicrographs, each containing one large microsphere grouping. It was not possible to select a measurement path for each grouping such that each measured sphere had only two (or three) neighbors. As a result, the structures were likely to show the effect of air gaps present between many visually touching spheres, which increases the measured center distances. In hexagonally ordered microsphere structures (“hexagonal arrays”) the mean value of these gaps is known to be about 0.45 σ_D [4,5], amounting to 0.10 μm . In large random clusters, such as the four measured, the average gap width could be expected to be comparable to that value. This appears to be the case for sample 1 in Table 1. Excluding that sample lowers the grand mean diameter by 0.01 μm .

² Certain commercial equipment, instruments, or materials are identified in this paper to specify adequately the experimental procedure. Such identification does not imply recommendation or endorsement by the National Institute of Standards and Technology, nor does it imply that the materials or equipment identified are necessarily the best available for the purpose.

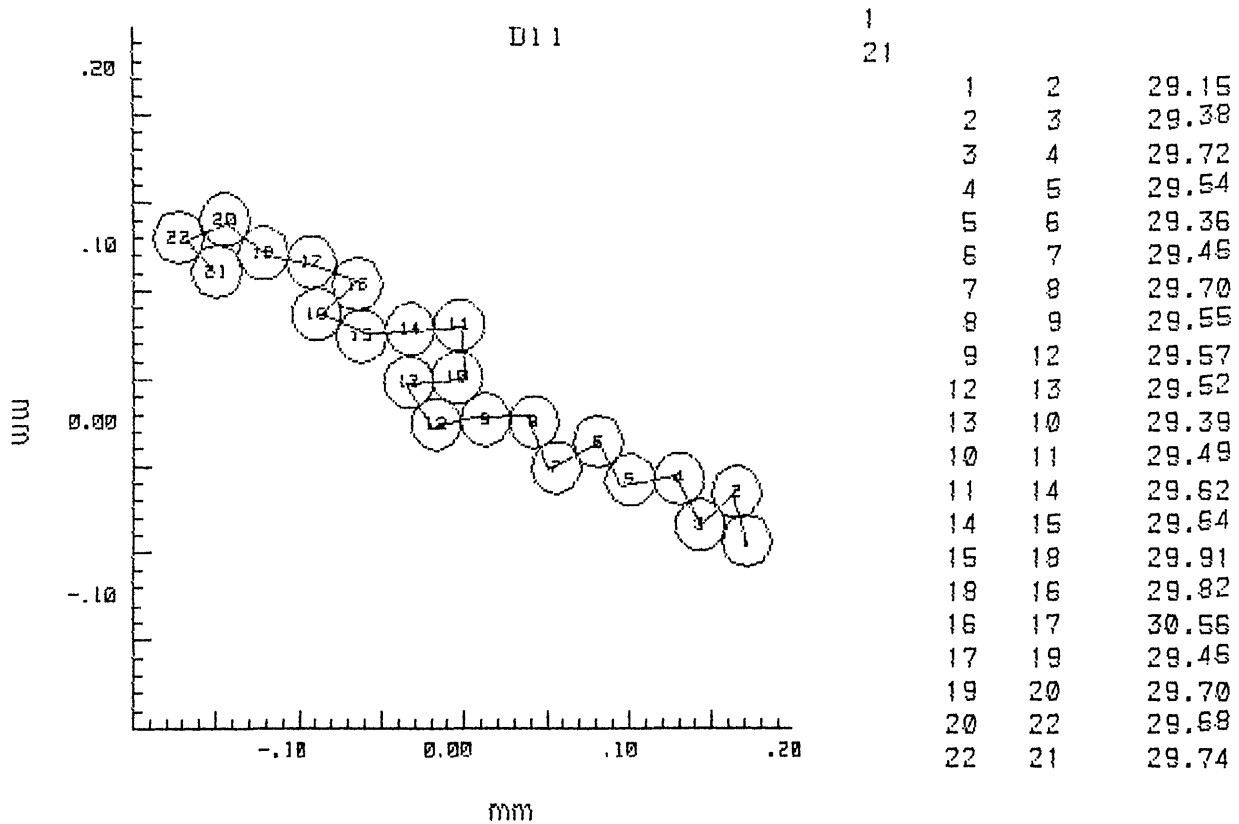


Figure 5. Measurement path for the sphere grouping of Fig. 3.

Table 1. Measurement results with optical microscopy^a

Vial #	Sample #	Sphere diameter (μm)		# of measurements	# of photographs
		average	median		
1	1	29.72	29.72	218	4
1	2	29.66	29.66	192	6
1	3	29.63	29.64	345	28
1	4	29.63	29.64	276	25
1	1 to 4	29.65	29.66	1031	63
2	5	29.59	29.59	608	18
3	6	29.60	29.59	255	12
4	7	29.58	29.57	151	6
all	all	29.62	29.62	2045	99

^a Diameter distribution is approximately normal from 3 to 97%. Standard deviation over this interval: 0.21 μm.

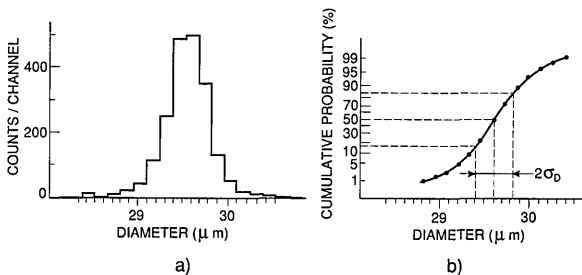


Figure 6. SRM 1961: a) Diameter distribution; b) Cumulative distribution.

3.2 Electron Microscopy (MEM)

The contents of an SRM vial 1961 were homogenized by rolling and shaking for 2 min. Then a drop was taken from the vial, diluted in 50 ml of 18 MΩ cm deionized water, and washed three times to reduce the amount of dissolved material remaining (biocide). Each washing cycle involved low-power ultrasonication, settling, and decanting four-fifths of the clear liquid. A small drop of the final suspension was placed on three thin carbon foils supported by 200 mesh copper TEM grids. The grids

were then coated with about 30 nm of amorphous carbon to minimize charge-up in the electron beam.

The electron microscope used for the microsphere diameter measurements is a Vacuum Generators VG HB-50A scanning electron microscope. It has in the secondary electron imaging mode an edge resolution of 0.03 μm at 30 keV and a 25 mm working distance. The interferometer is a Hewlett-Packard Model 5526A, utilizing a two-frequency stabilized He-Ne laser and a heterodyne scheme for measuring optical path differences. The two reflectors are mounted in the SEM vacuum on the fixed and moving parts of a piezo-electric one-axis scanning stage. The reflectors are corner cube prisms, to accommodate any misalignment over the relatively long distance (some 80 cm) from the stage inside the SEM column to the interferometer readout system outside. The scanning stage is placed on top of the X-Y stage in the SEM. The X-Y stage is used for searching. A simplified diagram of the setup is shown in Fig. 4.

Thirty microspheres were measured on each of three grids. We selected spheres that were touching one of the copper grid bars as further insurance against beam charge-up. Obvious outliers were excluded from the measurements. After each computer-controlled scan across a microsphere the microscope was reverted to scan mode (SEM) and the next sphere positioned manually for a line scan (spot mode). The scans, of which Fig. 6 shows an example, were about 38 μm long. The secondary electron intensity profile was sampled at 500 equally spaced points. The transition at the sphere edges fell within one data point spacing. The overall shape of this profile was complex, therefore the edge-finding algorithm was simplified by first taking the derivative of this profile and then finding the edges at the most positive and negative values, respectively [6] (see also Fig. 7). Measurement results are given in Table 2.

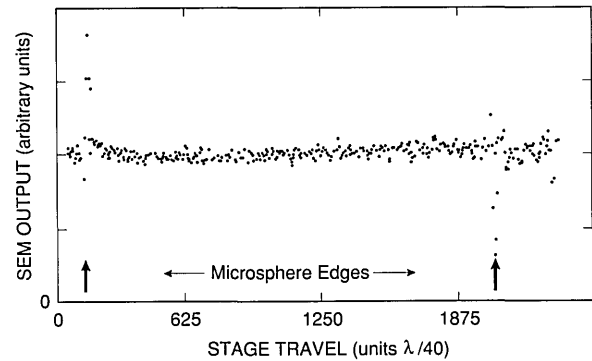


Figure 7. A microsphere scan obtained by MEM.

4. Error Analysis

In this section sources of uncertainty (called “errors” for short) are identified and evaluated for the two microsphere size measurement techniques. They are expressed as “ 3σ ” or “maximum” errors as indicated, the individual contributions are summed in quadrature, and the total systematic and random errors are added linearly to form “the uncertainty” of the measurement process (see also Tables 3 and 4).

4.1 Errors in Optical Microscopy

The errors in measuring the average diameter can be arranged in three classes: errors associated with finding the image magnification of the measured photographs, errors associated with measuring photographed focal spot spacings (center distances between contacting spheres), and errors associated with the diameter distribution. To find estimates for these errors, five repeat photographs were taken. Averaging of the repeat data was done to reduce the uncertainty of the measured magnification, while comparison between the photographs

Table 2. Measurement results with electron microscopy

Area #	Average diameter(μm) \bar{D}	Standard deviation(μm) σ_D	# of measurements
1	29.66	0.19	30
2	29.70	0.38	30
3	29.69	0.30	30
average	29.68		

Table 3. Error budget for a single 30 μm center distance measurement, using CDF^a

Category	Error source	Error contribution (μm)	
		Systematic	Random
On-axis magnification	Stage micrometer calibration	0.010	
	Film measuring machine calibration	0.001	
	Film readout, emulsion shifts, and magnification scatter (5 exposures)	0.030	
	Image distortion uncertainty	0.012	
		0.034	
Center distance measurement	Film readout and emulsion shifts		0.22
	Magnification scatter		0.08
	Image distortion-worst case		0.09
	Sphere flattening on contact		0.009
	Non-sphericity		0.15
	Subtotals	0.034	0.29
Finite sample size ($N = 2000$)	Diameter distribution width		0.30
	Totals	0.034	0.42

^a Uncertainty in \bar{D} : $0.034 + 0.42/\sqrt{2000} = 0.04 \mu\text{m}$. Measured \bar{D} (after corrections, see Sec. 4.1.2): 29.62 μm .

Table 4. Error budget for a single 30 μm sphere diameter measurement, using MEM^a

Category	Error source	Error contribution (μm)	
		Systematic	Random
Microsphere sensing	Imperfect scan and E-beam exposure	0.03	
	SEM spatial resolution and E-beam wander		0.042
Length measurements	Stage travel sampling		0.076
	Interferometer output digitizing		0.016
Finite sample size ($N = 90$)	Diameter distribution width ($\sigma_D = 0.21 \mu\text{m}$)		0.63
	Totals	0.03	0.72

^a Uncertainty in \bar{D} : $0.03 + 0.72/\sqrt{90} = 0.11 \mu\text{m}$. Measured \bar{D} : 29.68 μm .

was used to find scatter in measured focal spot spacings from which uncertainties in the magnification and in a single measurement of center distance can be derived. The three groups of errors are discussed next.

4.1.1 Errors Associated with Image Magnification The print magnification was found by photographing a calibrated chrome-on-glass stage micrometer (NIST No. 5525). The line center spacings in the prints were measured on a SGIP Universal Measuring Machine, Model MU-214B. The measured and averaged lengths were corrected for image distortion, which had been measured separately (Appendix B). The result was an image magnification value valid over the whole field of view; this value is equal to the on-axis value prior to image-distortion removal. A number of error sources affected the result, as detailed below.

a) The object micrometer.

The distance between the 1.80 and 2.20 mm lines of the calibrated stage micrometer was used. The length of section 0–1.80 mm was $1801.23 \mu\text{m}$ with a maximum error of $0.07 \mu\text{m}$, that of section 0–2.20 mm was $2199.51 \pm 0.11 \mu\text{m}$, giving for 1.80–2.20 mm a length $398.28 \pm 0.13 \mu\text{m}$. This corresponds to $\pm 0.033\%$ or $0.010 \mu\text{m}$ for a $30 \mu\text{m}$ length in the object plane—a systematic error.

b) The SGIP film measuring machine.

The scale error amounted to approximately $1.2 \mu\text{m}$ maximum per setting or about $2 \mu\text{m}$ for a difference between two settings. For the measured film distances (80.491 mm mean value) this amounts to about 0.002% or $0.001 \mu\text{m}$ in the object plane, a systematic error.

c) Film emulsion shifts, image magnification scatter, and film readout errors.

Polaroid Type 57 positive film exhibits, like most photographic emulsions, local random emulsion shifts. These lateral shifts are caused by non-uniform film processing and drying.

Magnification scatter is caused by slight changes in film position in the cassette (measured along the optical axis) when exposed film is replaced by a new film sheet.

Film readout errors reflect the precision with which one can visually pinpoint the center position of the scale division lines of the photographed object micrometer.

The combined contribution by these three error sources, based on an average of five repeat photographs, was found as follows. The 0.40 mm section of the calibrated object micrometer was photographed repeatedly at $200\times$, giving image lengths (in mm): 80.754, 80.777, 80.719, 80.853, and

80.818. The mean was 80.784, with a 3σ scatter of 0.079 mm or 0.10% . This total scatter contributes a $0.030 \mu\text{m}$ systematic error to a $30 \mu\text{m}$ center distance measurement. After correction for image distortion (see part d) the mean becomes 80.471 mm , giving an on-axis image magnification $M_o = 80.471 \text{ mm}/398.28 \mu\text{m} = 202.0\times$.

d) Image distortion.

The microscope exhibits radial image distortion: each off-axis image point is shifted radially by a small amount from its true position. In our case each end point of the 80 mm measured length was shifted outwards by 0.15 mm typically, with an estimated maximum uncertainty of 0.015 mm (Appendix B). This amounts to a combined 0.030 mm uncertainty in the measured length (the two error contributions are correlated), or 0.04% , corresponding to $0.012 \mu\text{m}$ in the object plane.

The error contributions a) through d) combine to a total systematic error of $0.034 \mu\text{m}$ (see Table 3).

4.1.2 Errors Associated with the Determination of Microsphere Center Distances The accuracy of center distance measurements is affected by various uncertainties: (a) those associated with pinpointing the positions of focal spot centers in the film, (b) with the correction of measured focal spot positions due to image distortion, (c) with the fluctuations in print magnification when new film is inserted in the cassette, (d) with possible distortion of the spheres at the contact areas, and (e) with the possibility that the individual spheres might be slightly deformed (showing a non-circular cross section when measured perpendicular to the line of sight).

a) The combined effect of film readout (pinpointing sphere centers) and emulsion shifts was found by taking five repeat exposures of a hexagonal array of the $30 \mu\text{m}$ spheres and measuring each time the same 17 distances between adjacent sphere centers in a selected microsphere row. This was done under computer control as described in Appendix A. All sets of five readings each were scaled down to the same average value (nominally 6.0 mm as a result of $200\times$ magnification of the $30 \mu\text{m}$ spheres). The 85 values were then pooled, resulting in a total scatter of $43 \mu\text{m}$ which amounts to $0.22 \mu\text{m}$ in a $30 \mu\text{m}$ object distance. This is a random error. As can be seen, this procedure reduced the effects of magnification scatter and avoided the effects of off-axis magnification changes due to image distortion, and of unequal-size spheres.

When pinpointing the center positions of the focal spot recordings in the film, the utilized coordi-

nate measuring machine with TV-microscope probe exhibited a reproducibility of better than 0.5 μm at 1 σ (see Appendix A). It translates to a maximum error of 2 μm in film distances between two focal spots, or 0.01 μm in distances between microsphere centers. This random error does not increase the 0.22 μm random error calculated above.

b) Magnification scatter, occurring when replacing sheet film in the cassette, was measured as 0.27% at 3 σ for the central area of a single exposure (see Appendix B). This value is considerably larger than can be expected from the data in paragraph c) of Sec. 4.1.1. One reason for this is that paragraph c) relates to measurements near the edges of the film sheet (the image of the object micrometer segment spans the field of view), where it is clamped by the cassette mechanism and consequently flexes much less. The corresponding maximum error for a 30 μm center distance measurement is 0.08 μm , an essentially random error. It has been applied to all areas in the film, as a worst case.

c) The effect of image distortion in our case (see Appendix B) is maximum for a sphere pair at the edge of the measured field of view. At 40 mm off-axis distance the maximum error in the measured image distortion is about $\pm 15 \mu\text{m}$; at 34 mm it is $\pm 10 \mu\text{m}$. Assuming that these errors are uncorrelated (a worst case), the resultant maximum error for 6 mm center distances oriented radially near the edge of the 80 mm field of view will then be $\pm 18 \mu\text{m}$ or 0.09 μm in the object plane, a random error. For center distances closer to the optical axis this error will be considerably less, and for those on the axis the error will be zero.

d) One can adopt the model that two polystyrene spheres approaching each other during the drying process will finally be in intimate contact over a circular area, the extent of which is controlled by a balance between van der Waals attraction and elastic deformation. This model has been analyzed by Derjaguin et al.; they have derived an expression for the resultant sphere flattening [7]. For the present case the two-sided flattening would amount to a shortening ΔC of the measured center distance C given by

$$\Delta C = \frac{1}{8} \left[\frac{6(1-\eta^2)^2 DA^2}{\epsilon^4 E^2} \right]^{1/3}, \text{ in which}$$

η = Poisson constant, 0.3 for polystyrene

D = sphere diameter, 3×10^{-3} cm

A = Hamaker constant, 1×10^{-12} erg for polystyrene

E = Young's Modulus, 3×10^{10} dyne/cm² for polystyrene

ϵ = distance of closest approach, 3×10^{-8} cm

This gives $\Delta C = 3.4 \text{ nm} = 0.003 \mu\text{m}$, lowering the measured diameter. If the selected values for A and E are each uncertain by a conceivable factor 2, then ΔC could change by a factor whose maximum value is $\sqrt[3]{16} = 2.5$. The ΔC estimate then ranges from 0.001 to 0.009 μm .

Although this model for sphere flattening on contact is not the only one available [8], experimental data (comparison with other calibration techniques for various monosize microsphere SRMs) support the Derjaguin model. Therefore the measured diameter values in Table 1 include a correction by a somewhat arbitrary increase of 0.01 μm , and a random error 0.009 μm is entered into the error analysis.

e) If a microsphere is elongated perpendicular to the line of sight, its focal spot will be elongated by the same amount [4]. The photographed focal spots are almost all very uniform and circular, with a diameter of 0.20 mm in the film plane corresponding to 1.0 μm in the object plane. A non-circularity of 0.03 mm is visually detectable, and any residual non-sphericity will then not exceed 0.15 μm , a random error. The random contributions combine to a maximum random error of 0.29 μm .

4.1.3 Errors Associated With the Microsphere Diameter Distribution Figure 7 shows that the diameter distribution is not quite normal. Of the measured population, 1 to 99% covers the size range 28.8 to 30.4 μm . The maximum error contribution to a single center distance measurement can be set at $\pm 0.30 \mu\text{m}$, a random error.

4.1.4 Combining the Various Error Contributions for the \bar{D} Measurement From Table 3 the total random error amounts to $0.41/\sqrt{2000} = 0.009 \mu\text{m}$, the total systematic error is 0.035 μm , therefore the total error in \bar{D} is 0.039 μm . The reported value for \bar{D} becomes $29.62 \pm 0.04 \mu\text{m}$.

4.1.5 Finding the Standard Deviation of the Size Distribution Figure 5 shows that the diameter distribution is normal from 3 to 97% (1900 spheres), and the calculated value of σ_D for this population is 0.23 μm .

- The statistical uncertainty in σ_D based on 900 measurements is $\pm 10\%$ at 3 σ , or 0.023 μm .
- Subtracting in quadrature the 1 σ random uncertainty in a single measurement of center distance (equal to 0.26/3 or 0.09 μm ; see Table 3) lowers σ_D to 0.21 μm , with an uncertainty of about 0.03 μm .

The reported value for σ_D is therefore $\sigma_D = 0.21 \pm 0.03 \mu\text{m}$.

4.2 Errors in Electron Microscopy

4.2.1 Errors Associated With Microsphere Sensing

a) Imperfect scans and E-beam exposure.

Each selected microsphere was positioned under the stationary electron beam such that a subsequent computer-controlled scan would result in the E-beam traversing the microsphere across its center as close as possible, while being measured edge-to-edge. Each scan was repeated a total of three times. In order to minimize errors from off-center scans and from a possible slight shrinking of the polystyrene microspheres from E-beam exposure, only the largest of the three edge-to-edge distances for each measured sphere was used in the data analysis.

The combined effect of these error sources is estimated as 0.1%, or $0.03 \mu\text{m}$ for a single diameter measurement. Because it is not known which part of this error is random or systematic, the whole error is considered a systematic one.

b) SEM spatial resolution and E-beam wander.

The edge resolution is $0.03 \mu\text{m}$, giving for a diameter measurement a random uncertainty of $0.042 \mu\text{m}$. The effect from E-beam wander is considered negligible.

4.2.2 Errors Associated With Stage Travel Measurement

a) Stage travel sampling.

The stage travel was $37.9 \mu\text{m}$ for each scan; it was sampled at 500 equidistant points, giving a digitizing error of $\pm 0.076 \mu\text{m}$.

b) Interferometer-output digitizing.

The HP interferometer readout system had a least count of $\lambda/40$, giving a digitizing error of $\pm 0.016 \mu\text{m}$.

4.2.3 Errors Associated With the Microsphere Diameter Distribution The diameter distribution has $\sigma_D = 0.21 \mu\text{m}$. For 90 measurements the 3σ error in the mean diameter is $0.63/\sqrt{90} = 0.066 \mu\text{m}$.

4.2.4 Combining the Various Error Contributions to \bar{D} Referring to Table 4, the 0.042 and $0.63 \mu\text{m}$ random errors combine to $0.63 \mu\text{m}$. The digitizing errors add linearly to this, giving $0.72 \mu\text{m}$. With the systematic error of $0.03 \mu\text{m}$ the total error in \bar{D} becomes $0.03 + 0.72/\sqrt{90} = 0.11 \mu\text{m}$, giving a reported value for MEM: mean diameter $\bar{D} = 29.68 \pm 0.11 \mu\text{m}$.

5. Diameter Calibration Final Results

The results of the certification are as follows:

Mean diameter of the SRM 1961 microspheres:

$\bar{D} = 29.62 \pm 0.04 \mu\text{m}$ (optical microscopy)

$\sigma_D = 0.23 \pm 0.03 \mu\text{m}$ (central peak)

Supporting value:

$\bar{D} = 29.68 \pm 0.11 \mu\text{m}$ (electron microscopy)

The quoted uncertainties are maximum values.

6. Sample Uniformity

From Table 1 an impression of sample uniformity can be obtained: the within-vial variation in the measured average diameter is $\pm 0.1\%$, and the between-vial variation amounts to a slightly larger amount ($\pm 0.13\%$). Sample 1 was a special case: instead of measuring string-like groupings, where each microsphere can freely touch its neighbors, four large conglomerates were measured (one per photograph). Such structures are overdetermined in the sense that after drying small air gaps can remain between apparently touching spheres. As expected, the average center distance between neighboring spheres was significantly larger for this sample than for all others. Because the average gap width is related to the sphere diameter distribution, a found increase in measured average center distance by about $1/4 \sigma_D$ does not seem unreasonable. Taking this into account, only upper limits for the SRM non-uniformity are quoted: $\pm 0.1\%$ for within-vial and between-vial sampling.

7. Outliers

As with the sample uniformity, only upper limits could be set to the percent oversize and undersize of the measured 2000 spheres. When outliers are defined as spheres with sizes more than $4\sigma_D$ different from the mean diameters, there are nearly 1% oversize and nearly 1% undersize (Fig. 5b). Spheres that were outside by some 10% or more could be found by visual inspection of the photomicrographs. In this way two oversize and two undersize spheres were found.

8. Appendix A. Measuring Microsphere Center Distances from Photomicrographs

The relative positions of the photographed microsphere focal spot positions are read out with a

coordinate measuring machine (CMM). Its probe is a microscope containing a high-resolution image sensor (vidicon) and circuitry to pinpoint the center of each focal spot, which is interfaced with the CMM control computer to bring the focal spot center to the boresight axis (center of the microscope's field of view). The CMM's X - Y coordinates are then stored.

Next, for each photograph being measured a decision is made as to what measurement path will be selected from one focal spot to the next, in order to make sure that each sphere is measured only once and that each sphere in the grouping could have been free to assume its contacting position with its neighbors during drying (no mechanically overdetermined sphere arrangement). The path selection is done by an operator using an interactive graphics routine. The CRT display shows all focal spots in their relative positions with circles drawn around each one, to simulate the actual microsphere scene rather than the focal spot representation of it. It also shows the keyed-in measurement path (see Fig. 5). The result is a string of X - Y coordinates in which each increment represents a center distance (CD) between two adjacent (contacting) spheres.

Before the CDs are computed each focal spot position is first corrected for image distortion of the microscope (this distortion can be determined as in Appendix B). Because the distortion is a radial function these position corrections take the form of small radial shifts. Their magnitudes depend on the initial off-axis distances, and are found by means of a stored function.

An impression of the repeatability and accuracy of the film measuring system can be obtained from the following information:

1. The CMM is normally used for the calibration of precision grid plates. It has been extensively studied, and its positional accuracy is better than $0.1\ \mu\text{m}$ over the area of the pictures measured [9].
2. Each focal spot was centered to the same point of the camera field, and all the spots were about the same size. Therefore any geometrical errors in the camera scan can have only secondary effects on the measurement.
3. A photograph selected at random was run a number of times without being moved. The center distances (6 mm nominally, the print magnification being $200\times$) showed a repeatability with standard deviation less than $0.5\ \mu\text{m}$.
4. One other photograph was measured repeatedly while the microscope focus was varied in both directions. Since the focal spot brightness was

not completely isotropic, the focus settings changed the apparent size and shape of the focal spots by small amounts. The resultant changes in focal spot positions were very small and uncorrelated, with an estimated standard deviation of less than $0.5\ \mu\text{m}$.

5. A few photographs were reexamined after all had been measured in order to check for any process changes during the measurements. No changes larger than the measured repeatability were found.

The CMM used was a five-axis Moore M5Z from Moore Special Tool Company. The TV camera system consisted of a Dage-MTI Inc. high-resolution vidicon camera Model 65, with a Bausch & Lomb lens type Mono Zoom 7 and a vision system from Videometrics VPU, Model 101110-501-14. The scene illumination was a diffuse one, using a fiber-optic ring illuminator from Titan Tool Company.

9. Appendix B. Measuring the Print Magnification (Film Scale) and Image Distortion

To set the scale of the photographs a section of a calibrated object micrometer is photographed and measured. To maximize resolution the photographed length is made to span the whole field of view. The measured length is then corrected for the effects of image distortion which causes off-axis image points to be radially shifted from their intended positions. The corrected length now shows the image magnification in the absence of image distortion. In other words: one has found the on-axis image magnification value.

For the determination of image distortion the microscope magnification itself is not needed. In the following is shown how these properties were measured.

a) Image distortion.

Following a scheme outlined in Ref. [1] this goes as follows. A row of microspheres is placed such that it crosses the center of the field of view. Its row of focal spots is photographed. Then the row is shifted in-line by three sphere diameter ($3D$) and its focal spots are recorded again. All distance between adjacent sphere centers are measured in both photographs; it will be seen that some center distances will have decreased while others increased. These changes are so small that a $3D$ line section rather than D was chosen in order to make the center distance changes stand out from measurement noise (see Fig. 8a).

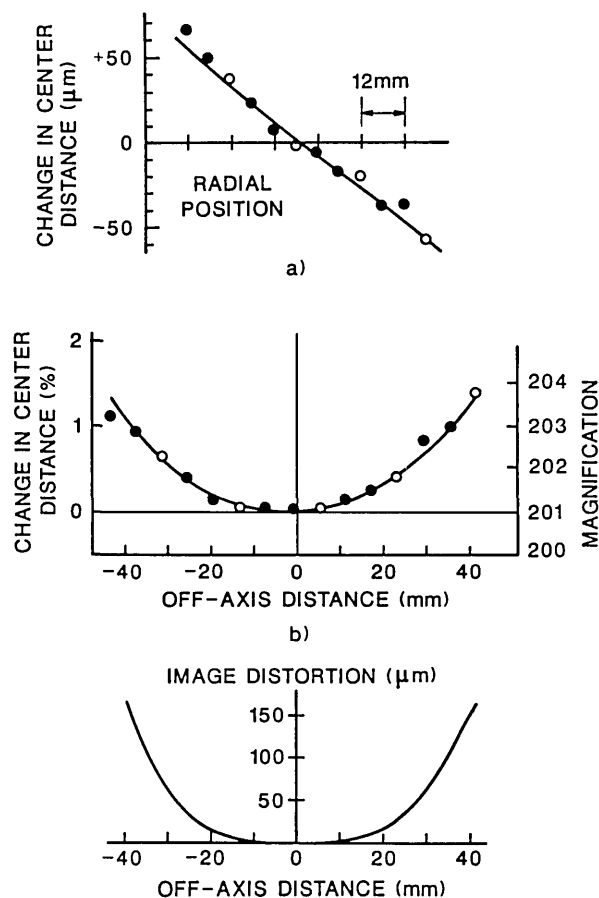


Figure 8. Finding microscope image distribution and magnification.

Assuming a $3D$ shift from left to right, and starting with the far left (first) sphere pair, one finds the accumulated length changes when the center distance length D is shifted in-line by $3D$ at the various points in the field of view. A second data set is found by repeating the length change calculations starting at the next left sphere pair. A third data set is obtained from the third left sphere pair. The three data sets belong to a common curve, and a best fit of all three sets is obtained as shown in Fig. 8b.

Figure 8b therefore shows by what percentage a center distance D will vary as it is shifted all across the field of view (this is equal to the percent change in magnification for radial objects as a function of off-axis distance). A graphic integration then yields the radial shifts of off-axis image points as a function of their off-axis distance, that is, the image distortion as shown in Fig. 8c.

b) Film scale.

With the image distortion known, the film scale or on-axis magnification M_0 is found next using

steps already described. If M_0 is measured a number of times the results will show data scatter, typically 0.3% at 3σ . This is caused by small changes in axial position when fresh sheet film is inserted in the cassette. The corresponding scale changes can be reduced by averaging over a number of repeat exposures, for instance five, of the object micrometer.

The effect of inserting fresh sheet film in the cassette can be measured by placing a row of microspheres such that it crosses the center of the microscope's field of view, taking five repeat photomicrographs, and measuring a number of sphere center distances in all photographs. The scatter found in these lengths contains the combined effects of film readout, local emulsion shifts and changes in film scale. As shown in Fig. 9 these data approximate a straight line through the origin; the slope of that line represents the scatter in film scale or magnification (0.09% at 1σ in our case), for areas near the center of the photographs. For this experiment a $10\ \mu\text{m}$ microsphere array was centered in the field of view, and the various lengths in Fig. 9 were realized by summing the lengths of a number of adjacent microsphere rows. The found magnification scatter was indicative of film flexure at the central area of the film frame.

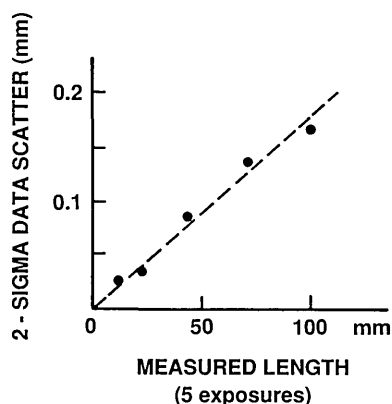


Figure 9. Scatter in image magnification.

10. References

- [1] A. W. Hartman, *Powder Technol.* **46**, 109 (1986).
- [2] G. G. Hembree, *Proc. 44th Ann. Meeting*, G. W. Bailey, Ed., San Francisco Press, San Francisco (1986) p. 644.
- [3] D. A. Swyt and S. W. Jensen, *Prec. Eng.* **3**, 11 (1981).
- [4] H. E. Kubitschek, *Nature* **192**, 48 (1961).
- [5] A. W. Hartman, *Powder Technol.* **42**, 269 (1964).
- [6] A. Savitsky and M. J. E. Golay, *Anal. Chem.* **36**, 1627 (1964).

- [7] B. V. Derjaguin, V. M. Muller, and Yu P. Toporov, *J. Coll. Interf. Sci.* **53**, 414 (1975).
- [8] K. L. Johnson, K. Kendall, and A. S. Roberts, *Proc. R. Soc. Lond.* **A324**, 301 (1971).
- [9] R. J. Hocken et al., *Annal C.I.R.P.*, Vol. 26 (1977).

About the authors: A. Hartman and T. Doiron are physicists in the Precision Engineering Division at NIST. G. Hembree, a physicist, was in the same division when this work was done.

Optimization Techniques for Permittivity and Permeability Determination

Volume 96

Number 5

September-October 1991

**Paul D. Domich,
James Baker-Jarvis, and
Richard G. Geyer**

National Institute of Standards
and Technology,
Boulder, CO 80303

This paper discusses optimization techniques for the determination of complex permittivity and permeability in transmission lines. The traditional theoretical model using scattering parameters is extended into a mathematical regression model that can be solved with widely accepted numerical techniques. This new model produces accurate primary mode results for the samples tested including nonmagnetic and magnetic materials with high dielectric constants. An extension of the model includes responses due to higher order modes. The general model determines parameters to specify the

spectral functional form of complex permittivity and permeability and is capable of small corrections to independent variable data including angular frequency, sample length, sample position, and cutoff wavelength. The method provides reliable determination for both low and high permittivity materials.

Key words: higher order modes; microwave; permeability; permittivity; primary mode; orthogonal distance regression; scattering matrix.

Accepted: June 17, 1991

1. Introduction

A constrained nonlinear optimization procedure is presented for the determination of complex permittivity and permeability spectra from scattering parameter (S -parameter) data taken from an automatic network analyzer (ANA). The procedure has been used successfully for reliable characterization of permittivity and permeability of many different test samples. In addition, it provides a basis for the analysis of multi-mode field data and for the determination of experimental systematic uncertainty.

Previous work in this area involved the determination of permittivity and permeability on a point-by-point basis with explicit or implicit solution of a system of nonlinear scattering equations at each particular frequency (see [1, 5]). Inaccurate results, however, may arise when numerical singularities occur at frequencies corresponding to integer multiples of one half wavelength of the material. The

same system of nonlinear scattering equations is used in this study. Here they are solved in the sense of least squares over the entire range of measurement by determining the best Laurent series approximations to permittivity and permeability consistent with linearity and causality constraints. Points of singularity may be de-emphasized to lessen the effect of highly uncertain data points.

This effort determines complex permittivity and permeability from two-port S -parameter data using the primary (or fundamental) mode field behavior in various materials. Physical measurements of the S -parameter data are made with an automatic network analyzer. Fundamental mode S -parameter relationships are then used to solve for permeability and permittivity, $\mu(\omega)$ and $\epsilon(\omega)$ respectively, as a function of the angular frequency ω .

The general functional form for μ and ϵ was decided upon after evaluating several different polynomial and trigonometric relations. The evaluation criteria for the functional form for permittivity and permeability was based on the reproducibility of the S -parameter data in terms of the minimum total least square approximation to these data. The best overall approximation was selected. The general functional form for μ and ϵ with acceptable results involves only the first two terms of a Laurent series.

The optimization approach in this research is an implicit function regression model. This model is solved by the orthogonal distance regression package ODRPACK [2]. This estimation package allows for adjustments in input parameters to compensate for measurement uncertainties. Adjustments here are limited to the sample length, sample position in the waveguide measurement fixture, and the cutoff wavelength. Orthogonal distance regression is intended to compensate for slight uncertainties in the independent variable (angular frequency, ω) as well as the dependent variable (observed S -parameter data).

The physical model is outlined in Sec. 2, with the related mathematical model discussed in Sec. 3. Numerical considerations are covered in Sec. 4 and conclusions and future directions discussed in Sec. 5.

2. Scattering Parameter Relations

The equations described below relate the measured two-port scattering parameters (S -parameters) to the permittivity and permeability of the material. First, in order to develop the scattering equations, the following notation is used. Let

$$\epsilon = [\epsilon'_R - j\epsilon''_R]\epsilon_0 = \epsilon_R^* \epsilon_0$$

and

$$\mu = [\mu'_R - j\mu''_R]\mu_0 = \mu_R^* \mu_0,$$

the permittivity and permeability of a sample material, where ϵ_0 and μ_0 are the permittivity and permeability of a vacuum, and ϵ_R^* and μ_R^* are the relative complex permittivity and permeability. Next let c_{vac} and c_{lab} be the speed of light in a vacuum and the laboratory, respectively, and for a given frequency f , let

$$\omega = 2\pi f,$$

be the corresponding angular frequency. Then

$$\gamma = j \sqrt{\frac{\omega^2 \mu_R^* \epsilon_R^*}{c_{vac}^2} - \left(\frac{2\pi}{\lambda_{c1}}\right)^2}$$

and

$$\gamma_0 = j \sqrt{\left(\frac{\omega}{c_{lab}}\right)^2 - \left(\frac{2\pi}{\lambda_{c1}}\right)^2}$$

represent the propagation constants in the material and air, respectively, where $j = \sqrt{-1}$ and λ_{c1} is the cutoff wavelength in the waveguide measurement fixture, where the subscript 1 refers to the fundamental mode. The expression for the transmission coefficient z is

$$z = \exp(-\gamma L),$$

where L is the sample length. The reflection coefficient is

$$\Gamma = \frac{\frac{\mu}{\mu_0} \frac{\gamma_0}{\gamma} - 1}{\frac{\mu}{\mu_0} \frac{\gamma_0}{\gamma} + 1}$$

or

$$\Gamma = \frac{\frac{c_{vac}}{c_{lab}} \sqrt{\frac{\mu_R^*}{\epsilon_R^*}} - 1}{\frac{c_{vac}}{c_{lab}} \sqrt{\frac{\mu_R^*}{\epsilon_R^*}} + 1}$$

for coaxial line when $\frac{1}{\lambda_{c1}} \rightarrow 0$.

It is assumed that the total length of the sample holder is

$$L_{air} = L + L_1 + L_2, \tag{1}$$

as shown in Fig. 1, where L_1 and L_2 are the distances from the calibration reference planes to the sample faces for ports 1 and 2, respectively.

For a two-port device the expressions for the measured S -parameters are obtained by the solution of a related boundary value problem. The explicit expressions for the scattering relations of the fundamental mode are assumed to functions of λ_{c1} are given by

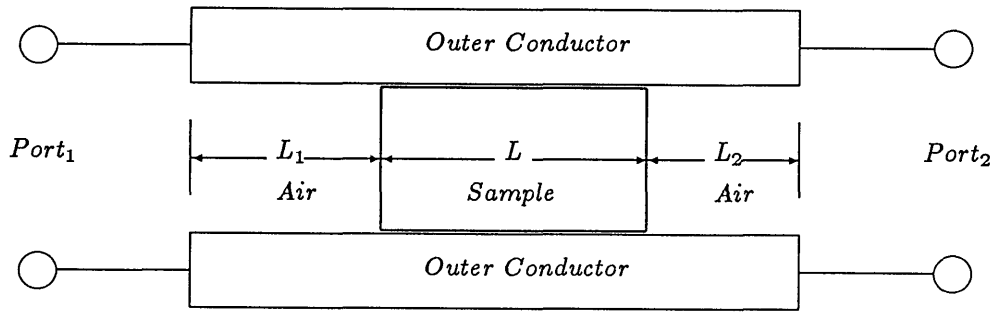


Figure 1. Dielectric sample in waveguide.

$$S_{11}(\lambda_{c1}) = R_1^2 \left[\frac{\Gamma(1-z^2)}{1-\Gamma^2 z^2} \right], \quad (2)$$

$$S_{12}(\lambda_{c1}) = R_1 R_2 \left[\frac{z(1-\Gamma^2)}{1-\Gamma^2 z^2} \right], \quad (3)$$

$$S_{21}(\lambda_{c1}) = R_1 R_2 \left[\frac{z(1-\Gamma^2)}{1-\Gamma^2 z^2} \right], \quad (4)$$

$$S_{22}(\lambda_{c1}) = R_2^2 \left[\frac{\Gamma(1-z^2)}{1-\Gamma^2 z^2} \right], \quad (5)$$

where $R_1 = \exp(-\gamma_0 L_1)$ and $R_2 = \exp(-\gamma_0 L_2)$ are the reference plane transformation expressions.

3. The Mathematical Model

3.1 $\mu_R^*(\omega)$, $\epsilon_R^*(\omega)$, and the Regression Model

The mathematical problem can be stated as that of finding parameters to a prespecified functional form for the complex functions $\mu_R^*(\omega)$ and $\epsilon_R^*(\omega)$. S -parameter data acquired from the ANA for selected samples of materials provide complex values for each of S_{11} , S_{21} , S_{12} , and S_{22} , at n different frequencies ranging from 1 to 18 GHz. The model determines the parameterization of μ_R^* and ϵ_R^* that best reproduces simultaneously the four S -parameters for the n observations, given the sample data, two reference plane positions, and the sample length.

The general form for $\mu_R^*(\omega)$ and $\epsilon_R^*(\omega)$ uses terms from the Laurent series:

$$f(\omega) = \sum_{i=-\infty}^{\infty} \frac{a_i}{(1+b_i\omega)^i}, \quad (6)$$

where a_i and b_i are complex scalars in the i th term. The solution procedure here is an implicit function regression and corresponds to the parameterization of two terms in a truncated Laurent series. Note that Eq. (7) automatically satisfies Kramers-Kronig relations (see, for example, [1] or [4]) for dispersion. The functional form for $\mu_R^*(\omega)$ and $\epsilon_R^*(\omega)$ follows:

$$\mu_R^*(\omega) \equiv f(\omega) = \frac{A_1}{1+B_1\omega} + \frac{A_2}{(1+B_2\omega)^2},$$

$$\epsilon_R^*(\omega) \equiv \tilde{f}(\omega) = \frac{\tilde{A}_1}{1+B_1\omega} + \frac{\tilde{A}_2}{(1+B_2\omega)^2}.$$

For notational convenience, the terms of the second truncated Laurent series \tilde{A}_1 , \tilde{A}_2 , \tilde{B}_1 , and \tilde{B}_2 will be referred to as A_3 , A_4 , B_3 , and B_4 .

The solution procedure to determine the complex parameters A_i , B_i is the minimization of the sum of the squares of the uncertainties between the predicted and observed S -parameters,

$$\min \left(\sum_{k=1}^n |S_{11}^k - P_{11}^k|^2 + |S_{12}^k - P_{12}^k|^2 + |S_{21}^k - P_{21}^k|^2 + |S_{22}^k - P_{22}^k|^2 \right)^{1/2} \quad (7)$$

where, for $ij = 1, 2$, S_{ij}^k represents the k th observed S_{ij} scattering parameter at frequency ω_k and

$$P_{ij}^k \equiv S_{ij}(\lambda_{c1}, \omega_k, A_1, \dots, A_4, B_1, \dots, B_4),$$

is the corresponding predicted scattering parameter. We let $|z| = \sqrt{\Re(z)^2 + \Im(z)^2}$ represent the absolute value of a complex scalar z . Note that Eq. (8) is equivalent to the minimization of the sum of the

squares of the real and imaginary parts of each of the S -parameters, i.e.,

$$\min \left(\sum_{k=1}^n \sum_{i=1}^2 \sum_{j=1}^2 \Re(S_{ij}^k - P_{ij}^k)^2 + \Im(S_{ij}^k - P_{ij}^k)^2 \right)^{1/2} \quad (8)$$

The model reported in Sec. 4.4 results uses the formulation in Eq. (8).

3.2 Adjustments to the Model Inputs

In standard ordinary least squares regression models, the observed responses are assumed to contain some uncertainties either produced by the phenomena under examination or introduced by the device that measures the events. In addition, certain independent and dependent variable pairs may not be as reliable as others due to an increased variance in the uncertainties in the dependent variable for particular values of the independent variable. The application of a reduced weight to points of questionable reliability provides the modeler with a means to de-emphasize such points to find a more appropriate regression solution.

Usually the independent variable can be controlled, and the precise value of each of the observations is well known. An orthogonal distance regression model provides the modeler with the additional ability to assume that the independent variable, in this case frequency, may contain some uncertainty as well. Allowances for this type of uncertainty can, in some cases, greatly improve the approximation. For this particular model and the samples tested in this study, the uncertainty in the independent variables is sufficiently small to allow the modeler to assume that an ordinary least squares approximation provides an adequate solution.

Other model parameters such as sample length, sample position in the waveguide, and cutoff wavelength are sufficiently sensitive to require slight perturbation. Each of these inputs is required by the S -parameter equations and is considered to be known by the modeler. Since these inputs are not always known exactly, each may be perturbed slightly, as determined by the problem solver, to improve approximation. This allows the user to adjust for measurement uncertainty.

In particular, since incorrect specification of the sample position, L_1 , in waveguide affects the value of phase in the reflected S -parameter data, an additional parameter, β_{L_1} , is included in R_1 ,

$$R_1 = \exp(-\gamma_0 [L_1 + \beta_{L_1}]).$$

Similarly, uncertainties in L_{air} and L_2 are represented by analogous means with parameters $\beta_{L_{\text{air}}}$ and β_{L_2} , respectively. With Eq. (1), the total length L of the sample is completely determined by

$$L = (L_{\text{air}} + \beta_{L_{\text{air}}}) - (L_1 + \beta_{L_1} + L_2 + \beta_{L_2})$$

and is parameterized by the values of $\beta_{L_{\text{air}}}$, β_{L_1} , and β_{L_2} .

Another parameterized correction, β_λ , is included in the cutoff wavelength λ_{c_1} as $\lambda_{c_1} + \beta_\lambda$. Inaccuracies in the waveguide dimensions due to the milling process can affect the value for the cutoff wavelength. In addition, the higher order model discussed below requires an additional wavelength cutoff value, λ_{c_2} , for a higher mode solution. Since it is not known *a priori* which higher modes will be present, a variation in λ_{c_2} from $0 < \lambda_{c_2} \leq \lambda_{c_1} + \beta_\lambda$, enables the solution procedure to find the value for λ_{c_2} that best improves the S -parameter approximation for the higher order terms.

One can formulate an invariant model with respect to reference planes for the problem discussed here, as suggested in [1], to remove uncertainty in L_1 and in L_2 . This approach uses Eq. (3) or (4), and the determinant of the S -matrix,

$$\det(S) = S_{11}S_{22} - S_{12}S_{21},$$

and solves for the parameters $A_1, \dots, A_4, B_1, \dots, B_4$. Simplification of $\det(S)$ yields a formula with neither L_1 nor L_2 . This reduced model remains dependent on a precise knowledge of both L_{air} and L and the cutoff wavelength, λ_{c_1} . This approach can be used interchangeably with the original model that contains L_1 and L_2 . The original model uses twice the number of observations and seems to produce more accurate approximations to the S -parameter data.

3.3 Higher Order Modes

In samples with a high dielectric constant, the observed S -parameter data may exhibit responses due to modes other than the fundamental mode. These responses are the result of resonances of the higher mode in the material. Earlier work does not include this information in the computation of μ_R^* and ϵ_R^* as higher modes are ignored. In this section we describe an enhancement to the previously defined model that does include higher order response data.

Because of the similarity between the response of the primary mode and the higher modes (see Sec. 4.4), an additional term is added to each of the

four equations (see Eqs. 2–5). This numerical model includes higher order mode structure in the S -parameter approximation and is a simple extension of the primary mode model described in Sec. 2.¹ The terms that approximate the higher order modes are identical to the primary mode term with the exception that each term is scaled. For the evaluation of the higher order terms, all input parameters are unchanged except for the parameter for the higher mode cutoff wavelength, λ_{c2} , that is allowed to decrease.

The explicit forms of the new set of equations use the Eqs. (2–5), and are denoted as D_{11} , D_{12} , D_{21} , and D_{22} . Associated with each higher order term is a scaling parameter, β_1, \dots, β_4 . In particular, to include the primary mode and one higher-order mode, the following approximate model is used:

$$D_{11} = S_{11}(\lambda_{c1}) + \beta_1 S_{11}(\lambda_{c2}), \quad (9)$$

$$D_{21} = S_{21}(\lambda_{c1}) + \beta_2 S_{21}(\lambda_{c2}), \quad (10)$$

$$D_{12} = S_{12}(\lambda_{c1}) + \beta_3 S_{12}(\lambda_{c2}), \quad (11)$$

$$D_{22} = S_{22}(\lambda_{c1}) + \beta_4 S_{22}(\lambda_{c2}), \quad (12)$$

where λ_{c2} is determined by ODRPACK.

3.4 The Initial Solution Procedure

In the Nicolson-Ross-Weir procedure (5, 7) the equations for the scattering parameters are combined to allow the system of equations to decouple. This decoupling yields an explicit equation for the permittivity and permeability as a function of the scattering parameters on a point-by-point basis. This solution procedure is the basis of the commonly used techniques for obtaining permittivity and permeability. Unfortunately, these equations are not well-behaved for low-loss materials at frequencies that correspond to integer multiples of one half wavelength in the sample.

The Nicolson-Ross-Weir procedure that is implemented provides a good initial approximation to A_1, A_3, B_1 and B_3 . All other parameters are initialized to zero. The estimated values for permittivity and permeability are determined on a point-by-point basis by frequency. The corresponding scattering parameters are computed with these values and then compared to the observed values. The computed values for μ_R^* and ϵ_R^* that provide the closest agreement between the observed and predicted S -parameter data are used as the initial values to the regression model.

¹ The justification of new terms added to each of Eqs. 2–5 is based solely on empirical evidence found when solving for the primary mode.

4. Numerical Considerations

4.1 ODRPACK Orthogonal Distance Regression Package

Briefly, ODRPACK [2] is an implementation of a trust region Levenberg-Marquardt algorithm. This type of trust region approach adaptively determines the region in which the linear approximation closely resembles the nonlinear model. The procedure allows both an ordinary least squares model, in which the uncertainties are assumed to be only in the dependent variable, and, an orthogonal distance regression model, where uncertainties also exist in the independent variables.

First order derivatives for the Jacobian matrices can be numerically approximated (finite difference approximation), or can be user-supplied analytical derivatives. The procedure performs automatic scaling of the variables if necessary, as well as determination the precision of the model in terms of machine precision. The ODRPACK includes many other features that assist the user in the modeling process. The model automatically determines the number of digits in the model, checks analytical derivatives provided by the user, and automatically selects many of the input parameters for the user, if desired.

Iterations are stopped in ODRPACK when any one of three stopping criteria is met. Two of these indicate that the iterations have converged to a solution. Sum-of-squares convergence indicates that the change in sum-of-squares observational uncertainty is sufficiently small. Parameter convergence indicates that the change in the estimated parameters is sufficiently small. The third stopping criterion is a limit on the number of iterations.

4.2 Initial Conditions

Many of the input options for ODRPACK can be set to their default values, as is done in this model. The most significant input parameters for modeling permittivity and permeability are the initial values for A_1, A_3, B_1 and B_3 . Sensitivity to the initial solution for these parameters is discussed below and the selection of initial settings is covered in Sec. 3.4. When higher modes are included, the solution for the primary mode is used as the initial guess for the higher mode model. For all of the parameters that define the physical model except those for μ_R^* and ϵ_R^* mentioned above, the standard laboratory values are used. All additional parameters are initialized to zero.

4.3 Sample Characteristics

A total of seven samples were modeled to determine permittivity and permeability with ANA two-port S -parameter data. The sample characteristics

appear in Table 1. Figure 2 contains selected plots of the observed ANA S -parameter data versus frequency for sample 6.

Table 1. Sample characteristics

	Material name	Identifier	Length (m)	L_1 (m)	L_2 (m)	Initial ϵ_R^*	Initial μ_R^*
1	Cross-linked polystyrene	rexa240889	2.407×10^{-2}	0.000	1.3208×10^{-3}	(2.53,0.002)	(1,0)
2	1723 glass	172a240889	1.015×10^{-2}	0.000	1.5250×10^{-2}	(6.15,0.04)	(1,0)
3	Loaded polymer	112a050290	2.540×10^{-2}	0.000	0.0000	(5.75,0.23)	(1.6,0.1)
4	Yttrium iron garnet	YIG	1.766×10^{-2}	0.000	7.7380×10^{-3}	(10,0.2)	(1,0.4)
5	Nickel ferrite	tt1a120490	1.013×10^{-2}	0.000	1.5263×10^{-2}	(11.5,0.1)	(0.85,0.1)
6	Barium titanate mix 1	barium	7.632×10^{-3}	0.000	1.7768×10^{-2}	(265,1)	(1,0)
7	Barium titanate mix 2	french	2.427×10^{-2}	0.000	1.1252×10^{-3}	(105,1)	(1,0)

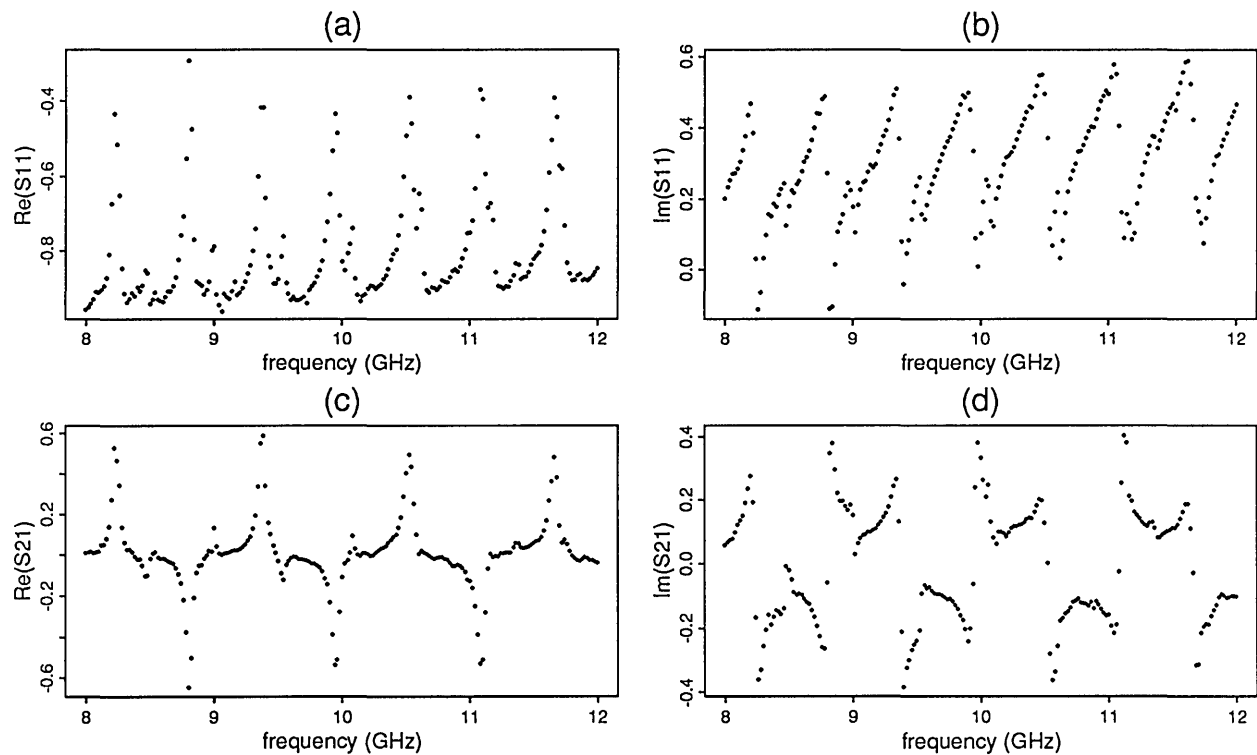


Figure 2. Barium titanate mix 1 (a) $\Re[S_{11}]$, (b) $\Im[S_{11}]$, (c) $\Re[S_{21}]$, (d) $\Im[S_{21}]$.

4.4 Numerical Results

The first results reported are those for the primary mode model for all seven samples described in Sec. 4.3. The first set of plots (Fig. 3) include the observed S -parameter data (dots) for the YIG sample (sample 4) from the ANA overlaid by the predicted data (line) found by the model. The corresponding residual plots² for this sample appear in Fig. 4.

For the first four samples the predicted and observed data are nearly identical. The residual plot for cross-linked polystyrene (sample 1) as shown in Fig. 5 reveals the systematic uncertainty due to the ANA.

Fig. 6 illustrates a S -parameter primary mode solution for barium titanate mix 1 with a high dielectric constant and its corresponding residual

plot. For three of the samples with high dielectric constants, the new model produces responses for the primary and one of the higher modes. See Fig. 7 for the S -parameter real and imaginary components of S_{21} for the sample exhibited in Fig. 6 with the model for higher order modes.

For samples 5, 6, and 7 the predicted S -parameter data provide realistic primary mode responses although the residual plots for these samples indicate that higher modes are present. With the higher order model described in Sec. 3.3 and the new solution found, the problem is resolved for the last three samples. The new solution specifies the additional parameters β_1, \dots, β_4 . Fig. 8 shows the results from the higher order model for sample 5. Additional work in this area suggests that this model is only an approximation.

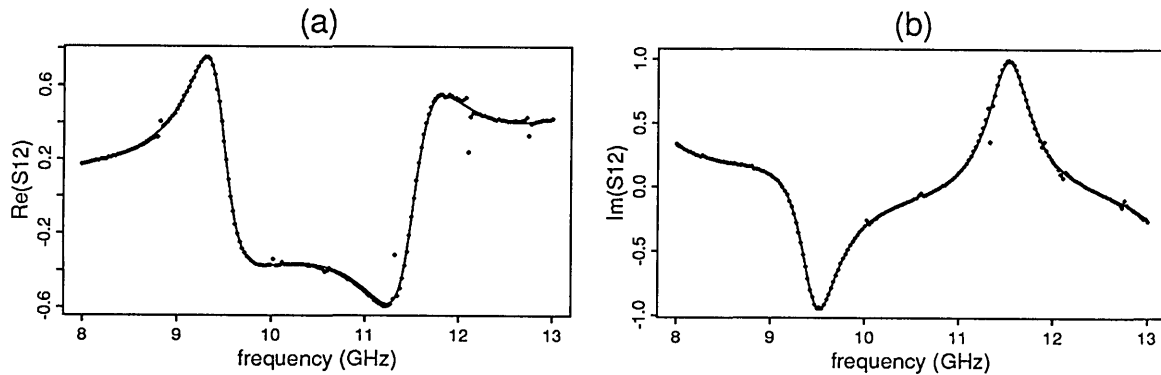


Fig. 3. Yttrium iron garnet predicted and observed: (a) $\Re[S_{12}]$, (b) $\Im[S_{12}]$.

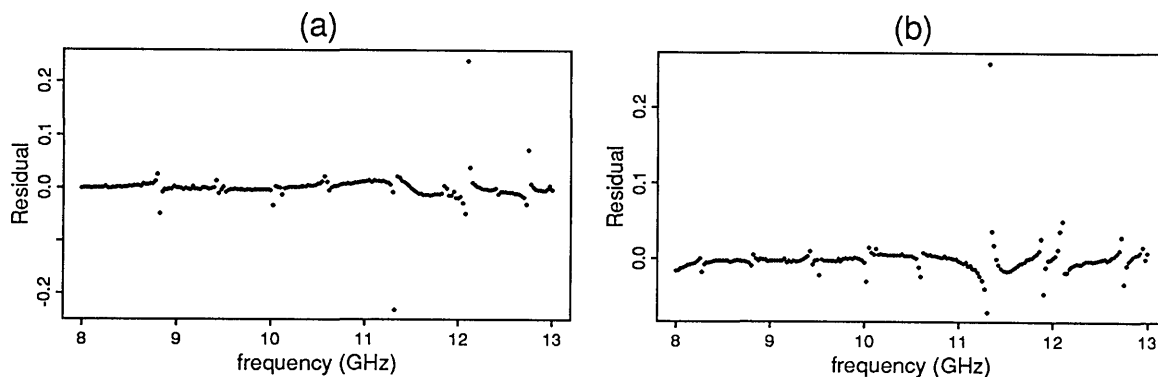


Fig. 4. Yttrium iron garnet residual plots: (a) $\Re[S_{12}]$, (b) $\Im[S_{12}]$.

² A "residual plot" denotes a plot of the difference between the predicted and observed S -parameter data over the range of observations.

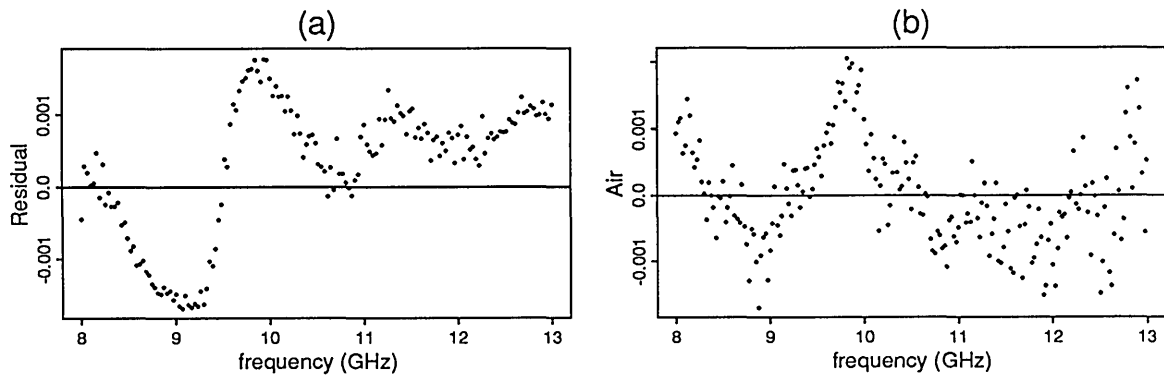


Figure 5. (a) Residual plots of $\Im[S_{22}]$ for cross-linked polystyrene (b) $\Im[S_{22}]$ for an empty waveguide.

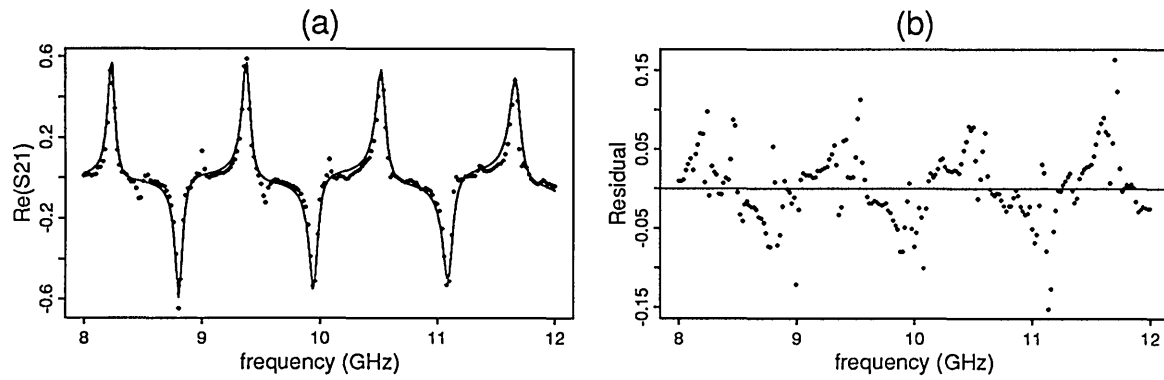


Figure 6. Barium titanate mix 1 (a) predicted and observed $\Re[S_{21}]$ (b) residual plot.

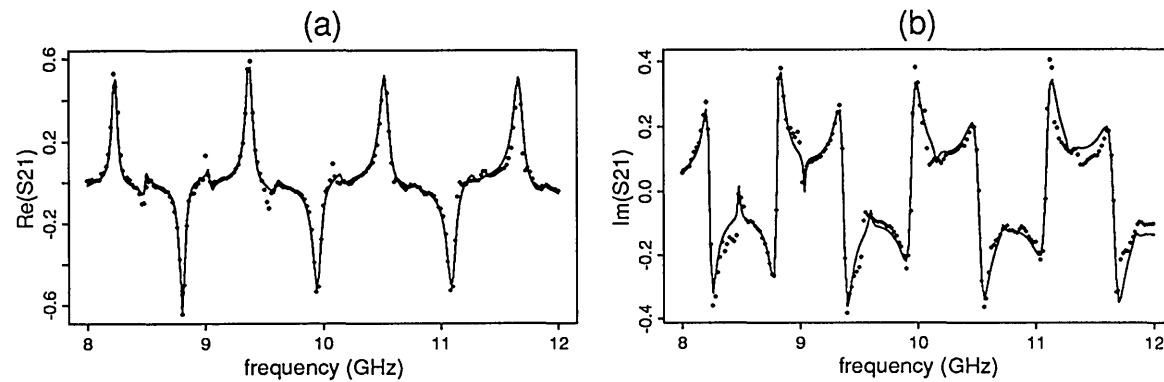


Figure 7. Barium titanate mix 1 (a) predicted and observed $\Re[S_{21}]$ (b) predicted and observed $\Im[S_{21}]$.

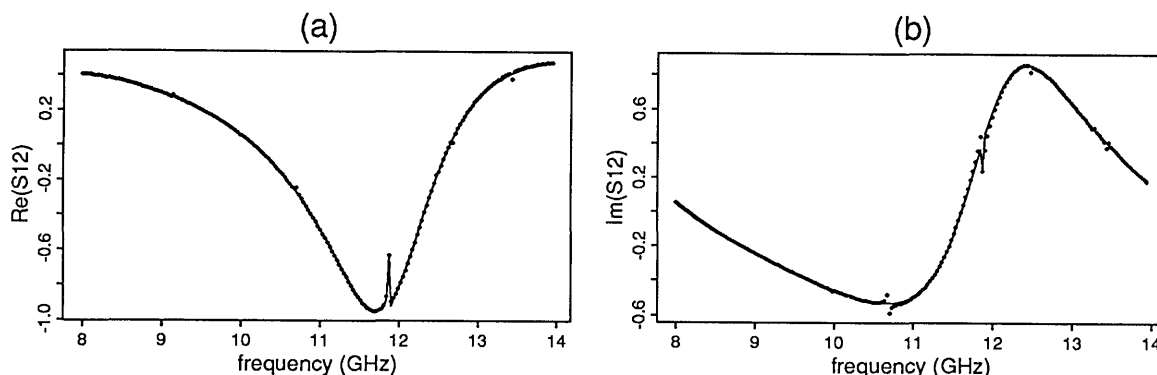


Figure 8. Nickel ferrite (a) predicted and observed $\Re[S_{12}]$ (b) predicted and observed $\Im[S_{12}]$.

4.5 ANA Systematic Uncertainty

The difference of the predicted S -parameter and the observed values for samples with low dielectric values revealed systematic uncertainty. (For the high dielectric samples, other sources of uncertainty including higher mode responses dominate the ANA-induced uncertainty.) Additional tests revealed that the source of the uncertainty is not related to the material tested in the waveguide. In fact, uncertainties in the S -parameter data for the cross-linked polystyrene sample closely resemble the S -parameter data for an empty waveguide. Attempts to further identify and remove the systematic uncertainty are underway. Figure 5 contains the S_{11} data for an empty waveguide and also the residual plot for the cross-linked polystyrene sample.

4.6 Permittivity and Permeability Estimates

The estimates of permeability and permittivity for the various samples are defined by the parameters $A_1, \dots, A_4, B_1, \dots, B_4$ as a function of frequency. Several of the samples are magnetic (see Table 1). For these samples the permeability was allowed to vary, with ODRPACK required to determine the $(1,0)$ value. Slight variations in the value of permeability are apparent although the deviation from the true value is small. The solution procedure also provides the standard deviation and confidence intervals for each of the estimated parameters.

4.7 Robustness of the ODRPACK Procedure

The robustness of a mathematical procedure is its ability to find a locally optimal solution from a varied initial condition. The robustness of the entire permeability and permittivity procedure depends on the robustness of the ODRPACK procedure and, more significantly, the robustness of the math-

ematical model. The existence of alternative optima in the mathematical model can limit the range of the initial conditions to produce a particular solution. In addition, singularities in the absence of alternative optima may force the solution procedure to fail to determine directions of improvement and cause a premature termination.

For the samples in this study, variability in the robustness of the procedure depended on the sample studied. For the materials with small dielectric constant, the procedure readily determined the correct solution for a variety of initial conditions. For materials with higher dielectric constant, the procedure often converged quickly, although the existence of alternative optima in the mathematical model often required the repeated solution with varied initial conditions before an acceptable solution was found.

In particular, for the cross-linked polystyrene sample, initial values for μ_R^* and ϵ_R^* were set to $(1,0)$ and $(1,0)$ and were constant over the entire frequency range. The solution $(1,0), (2.517, 0.0018)$ was found after 50 iterations of the solution procedure. Initial conditions of $(1,0)$, and $(4.0, 0.01)$ failed to determine a solution, while altering the imaginary part of ϵ_R^* to 1×10^{-4} resulted in the desired final solution once again. For material with high dielectric constants, the range was smaller. For example for the barium titanate mix 1, initial conditions of $(1,0,0)$ and $(200,0,1,0)$ produced the converged value of $(1,0)$ and $(269,0,1,70)$ in 59 iterations.

One should note that the solution procedure can change the value of the estimated parameters by large amounts in the early iterations. Hence it is possible that for cross-linked polystyrene an initial solution farther from the desired solution may in fact find a solution merely because of the solution path taken by the procedure.

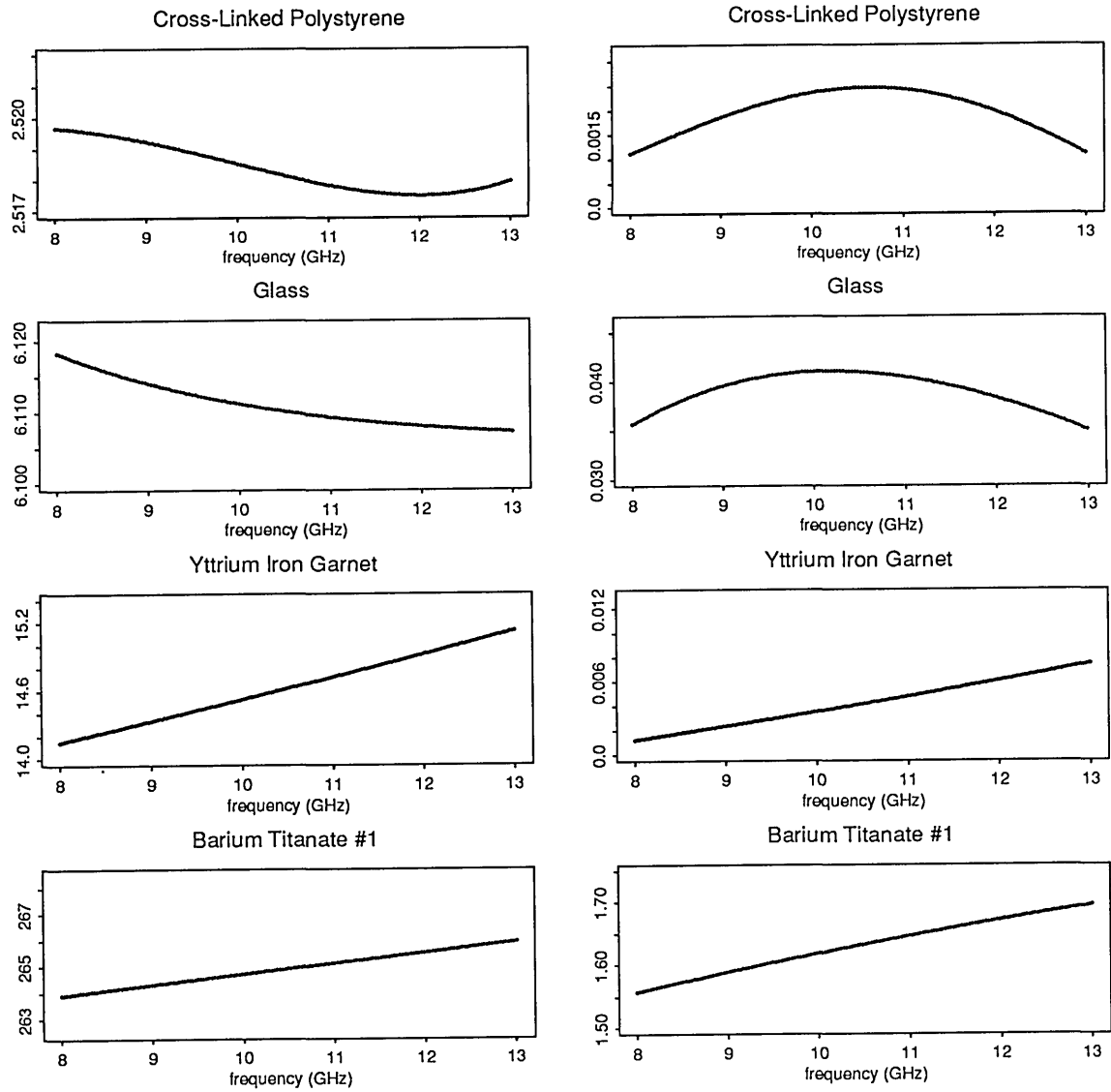


Figure 9. Selected plots of $\epsilon_R^*(\omega)$ for various samples.

5. Conclusions and Future Directions

The nonlinear optimization procedure using two-port scattering parameters determined permittivity and permeability for a large number of samples (see Fig. 9). The added capability that permits variations in certain input parameters provides a mechanism to adjust for measurement uncertainties. The extension of the model to include higher order mode responses is quite useful for high dielectric constant materials.

About the authors: Paul D. Domich is a mathematician in the Applied and Computational Mathematics Division of the NIST Computing and Applied Mathematics Laboratory. James Baker-Jarvis and Richard G. Geyer are physicists in the Electromagnetics Fields Division of the NIST Electronics and Electrical Engineering Laboratory.

6. References

- [1] J. Baker-Jarvis, Transmission/Reflection and Short-Circuit Line Permittivity Measurements, NIST Technical Note 1341 (1990).
- [2] P. T. Boggs, J. R. Donaldson, R. H. Byrd, and R. B. Schnabel, Algorithm 676 ODRPACK: Software for Weighted Orthogonal Distance Regression, ACM Trans. Math. Software 15, 348–364 (1989).
- [3] H. E. Bussey, Measurement of RF Properties of Materials: A Survey, Proc. IEEE 55, 1046–1053 (1967).
- [4] R. G. Geyer, Dielectric Characterization and Reference Materials, NIST Technical Note 1338 (1990).
- [5] A. M. Nicolson, and G. F. Ross, Measurement of the Intrinsic Properties of Materials by Time Domain Techniques, IEEE Transactions on Instrumentation Measurement IM-19/ November 1970, 377–382.
- [6] S. Roberts, and A. von Hippel, A New Method for Measuring Dielectric Constant and Loss in the Range of Centimeter Waves, J. Appl. Phys. 7, 610–616 (1946).
- [7] W. B. Weir, Automatic Measurement of Complex Dielectric Constant and Permeability at Microwave Frequencies, Proc. IEEE 62, 33–36 (1974).

Taguchi's Orthogonal Arrays Are Classical Designs of Experiments

Volume 96

Number 5

September–October 1991

**Raghu N. Kacker,
Eric S. Lagergren, and
James J. Filliben**

National Institute of Standards
and Technology,
Gaithersburg, MD 20899

Taguchi's catalog of orthogonal arrays is based on the mathematical theory of factorial designs and difference sets developed by R. C. Bose and his associates. These arrays evolved as extensions of factorial designs and latin squares. This paper (1) describes the structure and constructions of Taguchi's orthogonal arrays, (2) illustrates their fractional factorial nature, and (3) points out that

Taguchi's catalog can be expanded to include orthogonal arrays developed since 1960.

Key words: difference sets; fractional factorial plans; orthogonal arrays; Taguchi's methods.

Accepted: June 5, 1991

1. Introduction

Today many engineers are using Taguchi's catalog of orthogonal arrays [1] to plan industrial experiments. But Taguchi provides either no information or insufficient information on the methods that were used to construct these arrays. Moreover, Taguchi displays orthogonal arrays in forms that are different from the way these arrays are usually displayed in the statistical literature. It is, therefore, difficult to discern the links between Taguchi's arrays and their counterparts published elsewhere. Recent advertisements and testimonials of the efficacy of experiments based on Taguchi's orthogonal arrays increase the confusion by giving an impression that these arrays are something other than fractional factorials and classical plans of experiments. This paper describes the structure and constructions of Taguchi's orthogonal arrays, illustrates their fractional factorial nature, and points out that his catalog can be expanded to include orthogonal arrays developed since 1960.

The next section of this paper provides the background of orthogonal arrays and introduces the

concept that an orthogonal array can be displayed in one of many equivalent forms. This concept is subsequently used to exhibit the equivalence of certain well-known fractional factorial plans and Taguchi's orthogonal arrays. Taguchi's catalog contains 20 arrays. However, only 18 of these arrays are orthogonal arrays. These 18 orthogonal arrays are the focus of this paper, and they have been classified into eight groups defined in such a way that the orthogonal arrays in each group can be constructed by a common method. The subsequent eight sections are devoted to these eight specific groups. In these sections, first the constructions of Taguchi's orthogonal arrays are described and then these arrays are related to fractional factorials and other well-known orthogonal arrays. In order to appreciate the factorial nature of Taguchi's orthogonal arrays, it is necessary to understand the constructions of these arrays. The last section of this paper identifies several useful orthogonal arrays that are not in Taguchi's catalog because they were developed after 1960.

2. The Background of Orthogonal Arrays

An *orthogonal array* (more specifically a fixed-element orthogonal array) of s elements, denoted by $OA_N(s^m)$, is an $N \times m$ matrix whose columns have the property that in every pair of columns each of the possible ordered pairs of elements appears the same number of times. The symbols used for the elements of an orthogonal array are arbitrary. This paper uses the symbols $(0,1,2,\dots,s-1)$ to denote the s elements. Tables 1 and 2 display $OA_4(2^3)$ and $OA_8(2^7)$ respectively. Note that in every pair of columns of table 1 each of the 4 ordered pairs $(0,0)$, $(0,1)$, $(1,0)$, and $(1,1)$ appears exactly once. Similarly, every pair of columns in table 2 contains each of the four pairs $(0,0)$, $(0,1)$, $(1,0)$, and $(1,1)$ exactly twice. Taguchi refers to $OA_N(s^m)$ by the notation $L_N(s^m)$. The letter L in this notation stands for latin square, and it indicates that orthogonal arrays are generalized latin squares. Taguchi uses the symbols $(1,2,\dots,s)$ to denote the elements of an orthogonal array. The authors have, however, used the symbols $(0,1,\dots,s-1)$ in this paper because these symbols are natural in light of the methods of constructing these arrays.

Table 1. Orthogonal array $OA_4(2^3)$

Row No.	Column No.		
	1	2	3
1	0	0	0
2	0	1	1
3	1	0	1
4	1	1	0

Table 2. Orthogonal array $OA_8(2^7)$

Row No.	Column No.						
	1	2	3	4	5	6	7
1	0	0	0	0	0	0	0
2	0	0	0	1	1	1	1
3	0	1	1	0	0	1	1
4	0	1	1	1	1	0	0
5	1	0	1	0	1	0	1
6	1	0	1	1	0	1	0
7	1	1	0	0	1	1	0
8	1	1	0	1	0	0	1

Orthogonal arrays can be viewed as plans of multifactor experiments where the columns correspond to the factors, the entries in the columns correspond to the test levels of the factors and the rows correspond to the test runs. More specifically, the N rows of an $OA_N(s^m)$ can be viewed as a subset of the possible s^m test runs of a complete factorial plan in m factors each having s test levels. Thus, an $OA_N(s^m)$ can be viewed as a N/s^m fraction of a complete s^m factorial plan. For example, the four rows of the $OA_4(2^3)$ that are displayed in Table 1, can be viewed as a $4/2^3 = 1/2$ fraction of a complete 2^3 factorial plan.

A sub-matrix formed by deleting some columns of an orthogonal array is also an orthogonal array. Thus, by deleting certain columns of a given orthogonal array, it is possible to generate many different plans of multifactor experiments.

A fractional factorial plan that enables uncorrelated estimation of every factorial effect included in the underlying linear model assuming that all other effects are zero is called an orthogonal plan. Fractional factorial plans based on orthogonal arrays irrespective of the degree of fractionation are necessarily orthogonal plans. This is the primary reason for the popularity of fractional factorials based on orthogonal arrays.

Some of the most popular arrays in Taguchi's catalog are mixed-element (level) orthogonal arrays. A *mixed-element orthogonal array*, denoted by $OA_N(s^m \times t^n)$, is a matrix of N rows and $m+n$ columns in which the first m columns have s elements each, the next n columns have t elements each, and in every pair of columns each of the possible ordered pairs of elements appears a constant number of times. The constant, however, depends on the pair of columns selected. Table 3 displays two orthogonal arrays: $OA_{18}(6^1 \times 3^6)$ and $OA_{18}(2^1 \times 3^7)$. Note that every pair of columns in Table 3 contains each of the possible ordered pairs a constant number of times. A mixed-level orthogonal array can be viewed as a fractionated multilevel factorial plan.

It follows from the definition of an orthogonal array that an orthogonal array remains an orthogonal array when its (1) rows are permuted or (2) columns are permuted or (3) the elements within a column are permuted. When orthogonal arrays are viewed as plans of multifactor experiments, the row permutation corresponds to reordering of test runs, the column permutation corresponds to relabeling of factors, and the permutation of elements within a column corresponds to relabeling of factor levels. Most experimenters realize that the labels of factors,

Table 3. Orthogonal arrays $OA_{18}(6^1 \times 3^6)$ and $OA_{18}(2^1 \times 3^7)^a$

Row No.	Column No.								
	1'	1	2	3	4	5	6	7	8
1	0	0	0	0	0	0	0	0	0
2	0	0	0	1	1	1	1	1	1
3	0	0	0	2	2	2	2	2	2
4	1	0	1	0	0	1	1	2	2
5	1	0	1	1	1	2	2	0	0
6	1	0	1	2	2	0	0	1	1
7	2	0	2	0	1	0	2	1	2
8	2	0	2	1	2	1	0	2	0
9	2	0	2	2	0	2	1	0	1
10	3	1	0	0	2	2	1	1	0
11	3	1	0	1	0	0	2	2	1
12	3	1	0	2	1	1	0	0	2
13	4	1	1	0	1	2	0	2	1
14	4	1	1	1	2	0	1	0	2
15	4	1	1	2	0	1	2	1	0
16	5	1	2	0	2	1	2	0	1
17	5	1	2	1	0	2	0	1	2
18	5	1	2	2	1	0	1	2	0

^a Columns 1',3,4,5,6,7, and 8 form $OA_{18}(6^1 \times 3^6)$.
Columns 1,2,3,4,5,6,7, and 8 form $OA_{18}(2^1 \times 3^7)$.

the labels of factor levels and the order of test runs are arbitrary. Indeed, the order of test runs is usually randomized. Therefore, two orthogonal arrays are defined to be *equivalent* if one can be obtained from the other via the following permutations: (1) the rows are permuted, (2) the columns are permuted, and (3) the elements (symbols) within a column are permuted (for example, in a three-element column, the elements (0,1, and 2) can be replaced with any one of their permutations: (0,2, and 1); (1,0, and 2); (1,2 and 0); (2,0, and 1); or (2,1, and 0) respectively).

Taguchi's format for an orthogonal array has the property that the entries in the left most columns change less frequently than the entries in the right most columns. Therefore, when these arrays are used to plan multifactor experiments, the cost of running the experiment can sometimes be reduced by judiciously associating with the left most columns those factors that are most expensive or most difficult to vary.

Taguchi's catalog contains twenty arrays. However, only eighteen of these twenty arrays are orthogonal arrays. The remaining two arrays, denoted by $L'_9(2^{21})$ and $L'_{27}(3^{22})$, are not orthogonal arrays and they are not discussed in this paper. The eighteen orthogonal arrays are classified into eight groups based on the common method of construction. The next eight sections are devoted to these eight groups.

3. Two-Element Orthogonal Arrays of 2^r Rows for $r = 2,3,4,5$, and 6

The fractional factorial nature of two-element (level) orthogonal arrays follows from the way these arrays are constructed. So this section first describes a simple method of constructing these arrays, then illustrates their fractional factorial nature. A complete two-element orthogonal array with 2^r rows has $2^r - 1$ columns and it is constructed column by column in three steps.

Step 1: Write in the r columns specified by column numbers 1,2,4,8,..., 2^{r-1} a complete factorial plan in r factors each having two test levels represented by 0 and 1 respectively. In order to match Taguchi's display format, write this plan in such a way that the entries of the left most columns change less frequently than the entries of the right most columns. The entries of these r columns are used to calculate and define the entries of the remaining columns. Therefore, these r columns are referred to as the basic columns and marked as x_1, x_2, \dots, x_r , respectively.

Step 2: These basic columns are used to generate the other columns. The generator of a particular column is a rule of the form $a_1x_1 + a_2x_2 + \dots + a_r x_r$ where x_1, x_2, \dots, x_r are the r basic columns and the coefficients a_1, a_2, \dots, a_r are obtained from the appropriate row of table 4. [For example, in the construction of $OA_8(2^7)$ discussed below, the coefficients a_1, a_2, \dots , and a_3 for column 5 are in the fifth row of table 4 and have the values 1, 0, and 1 respectively. This yields $x_1 + x_3$ as the generator for column 5 of $OA_8(2^7)$]. List the generators in the order of column numbers.

Step 3: Compute the entries of the other columns by using the generators identified in step 2. The required calculations are performed in modulo 2 arithmetic (that is, $0+0 = 0$, $0+1 = 1$, $1+0 = 1$ and $1+1 = 0$).

This method of construction and analogous methods of constructing three-, four-, and five-element orthogonal arrays are based on the mathematical theory of fractional factorials developed by Bose [2].

Table 4. Coefficients of the generators of two-element orthogonal arrays of 2^r rows for $r = 2, 3, \dots$

Column No.	Coefficients of $x_1, x_2, x_3, \dots, x_r$					
	a_1	a_2	a_3	...	a_{r-1}	a_r
1	1	0	0	First $(2^{r-2}-1)$	First $(2^{r-1}-1)$	
2	0	1	0	entries are 0	entries are 0	
3	1	1	0	Next (2^{r-2})	Last (2^{r-1})	
4	0	0	1	entries are 1	entries are 1	
5	1	0	1	Next (2^{r-2})		
6	0	1	1	entries are 0		
7	1	1	1	Last (2^{r-2})		
.	Repeat	Repeat		entries are 1		
.	(0,1)	(0,0,1,1)				
2^r-2	0	1	1			
2^r-1	1	1	1			

The following example illustrates these steps.

Example: Construction of an $OA_8(2^7)$

Here $N = 8 = 2^3$, so $r = 3$.

Step 1: Write the $r = 3$ basic columns.

Column No.	1	2	3	4	5	6	7
Row No.							
1		0	0	0			
2		0	0	1			
3		0	1	0			
4		0	1	1			
5		1	0	0			
6		1	0	1			
7		1	1	0			
8		1	1	1			
Generator	x_1	x_2	x_3				

Step 2: List the generators (see rows 1 to 7 of table 4).

Column No.	Generator
1	x_1
2	x_2
3	x_1+x_2
4	x_3
5	x_1+x_3
6	x_2+x_3
7	$x_1+x_2+x_3$

Step 3: Complete the array using the generators identified in step 2.

Column No.	1	2	3	4	5	6	7
Row No.							
1	0	0	0	0	0	0	0
2	0	0	0	1	1	1	1
3	0	1	1	0	0	1	1
4	0	1	1	1	1	0	0
5	1	0	1	0	1	0	1
6	1	0	1	1	0	1	0
7	1	1	0	0	1	1	0
8	1	1	0	1	0	0	1

The fractional factorial nature of Taguchi's two-element orthogonal arrays stems from the fact that the entries of the r columns identified by column numbers $1, 2, 4, 8, \dots, 2^{r-1}$ form a complete factorial plan, and the remaining columns correspond to the interaction effects. The generators of these columns have a one-to-one correspondence with the main effects and the interaction effects written in Yates' [3] standard order. The r basic columns correspond to the main effects and the remaining columns correspond to the interaction effects.

A two-element (two-level) orthogonal array with 2^r rows reduces to a fractional factorial plan when more than r factors are associated with the columns of the array and the remaining columns are deleted. In particular, when all $2^r - 1$ columns are associated with an equal number of factors, a two-level orthogonal array $OA_N(2^m)$ where $N = 2^r$ represents a $N/2^m = (1/2)^{m-r}$ fraction of a complete 2^m factorial plan. For example, an $OA_8(2^7)$ represents a $(1/2)^{7-3} = (1/2)^4 = 1/16$ th fraction of a complete 2^7 factorial plan. That is, an $OA_8(2^7)$ represents a 2^{7-4} plan in factorial notation.

The test levels of 2^{k-p} type fractional factorial plans are usually represented [4] by the symbols $-$ and $+$. Such plans are often constructed by writing a complete factorial plan in the required number of test runs and appending additional columns obtained by multiplying certain columns of the complete factorial plan. This method and the Bose method of constructing two-level orthogonal arrays described here are similar, but since $(- \times - = +, - \times + = -, \text{ and } + \times + = +)$ while $(0+0=0, 0+1=1, \text{ and } 1+1=0)$ in modulo 2 arithmetic, the two methods yield different fractions of the same type. However, one fraction can be obtained from another of the same type by switching the test levels, and permuting the rows and columns. For example, Taguchi's $OA_8(2^7)$ can be obtained from Box, Hunter, and Hunter's 2^{7-4} plan [4] (shown as table 12.5 on page 391 of their book) by switching $-$ and $+$ in columns 4, 5 and 6; permuting the columns in the order 3,2,6,1,5,4, and 7; and relabeling $-$ as 0 and $+$ as 1.

4. Two-Element Orthogonal Array $OA_{12}(2^{11})$

Table 5 displays Taguchi's $OA_{12}(2^{11})$ in the 0 and 1 notation, and table 6 displays the classic Plackett and Burman [5] plan of 12 runs in the 0 and 1 notation rather than the usual $-$ and $+$ notation. Since table 5 can be obtained

from table 6 through the following permutations, Taguchi's $OA_{12}(2^{11})$ and the Plackett and Burman plan of 12 runs are equivalent.

- (1) In table 6 switch the elements 0 and 1 of columns 1,2,4,5,7, and 11 (that is, substitute 1 for 0 and 0 for 1 in these columns).
- (2) Permute the rows in the following order: 5,2,6,10,4,1,3,7,11,8,12,9.
- (3) Permute the columns in the following order: 1,2,3,4,6,5,9,10,8,7,11.

Table 5. Orthogonal array $OA_{12}(2^{11})$

Row No.	Column No.										
	1	2	3	4	5	6	7	8	9	10	11
1	0	0	0	0	0	0	0	0	0	0	0
2	0	0	0	0	0	1	1	1	1	1	1
3	0	0	1	1	1	0	0	0	1	1	1
4	0	1	0	1	1	0	1	1	0	0	1
5	0	1	1	0	1	1	0	1	0	1	0
6	0	1	1	1	0	1	1	0	1	0	0
7	1	0	1	1	0	0	1	1	0	1	0
8	1	0	1	0	1	1	1	0	0	0	1
9	1	0	0	1	1	1	0	1	1	0	0
10	1	1	1	0	0	0	0	1	1	0	1
11	1	1	0	1	0	1	0	0	0	1	1
12	1	1	0	0	1	0	1	0	1	1	0

Table 6. Plackett and Burman plan of 12 rows

Row No.	Column No.										
	1	2	3	4	5	6	7	8	9	10	11
1	1	0	1	0	0	0	1	1	1	0	1
2	1	1	0	1	0	0	0	1	1	1	0
3	0	1	1	0	1	0	0	0	1	1	1
4	1	0	1	1	0	1	0	0	0	1	1
5	1	1	0	1	1	0	1	0	0	0	1
6	1	1	1	0	1	1	0	1	0	0	0
7	0	1	1	1	0	1	1	0	1	0	0
8	0	0	1	1	1	0	1	1	0	1	0
9	0	0	0	1	1	1	0	1	1	0	1
10	1	0	0	0	1	1	1	0	1	1	0
11	0	1	0	0	0	1	1	1	0	1	1
12	0	0	0	0	0	0	0	0	0	0	0

5. Three-Element Orthogonal Arrays of 3^r Rows for $r = 2, 3,$ and 4

A complete three-element orthogonal array with 3^r rows has $(3^r - 1)/(3 - 1)$ columns and it is constructed in three steps:

Step 1: Write in the r columns specified by column numbers 1,2,5,14,...,($3^{r-1} - 1$)/($3 - 1$) + 1 a complete factorial plan in r factors each having three test levels represented by 0, 1, and 2, respectively. In order to match Taguchi's display format, write this plan in such a way that the entries of the left-most columns change less frequently than do the entries of the right-most columns. Mark these columns as x_1, x_2, \dots, x_r , respectively.

Step 2: As before the generators of the remaining columns are of the form $a_1x_1 + a_2x_2 + \dots + a_rx_r$ where x_1, x_2, \dots, x_r denote the r basic columns and the coefficients a_1, a_2, \dots, a_r for a particular column are given in the appropriate row of table 7. List the generators in the order of column numbers.

Step 3: Compute the entries of the remaining columns by using the entries of the r basic columns and the appropriate generators. All calculations are done in modulo 3 arithmetic (that is, an integer larger than or equal to three is replaced with its remainder after division by three).

Table 7. Coefficients of the generators of three-element orthogonal arrays of 3^r rows for $r = 2, 3, \dots$

Column No.	Coefficients of $x_1, x_2, x_3, \dots, x_r$				
	a_1	a_2	...	a_{r-1}	a_r
1	1	0	First $(3^{r-2} - 1)/(3 - 1)$	First $(3^{r-1} - 1)/(3 - 1)$	First $(3^{r-1} - 1)/(3 - 1)$
2	0	1	entries are 0	entries are 0	entries are 0
3	1	1	Next (3^{r-2})	Last (3^{r-1})	Last (3^{r-1})
4	2	1	entries are 1	entries are 1	entries are 1
.	Repeat	Repeat	Next (3^{r-2})	entries are 0	entries are 0
.	(0,1,2)	(0,0,0)	Next (3^{r-2})	entries are 1	entries are 1
.	.	1,1,1	Next (3^{r-2})	entries are 1	entries are 1
.	.	2,2,2	Next (3^{r-2})	entries are 1	entries are 1
.	.	.	Last (3^{r-2})	entries are 2	entries are 2
.	.	.	entries are 2	entries are 2	entries are 2
($3^r - 1$)/($3 - 1$)	2	2			

The following example illustrates these steps.
 Example: Construction of an $OA_9(3^4)$
 Here $N = 9 = 3^2$, so $r = 2$.

Step 1: Write the $r = 2$ basic columns

Column No.	1	2	3	4
Row No.				
1	0	0		
2	0	1		
3	0	2		
4	1	0		
5	1	1		
6	1	2		
7	2	0		
8	2	1		
9	2	2		
Generator	x_1	x_2		

Step 2: List the generators (see rows 1 to 4 of table 7).

Column No.	Generator
1	x_1
2	x_2
3	$x_2 + x_1$
4	$x_2 + 2x_1$

Step 3: Complete the array using the generators identified in step 2.

Column No.	1	2	3	4
Row No.				
1	0	0	0	0
2	0	1	1	1
3	0	2	2	2
4	1	0	1	2
5	1	1	2	0
6	1	2	0	1
7	2	0	2	1
8	2	1	0	2
9	2	2	1	0

The fractional factorial nature of Taguchi's three-element orthogonal arrays stems from the fact that the entries of the r basic columns identified by column numbers, $1, 2, 5, 14, \dots, (3^{r-1} - 1)/(3 - 1) + 1$ form a complete factorial plan and the other columns correspond to the interaction effects. Since each column contains three distinct elements, two degrees of freedom are associated with each column. Since pairwise interaction effects carry $(3 - 1) \times (3 - 1) = 4$ degrees of freedom, two columns correspond to each pairwise interaction effect. An interaction effect involving k factors carries $(3 - 1)^k = 2^k$ degrees of freedom. Therefore, 2^{k-1} columns correspond to each interaction effect involving k factors for $k = 2, 3, 4, \dots$.

A three-element (level) orthogonal array with 3^r rows reduces to a fractional factorial plan when more than r factors are associated with the columns of the array and the remaining columns are deleted. In particular, when all $(3^r - 1)/(3 - 1)$ columns are associated with an equal number of factors, a three-level orthogonal array $OA_N(3^m)$ where $N = 3^r$ and $m = (3^r - 1)/(3 - 1)$ represents a $N/3^m = (1/3)^{m-r}$ fraction of a complete 3^m factorial plan. For example, an $OA_9(3^4)$ represents a $(1/3)^2$ fraction of a complete 3^4 factorial plan. That is, an $OA_9(3^4)$ represents a 3^{4-2} plan in factorial notation.

6. Four-Element Orthogonal Arrays of 4^r Rows for $r = 2$ and 3

The method of constructing four-element orthogonal arrays is similar to the method for three-element arrays. An important difference, however, is that the calculations required to generate the columns are not performed in modulo 4 arithmetic. Instead, special addition and multiplication tables, displayed here as tables 9 and 10 are used. These addition and multiplication tables are based on the "finite arithmetic of the Galois Field Theory" that underlies this method of construction. According to this theory, the calculations required to generate an orthogonal array of s elements are done in modulo s arithmetic when s is a prime number, as is the case with 2, 3, and 5. When s is a power of a prime number such as 4 (which is the square of prime number 2), finite arithmetic of a Galois Field of s elements is used. A four-element orthogonal array with 4^r rows and $(4^r - 1)/(4 - 1)$ columns is constructed in three steps.

Step 1: Write in the r columns specified by column numbers $1, 2, 6, \dots, (4^{r-1} - 1)/(4 - 1) + 1$ a complete factorial plan in r factors each having four test levels represented by 0, 1, 2, and 3, respectively. Write this plan in Taguchi's format, and mark these columns as x_1, x_2, \dots, x_r , respectively.

Step 2: As before the generators of the remaining columns are of the form $a_1x_1 + a_2x_2 + \dots + a_r x_r$ where x_1, x_2, \dots, x_r denote the r basic columns and the coefficients a_1, a_2, \dots, a_r for a particular column are given in the appropriate row of table 8. List the generators in the order of column numbers.

The entries of the r basic columns identified by column numbers $1, 2, 6, \dots, (4^{r-1} - 1)/(4 - 1) + 1$ form a complete factorial plan and the other columns correspond to the interaction effects. Since each column contains four distinct elements, three degrees of freedom are associated with each column. An interaction effect involving k factors carries $(4 - 1)^k = 3^k$ degrees of freedom. Therefore, 3^{k-1} columns correspond to each interaction effect involving k factors. In particular, three columns correspond to each pairwise interaction effect.

When all $(4^r - 1)/(4 - 1)$ columns are associated with factors, a four-element (four-level) array $OA_N(4^m)$ where $N = 4^r$ and $m = (4^r - 1)/(4 - 1)$ represents a $N/4^m = (1/4)^{m-r}$ fraction of a complete 4^m factorial plan. For example, $OA_{16}(4^5)$ represents a $(1/4)^3$ fraction of a complete 4^5 factorial plan.

7. Five-Element Orthogonal Array $OA_{25}(5^6)$

Taguchi's $OA_{25}(5^6)$ is constructed through the same general approach that is used to construct 2-, 3-, and 4-element arrays. The first two columns form a complete factorial plan in two factors each having five test levels represented by 0, 1, 2, 3, and 4. The other columns are generated from these two columns using the following generators where x_1 and x_2 represent the entries of the first two columns.

Column No.	Generator
1	x_1
2	x_2
3	$x_2 + x_1$
4	$x_2 + 2x_1$
5	$x_2 + 3x_1$
6	$x_2 + 4x_1$

All calculations are done in modulo 5 arithmetic. When the six columns of an $OA_{25}(5^6)$ are associated with an equal number of factors, then $OA_{25}(5^6)$ represents a $(1/5)^4$ fraction of a complete 5^6 factorial plan.

8. Mixed-element Orthogonal Arrays $OA_{18}(2^1 \times 3^7)$, $OA_{32}(2^1 \times 4^9)$ and $OA_{50}(2^1 \times 5^{11})$

These orthogonal arrays are constructed by the method of Bose and Bush [6]. This method involves four concepts: difference matrices, Kronecker sums, saturated orthogonal arrays, and column replacement.

1) A *difference matrix* of s elements $0, 1, \dots, (s - 1)$, denoted by $D_M(s)$, is an $M \times M$ matrix whose columns have the property that the differences in finite arithmetic between any two columns is a column in which each of the s elements occurs equally often. Table 11 displays the difference matrix $D_3(3)$. When s is a prime number such as 3 or 5, the finite arithmetic used in defining the difference matrix is modulo s arithmetic, and when s is a power of a prime number such as 4 (which is the square of prime number 2), the finite arithmetic is the arithmetic of a Galois Field of s elements. Table 9 defines finite addition for $s = 4$. The finite difference table for $s = 4$ is the same as the finite addition table.

Table 11. Difference matrix $D_3(3)$

Row No.	Column No.		
	1	2	3
1	0	0	0
2	0	1	2
3	0	2	1

2) The *Kronecker sum* of an $M \times M$ difference matrix $D_M(s)$ and a $p \times 1$ vector b of s elements, denoted by $D_M(s) \oplus b$, is a matrix of $M \times p$ rows and M columns obtained by adding in finite arithmetic each element of the vector b to each element of the difference matrix $D_M(s)$. For example, if b is the column vector $(0, 1, 2)$ and $D_3(3)$ is as defined in table 11, then

$$D_M(s) \oplus b = \begin{bmatrix} 0+0 & 0+0 & 0+0 \\ 0+1 & 0+1 & 0+1 \\ 0+2 & 0+2 & 0+2 \\ \\ 0+0 & 1+0 & 2+0 \\ 0+1 & 1+1 & 2+1 \\ 0+2 & 1+2 & 2+2 \\ \\ 0+0 & 2+0 & 1+0 \\ 0+1 & 2+1 & 1+1 \\ 0+2 & 2+2 & 1+2 \end{bmatrix} = \begin{bmatrix} 0 & 0 & 0 \\ 1 & 1 & 1 \\ 2 & 2 & 2 \\ 0 & 1 & 2 \\ 1 & 2 & 0 \\ 2 & 0 & 1 \\ 0 & 2 & 1 \\ 1 & 0 & 2 \\ 2 & 1 & 0 \end{bmatrix}$$

3) An orthogonal array $OA_N(s^m \times t^n)$ is said to be *saturated* when $N - 1 = m(s - 1) + n(t - 1)$. Since an s element column has $s - 1$ degrees of freedom and a t element column has $t - 1$ degrees of freedom, $m + n$ columns of $OA_N(s^m \times t^n)$ have $m(s - 1) + n(t - 1)$ degrees of freedom. Since the N rows of $OA_N(s^m \times t^n)$ yield N (independent) data values, the total number of effects that can be estimated after allowing for the grand mean of the

N data values is $N - 1$. Therefore when a saturated orthogonal array is used as an experimental plan, the total number of effects that can be estimated is equal to the total degrees of freedom of the columns (factors). When all $m + n$ columns are associated with factors, a saturated orthogonal array can be viewed as a saturated main effect fractional factorial plan.

4) An orthogonal array remains an orthogonal array when one of its columns is replaced with an orthogonal array whose rows have a one-to-one correspondence with the elements of the replaced column. For example, suppose a is a four-element column of an orthogonal array A , and suppose B is an orthogonal array whose rows have a one-to-one correspondence with the elements of column a where

$$a = \begin{bmatrix} 0 \\ 1 \\ 2 \\ 3 \\ 3 \\ 2 \\ 1 \\ 0 \end{bmatrix} \quad \text{and} \quad B = \begin{bmatrix} 0 & 0 & 0 \\ 0 & 1 & 1 \\ 1 & 0 & 1 \\ 1 & 1 & 0 \\ 1 & 1 & 0 \\ 1 & 0 & 1 \\ 0 & 1 & 1 \\ 0 & 0 & 0 \end{bmatrix}$$

Then a matrix obtained from the orthogonal array A by replacing the column a with the orthogonal array B is an orthogonal array.

Taguchi's $OA_{18}(2^1 \times 3^7)$, $OA_{32}(2^1 \times 4^9)$, and $OA_{50}(2^1 \times 5^{11})$ are constructed by the Bose and Bush method [6] from the difference matrices $D_6(3)$, $D_8(4)$, and $D_{10}(5)$ displayed in tables 12, 13, and 14 respectively. The following example illustrates the method.

Example: Construction of an $OA_{18}(2^1 \times 3^7)$

- Step 1: Construct a matrix of $6 \times 3 = 18$ rows and 6 columns from the Kronecker sum of the difference matrix $D_6(3)$ displayed in table 12 and the column vector (0,1,2). This 18×6 matrix is displayed in columns 3,4,5,6,7, and 8 of table 3, and it is an $OA_{18}(3^6)$.
- Step 2: Append to columns 3,4,5,6,7, and 8 a six-element column consisting of three 0's, three 1's, three 2's, three 3's, three 4's, and three 5's. Label this column as 1'. Now columns 1',3,4,5,6,7, and 8 of table 3 form a saturated orthogonal array $OA_{18}(6^1 \times 3^6)$.
- Step 3: Construct a matrix of 18 rows and 2 columns by associating the six ordered pairs (0,0), (0,1), (0,2), (1,0), (1,1), and

(1,2) with the 6 elements 0,1,2,3,4, and 5 of column 1'. This matrix is an orthogonal array and its rows have a one-to-one correspondence with the elements of 1'. Write this orthogonal array in columns 1 and 2 of table 3. Now columns 1,2,3,4,5,6,7, and 8 of table 3 form Taguchi's $OA_{18}(2^1 \times 3^7)$.

Taguchi's $OA_{32}(2^1 \times 4^9)$ and $OA_{50}(2^1 \times 5^{11})$ are constructed, similarly, from the difference matrices $D_8(4)$ and $D_{10}(5)$ displayed in Tables 13 and 14, respectively.

Table 12. Taguchi's difference matrix $D_6(3)$

Row No.	Column No.					
	1	2	3	4	5	6
1	0	0	0	0	0	0
2	0	0	1	1	2	2
3	0	1	0	2	1	2
4	0	2	2	1	1	0
5	0	1	2	0	2	1
6	0	2	1	2	0	1

Table 13. Taguchi's difference matrix $D_8(4)$

Row No.	Column No.							
	1	2	3	4	5	6	7	8
1	0	0	0	0	0	0	0	0
2	0	0	1	1	2	2	3	3
3	0	1	2	3	0	1	2	3
4	0	1	3	2	2	3	1	0
5	0	3	0	3	1	2	1	2
6	0	3	1	2	3	0	2	1
7	0	2	2	0	1	3	3	1
8	0	2	3	1	3	1	0	2

Table 14. Taguchi's difference matrix $D_{10}(5)$

Row No.	Column No.									
	1	2	3	4	5	6	7	8	9	10
1	0	0	0	0	0	0	0	0	0	0
2	0	1	2	3	4	0	1	2	3	4
3	0	2	4	1	3	3	0	2	4	1
4	0	3	1	4	2	4	2	0	3	1
5	0	4	3	2	1	3	2	1	0	4
6	0	0	3	4	3	2	1	4	1	2
7	0	1	0	2	2	1	3	4	4	3
8	0	2	2	0	1	4	4	3	1	3
9	0	3	4	3	0	1	4	1	2	2
10	0	4	1	1	4	2	3	3	2	0

The general method of constructing a mixed-element array of the type $OA_N(2^1 \times s^m)$ where $m = 2s + 1$ and $N = 2s^2$ from a difference matrix of the type $D_{2s}(s)$ where s is a prime number (such as 3 or 5) or a power of a prime number (such as 4) consists of three steps.

Step 1: Construct a matrix of $2s^2$ rows and $2s$ columns from the Kronecker sum of the difference matrix $D_{2s}(s)$ and the column vector $(0, 1, \dots, s - 1)$. These $2s$ columns form $OA_N(s^{2s})$ where $N = 2s^2$. Label these columns as $3, 4, \dots$, and $2s + 2$, respectively.

Step 2: Append a $2s$ -element column consisting of s 0's, s 1's, ..., and $s(2s - 1)$'s. (The total number of entries in the column is $2s \times s = 2s^2$). Label this column 1'. Now columns 1', 3, 4, ..., and $2s + 2$ form a saturated orthogonal array $OA_N[(2s)^1 \times s^{2s}]$ where $N = 2s^2$.

Step 3: Construct a matrix of $2s^2$ rows and 2 columns by associating the $2s$ ordered pairs $(0, 0)$, $(0, 1)$, ..., $(0, s - 1)$, $(1, 0)$, $(1, 1)$, ..., and $(1, s - 1)$ with the $2s$ elements $0, 1, \dots, s - 1, s, s + 1, \dots$, and $2s - 1$ of column 1'. This matrix is an orthogonal array and its rows have a one-to-one correspondence with the elements of column 1'. Write this orthogonal array in columns 1 and 2. Now columns 1, 2, 3, ..., $2s + 2$ form $OA_N(2^1 \times s^m)$ where $N = 2s^2$ and $m = 2s + 1$.

A difference matrix remains a difference matrix when (1) its rows are permuted or (2) its columns are permuted or (3) an integer is added (in finite arithmetic) to any column of the matrix. Because of finite arithmetic, the addition of an integer to a column results in a permutation of the elements of that column. Thus each of these three operations results in a permutation of the elements of the matrix. The difference matrices $D_6(3)$ and $D_8(4)$ used by Taguchi are permuted versions of Bose and Bush's $D_6(3)$ and $D_8(4)$, respectively, and Taguchi's $D_{10}(5)$ is a permuted version of Masuyama's [7] $D_{10}(5)$. Specifically, Taguchi's $D_6(3)$ displayed in table 12 can be obtained from Bose and Bush's $D_6(3)$ displayed in table 15 by permuting the columns of table 15 in the following order: 1, 2, 3, 5, 6, and 4. And Taguchi's $D_8(4)$ displayed in table 13 can be obtained from Bose and Bush's $D_8(4)$ displayed in table 16 by permuting the columns of table 16 in the following order:

1, 5, 2, 6, 3, 7, 4, and 8. Similarly, Taguchi's $D_{10}(5)$ displayed in table 14 can be obtained from Masuyama's $D_{10}(5)$ displayed in table 17 by permuting both the rows and the columns of table 17 in the following order: 1, 2, 3, 4, 5, 10, 6, 7, 8, and 9.

Table 15. Bose and Bush's difference matrix $D_6(3)$

Row No.	Column No.					
	1	2	3	4	5	6
1	0	0	0	0	0	0
2	0	0	1	2	1	2
3	0	1	0	2	2	1
4	0	2	2	0	1	1
5	0	1	2	1	0	2
6	0	2	1	1	2	0

Table 16. Bose and Bush's difference matrix $D_8(4)$

Row No.	Column No.							
	1	2	3	4	5	6	7	8
1	0	0	0	0	0	0	0	0
2	0	1	2	3	0	1	2	3
3	0	2	0	2	1	3	1	3
4	0	3	2	1	1	2	3	0
5	0	0	1	1	3	3	2	2
6	0	1	3	2	3	2	0	1
7	0	2	1	3	2	0	3	1
8	0	3	3	0	2	1	1	2

Table 17. Masuyama's difference matrix $D_{10}(5)$

Row No.	Column No.									
	1	2	3	4	5	6	7	8	9	10
1	0	0	0	0	0	0	0	0	0	0
2	0	1	2	3	4	1	2	3	4	0
3	0	2	4	1	3	0	2	4	1	3
4	0	3	1	4	2	2	0	3	1	4
5	0	4	3	2	1	2	1	0	4	3
6	0	1	0	2	2	3	4	4	3	1
7	0	2	2	0	1	4	3	1	3	4
8	0	3	4	3	0	4	1	2	2	1
9	0	4	1	1	4	3	3	2	0	2
10	0	0	3	4	3	1	4	1	2	2

When all $m + 1$ columns are associated with factors, a mixed-element (mixed-level) orthogonal array, $OA_N(2^1 \times s^m)$, where $N = 2s^2$ and $m = 2s + 1$ represents a $N/(2^1 \times s^m) = (1/s)^{m-2}$ fractional factorial plan. For example, $OA_{18}(2^1 \times 3^7)$ can be viewed as a $(1/3)^{7-2} = (1/3)^5$ fraction of a complete $2^1 \times 3^7$ factorial plan.

9. Mixed-Element Orthogonal Arrays
 $OA_{36}(2^{11} \times 3^{12})$ and $OA_{36}(2^3 \times 3^{13})$

These arrays are constructed by appending certain columns to $OA_{36}(3^{12})$ developed by the Bose and Bush method [6] from the difference matrix $D_{12}(3)$ displayed in table 19. The following steps describe the method.

Step 1: Construct a matrix of $12 \times 3 = 36$ rows and 12 columns from the Kronecker sum of the difference matrix $D_{12}(3)$ displayed in table 19 and the column vector (0,1,2). These twelve columns are displayed in columns 12,13,..., and 23 of table 18 and they form $OA_{36}(3^{12})$.

Step 2: Append to columns 12,13,..., and 23 a twelve-element column consisting of three 0's, three 1's,..., and three 11's. Label this column as 1'. Now columns 12,13,..., 22, 23, and 1' form a saturated orthogonal array $OA_{36}(3^{12} \times 12^1)$.

Step 3: Construct a matrix of $12 \times 3 = 36$ rows and 11 columns by repeating three times each row of $OA_{12}(2^{11})$ displayed in table 5. This matrix is an orthogonal array and its rows have a one-to-one correspondence with the twelve elements of column 1'. Write this orthogonal array in columns 1,2,...,10, and 11. Now columns 1,2,...,11,12,13,..., and 23 of table 18 form Taguchi's $OA_{36}(2^{11} \times 3^{12})$.

Table 18. Orthogonal arrays $OA_{36}(2^{11} \times 3^{12})$, $OA_{36}(2^3 \times 3^{13})$, and $OA_{36}(3^{12} \times 12^1)^a$

Row No.	Column No.																												
	1	2	3	4	5	6	7	8	9	10	11	12	13	14	15	16	17	18	19	20	21	22	23	1'	2'	3	4'	1''	
1	0	0	0	0	0	0	0	0	0	0	0	0	0	0	0	0	0	0	0	0	0	0	0	0	0	0	0	0	0
2	0	0	0	0	0	0	0	0	0	0	0	1	1	1	1	1	1	1	1	1	1	1	1	1	0	0	0	0	0
3	0	0	0	0	0	0	0	0	0	0	0	2	2	2	2	2	2	2	2	2	2	2	2	0	0	0	0	0	
4	0	0	0	0	0	1	1	1	1	1	1	0	0	0	0	1	1	1	1	2	2	2	2	0	1	1	0	1	
5	0	0	0	0	0	1	1	1	1	1	1	1	1	1	2	2	2	2	2	0	0	0	0	0	1	1	0	1	
6	0	0	0	0	0	1	1	1	1	1	1	2	2	2	2	0	0	0	0	1	1	1	1	0	1	1	0	1	
7	0	0	1	1	1	0	0	0	1	1	1	0	0	1	2	0	1	2	2	0	1	1	2	1	0	1	0	2	
8	0	0	1	1	1	0	0	0	1	1	1	1	1	2	0	1	2	0	0	1	2	2	0	1	0	1	0	2	
9	0	0	1	1	1	0	0	0	1	1	1	2	2	0	1	2	0	1	1	2	0	0	1	1	0	1	0	2	
10	0	1	0	1	1	0	1	1	0	0	1	0	0	2	1	0	2	1	2	1	0	2	1	1	1	0	0	3	
11	0	1	0	1	1	0	1	1	0	0	1	1	1	0	2	1	0	2	0	2	1	0	2	1	1	0	0	3	
12	0	1	0	1	1	0	1	1	0	0	1	2	2	1	0	2	1	0	1	0	2	1	0	1	1	0	0	3	
13	0	1	1	0	1	1	0	1	0	1	0	0	1	2	0	2	1	0	2	2	1	0	1	0	0	0	1	4	
14	0	1	1	0	1	1	0	1	0	1	0	1	2	0	1	0	2	1	0	0	2	1	2	0	0	0	1	4	
15	0	1	1	0	1	1	0	1	0	1	0	2	0	1	2	1	0	2	1	1	0	2	0	0	0	0	1	4	
16	0	1	1	1	0	1	1	0	1	0	0	0	1	2	1	0	0	2	1	2	2	1	0	0	1	1	1	5	
17	0	1	1	1	0	1	1	0	1	0	0	1	2	0	2	1	1	0	2	0	0	2	1	0	1	1	1	5	
18	0	1	1	1	0	1	1	0	1	0	0	2	0	1	0	2	2	1	0	1	1	0	2	0	1	1	1	5	
19	1	0	1	1	0	0	1	1	0	1	0	0	1	0	2	2	2	0	1	1	0	1	2	1	0	1	1	6	
20	1	0	1	1	0	0	1	1	0	1	0	1	2	1	0	0	0	1	2	2	1	2	0	1	0	1	1	6	
21	1	0	1	1	0	0	1	1	0	1	0	2	0	2	1	1	1	2	0	0	2	0	1	1	0	1	1	6	
22	1	0	1	0	1	1	1	0	0	0	1	0	1	1	2	2	0	1	0	0	2	2	1	1	1	0	1	7	
23	1	0	1	0	1	1	1	0	0	0	1	1	2	2	0	0	1	2	1	1	0	0	2	1	1	0	1	7	
24	1	0	1	0	1	1	1	0	0	0	1	2	0	0	1	1	2	0	2	2	1	1	0	1	1	0	1	7	
25	1	0	0	1	1	1	0	1	1	0	0	0	2	1	0	1	2	2	0	2	0	1	1	0	0	0	2	8	
26	1	0	0	1	1	1	0	1	1	0	0	1	0	2	1	2	0	0	1	0	1	2	2	0	0	0	2	8	
27	1	0	0	1	1	1	0	1	1	0	0	2	1	0	2	0	1	1	2	1	2	0	0	0	0	0	2	8	
28	1	1	1	0	0	0	0	1	1	0	1	0	2	1	1	1	0	0	2	1	2	0	2	0	1	1	2	9	
29	1	1	1	0	0	0	0	1	1	0	1	1	0	2	2	2	1	1	0	2	0	1	0	0	1	1	2	9	
30	1	1	1	0	0	0	0	1	1	0	1	2	1	0	0	0	2	2	1	0	1	2	1	0	1	1	2	9	
31	1	1	0	1	0	1	0	0	0	1	1	0	2	2	2	1	2	1	1	0	1	0	0	1	0	1	2	10	
32	1	1	0	1	0	1	0	0	0	1	1	1	0	0	0	2	0	2	2	1	2	1	1	1	0	1	2	10	
33	1	1	0	1	0	1	0	0	0	1	1	2	1	1	1	0	1	0	0	2	0	2	2	1	0	1	2	10	
34	1	1	0	0	1	0	1	0	1	1	0	0	2	0	1	2	1	2	0	1	1	2	0	1	1	0	2	11	
35	1	1	0	0	1	0	1	0	1	1	0	1	0	1	2	0	2	0	1	2	2	0	1	1	1	0	2	11	
36	1	1	0	0	1	0	1	0	1	1	0	2	1	2	0	1	0	1	2	0	0	1	2	1	1	0	2	11	

^a Columns 1,2,...,22, and 23 form $OA_{36}(2^{11} \times 3^{12})$.
 Columns 1'',12,13,...,22, and 23 form $OA_{36}(3^{12} \times 12^1)$.
 Columns 1',2',3',4',12,13,...,22 and 23 form $OA_{36}(2^3 \times 3^{13})$.

Step 4: Construct a matrix of 12 rows and 4 columns by repeating $OA_4(2^3)$ displayed in table 1 three times and appending a three-element column consisting of four 0's, four 1's and four 2's. These four columns form $OA_{12}(2^3 \times 3^1)$, and are displayed in table 20. Now construct a matrix of 36 rows and 4 columns by repeating three times each of the twelve rows of $OA_{12}(2^3 \times 3^1)$ displayed in table 20. This 36×4 matrix is an orthogonal array of 36 rows and 4 columns and its rows have a one-to-one correspondence with the elements of column 1'. Write this orthogonal array in columns 1', 2', 3', and 4' of table 18. Now columns 12, 13, ..., 23, 1', 2', 3', and 4' of table 18 form Taguchi's $OA_{36}(2^3 \times 3^{13})$.

The difference matrix $D_{12}(3)$ used by Taguchi is a permuted version of Seiden's [8] $D_{12}(3)$. Specifi-

Table 19. Taguchi's difference matrix $D_{12}(3)$

Row No.	Column No.											
	1	2	3	4	5	6	7	8	9	10	11	12
1	0	0	0	0	0	0	0	0	0	0	0	0
2	0	0	0	0	1	1	1	1	2	2	2	2
3	0	0	1	2	0	1	2	2	0	1	1	2
4	0	0	2	1	0	2	1	2	1	0	2	1
5	0	1	2	0	2	1	0	2	2	1	0	1
6	0	1	2	1	0	0	2	1	2	2	1	0
7	0	1	0	2	2	2	0	1	1	0	1	2
8	0	1	1	2	2	0	1	0	0	2	2	1
9	0	2	1	0	1	2	2	0	2	0	1	1
10	0	2	1	1	1	0	0	2	1	2	0	2
11	0	2	2	2	1	2	1	1	0	1	0	0
12	0	2	0	1	2	1	2	0	1	1	2	0

Table 20. Orthogonal array $OA_{12}(2^3 \times 3^1)$

Row No.	Column No.			
	1	2	3	4
1	0	0	0	0
2	0	1	1	0
3	1	0	1	0
4	1	1	0	0
5	0	0	0	1
6	0	1	1	1
7	1	0	1	1
8	1	1	0	1
9	0	0	0	2
10	0	1	1	2
11	1	0	1	2
12	1	1	0	2

cally, Taguchi's $D_{12}(3)$ displayed in table 19 can be obtained from Seiden's $D_{12}(3)$ displayed in table 21 through two operations. First add 1 (in modulo 3 arithmetic) to each element of columns 10 and 11, and add 2 to each element of columns 4, 5, and 8 in table 21, then permute the columns in the following order: 1, 2, 3, 6, 12, 10, 11, 5, 9, 7, 8, and 4.

When all columns of $OA_{36}(2^{11} \times 3^{12})$ are associated with factors, this array represents a $36/(2^{11} \times 3^{12})$ fraction of a complete $2^{11} \times 3^{12}$ factorial plan; a very highly fractionated orthogonal plan indeed. Similarly $OA_{36}(2^3 \times 3^{13})$ represents a $36/(2^3 \times 3^{13})$ fraction of a complete $2^3 \times 3^{13}$ factorial plan.

Table 21. Seiden's difference matrix $D_{12}(3)$

Row No.	Column No.											
	1	2	3	4	5	6	7	8	9	10	11	12
1	0	0	0	1	1	0	0	1	0	2	2	0
2	0	0	0	0	2	0	2	0	2	0	0	1
3	0	0	1	0	0	2	1	2	0	0	1	0
4	0	0	2	2	0	1	0	0	1	1	0	0
5	0	1	2	2	0	0	1	1	2	0	2	2
6	0	1	2	1	2	1	2	2	2	2	1	0
7	0	1	0	0	2	2	0	2	1	1	2	2
8	0	1	1	2	1	2	2	0	0	2	0	2
9	0	2	1	2	1	0	0	2	2	1	1	1
10	0	2	1	0	0	1	2	1	1	2	2	1
11	0	2	2	1	2	2	1	1	0	1	0	1
12	0	2	0	1	1	1	1	0	1	0	1	2

10. Mixed-Element Orthogonal Array $OA_{54}(2^1 \times 3^{25})$

This array is a special case of $OA_{54}(6^1 \times 3^{24})$ where the six-element column is replaced with two columns one having two elements and the other having three elements. Orthogonal array $OA_{54}(6^1 \times 3^{24})$ is displayed in table 22 in a special vector form (to save space). In table 22 boldface numbers and letters **0, 1, 2, 3, 4, 5, a, b**, and **c** represent the column vectors (0,0,0), (1,1,1), (2,2,2), (3,3,3), (4,4,4), (5,5,5), (0,1,2), (1,2,0), and (2,0,1), respectively. An $OA_{54}(6^1 \times 3^{24})$ is constructed from $OA_{18}(6^1 \times 3^6)$, displayed in table 3, in three steps. (1) Repeat three times each row of $OA_{18}(6^1 \times 3^6)$. (2) Append a column consisting of the vector (0,1,2) repeated eighteen times. (3) Append seventeen additional columns representing the interactions of the columns of $OA_{18}(6^1 \times 3^6)$ and the three-element column appended in step 2. The following paragraphs describe these steps in more detail.

Table 22. Orthogonal array $OA_{54}(2^1 \times 3^{25})$, and $OA_{54}(6^1 \times 3^{24})^a$

Row No.	Column No.																												
	1'	1	2	3	4	5	6	7	8	9	10	11	12	13	14	15	16	17	18	19	20	21	22	23	24	25	26		
1-3	0	0	0	0	0	0	0	0	0	a	a	a	a	a	a	a	a	a	a	a	a	a	a	a	a	a	a	a	
4-6	0	0	0	1	1	1	1	1	1	a	a	a	a	a	a	b	c	b	c	b	c	b	c	b	c	b	c	b	c
7-9	0	0	0	2	2	2	2	2	2	a	a	a	a	a	a	c	b	c	b	c	b	c	b	c	b	c	b	c	b
10-12	1	0	1	0	0	1	1	2	2	a	a	b	b	c	c	a	a	a	a	b	c	b	c	c	b	c	b	c	b
13-15	1	0	1	1	1	2	2	0	0	a	a	b	b	c	c	b	c	b	c	c	b	c	b	a	a	a	a	a	a
16-18	1	0	1	2	2	0	0	1	1	a	a	b	b	c	c	c	b	c	b	a	a	a	a	a	b	c	b	c	b
19-21	2	0	2	0	1	0	2	1	2	a	b	a	c	b	c	a	a	b	c	a	a	c	b	b	c	b	c	b	c
22-24	2	0	2	1	2	1	0	2	0	a	b	a	c	b	c	b	c	c	b	a	a	c	b	b	c	a	a	c	b
25-27	2	0	2	2	0	2	1	0	1	a	b	a	c	b	c	c	b	a	a	c	b	b	c	a	a	b	c	a	b
28-30	3	1	0	0	2	2	1	1	0	a	c	c	b	b	a	a	a	c	b	c	b	b	c	b	c	a	a	a	a
31-33	3	1	0	1	0	0	2	2	1	a	c	c	b	b	a	b	c	a	a	a	a	c	b	c	b	b	c	b	c
34-36	3	1	0	2	1	1	0	0	2	a	c	c	b	b	a	c	b	b	c	b	c	a	a	a	a	a	a	c	b
37-39	4	1	1	0	1	2	0	2	1	a	b	c	a	c	b	a	a	b	c	c	b	a	a	c	b	b	c	b	c
40-42	4	1	1	1	2	0	1	0	2	a	b	c	a	c	b	b	c	c	b	a	a	b	c	a	a	b	c	a	b
43-45	4	1	1	2	0	1	2	1	0	a	b	c	a	c	b	c	b	a	a	b	c	c	b	b	c	a	a	a	a
46-48	5	1	2	0	2	1	2	0	1	a	c	b	c	a	b	a	a	c	b	b	c	c	b	a	a	b	c	a	b
49-51	5	1	2	1	0	2	0	1	2	a	c	b	c	a	b	b	c	a	a	c	b	a	a	b	c	c	b	a	b
52-54	5	1	2	2	1	0	1	2	0	a	c	b	c	a	b	c	b	b	c	a	a	b	c	c	b	a	a	a	a

^a Columns 1',3,4,...,25, and 26 form $OA_{54}(6^1 \times 3^{24})$.
Columns 1,2,3,...,25, and 26 form $OA_{54}(2^1 \times 3^{25})$.

The entries 0,1,2,3,4,5,a,b, and c represent the column vectors (0,0,0), (1,1,1), (2,2,2), (3,3,3), (4,4,4), (5,5,5), (0,1,2), (1,2,0), and (2,0,1), respectively.

- Step 1: Construct a 54×7 matrix by repeating three times each row of $OA_{18}(6^1 \times 3^6)$ displayed in table 3. This matrix forms the columns 1',3,4,5,6,7, and 8 of table 22.
- Step 2: Append to columns 1',3,4,5,6,7, and 8 of table 22, a three-element column consisting of the vector (0,1,2) repeated eighteen times. This is column 9 of table 22.
- Step 3: The seventeen columns identified by column numbers 10,11,12,...,25 and 26 of table 22 represent the interactions of column 9 with each of the seven columns 1',3,4,5,6,7, and 8. Since column 1' has 6 elements (5 degrees of freedom) and column 9 has 3 elements (2 degrees of freedom), interaction of column 1' and column 9 has $5 \times 2 = 10$ degrees of freedom. Thus 5 three-element columns (2 degrees of freedom each) are needed to represent the interaction of column 1' and column 9. These five columns are constructed from columns 2,3,4,5, and 6 of the difference matrix $D_6(3)$ displayed in table 12 as follows. Construct an 18×5 matrix (not shown in this paper) by delet-

ing column 1 of table 12 and repeating three times each row of the remaining five columns. Now construct a matrix of 54 rows and 5 columns by the Kronecker sum of this 18×5 matrix and the column vector (0,1,2). These five columns are displayed in columns 10,11,12,13, and 14 of table 22 and they represent the interaction of column 1' and column 9.

Since each of the columns 3,4,5,6,7,8, and 9 has three elements (2 degrees of freedom), each pairwise interaction among these columns has 4 degrees of freedom. Thus 2 three-element columns (2 degrees of freedom each) are needed to represent each pairwise interaction of column 9 with the columns 3,4,5,6,7, and 8. These interaction columns are identified by the method of Bose [2]. This method of construction was used earlier in this paper to construct 2-, 3-, 4-, and 5- element orthogonal arrays. Mark columns 3,4,5,6,7,8, and 9 as $x_3, x_4, x_5, x_6, x_7, x_8$, and x_9 , respectively. These seven columns are used to generate the columns 15,16,17,18,19,20,21,22,23,24,25, and 26 using the following generators, respectively.

Column No.	Generator
15	$x_9 + x_3$
16	$x_9 + 2x_3$
17	$x_9 + x_4$
18	$x_9 + 2x_4$
19	$x_9 + x_5$
20	$x_9 + 2x_5$
21	$x_9 + x_6$
22	$x_9 + 2x_6$
23	$x_9 + x_7$
24	$x_9 + 2x_7$
25	$x_9 + x_8$
26	$x_9 + 2x_8$

All calculations are done in modulo 3 arithmetic. Note that columns 15 and 16 together represent the four degrees of freedom corresponding to the interaction of column 3 and column 9. Similarly the other columns (in pairs) represent the interactions involving column 9, and columns 4,5,6,7, and 8, respectively. Now columns 1',3,4,5,...,25, and 26 of table 22 form $OA_{54}(6^1 \times 3^{24})$.

Taguchi's $OA_{54}(2^1 \times 3^{25})$ is constructed by replacing column 1' with two columns formed by associating the 6 ordered pairs (0, 0), (0, 1), (0, 2), (1, 0), (1, 1), and (1, 2) with the elements 0,1,2,3,4, and 5 of column 1'. These two columns are displayed in columns 1 and 2 of table 22. Now columns 1,2,3,4,..., 25 and 26 of table 22 form Taguchi's $OA_{54}(2^1 \times 3^{25})$. When all columns of $OA_{54}(2^1 \times 3^{25})$ are associated with factors, this array represents a $54/(2^1 \times 3^{25})$ fraction of a complete $2^1 \times 3^{25}$ factorial plan.

11. Concluding Remarks

As shown in this paper, Taguchi's catalog of orthogonal arrays [1] is primarily based on two papers: Bose [2], and Bose and Bush [6]. The Bose paper laid the mathematical foundation of fractional factorials and orthogonal arrays. The Bose and Bush paper describes a method of constructing mixed-element orthogonal arrays from difference matrices. The difference matrices used by Taguchi to construct $OA_{18}(2^1 \times 3^7)$, $OA_{32}(2^1 \times 4^9)$, $OA_{36}(2^{11} \times 3^{12})$, $OA_{36}(2^3 \times 3^{13})$ and $OA_{50}(2^1 \times 5^{11})$ are permuted versions of the difference matrices developed by Bose and Bush [6], Seiden [8], and Masuyama [7]. The extensions of the Bose, and the Bose and Bush, methods needed to construct $OA_{36}(2^{11} \times 3^{12})$, $OA_{36}(2^3 \times 3^{13})$, and $OA_{54}(2^1 \times 3^{25})$ appear to be Taguchi's contributions. The authors have shown that Taguchi's $OA_{12}(2^{11})$ is a permuted

version of the Plackett and Burman [5] plan of 12 runs, but there is no reason to believe that Taguchi permuted the Plackett and Burman plan to construct his $OA_{12}(2^{11})$.

Although the original Japanese version of Taguchi's catalog of orthogonal arrays was developed before 1960, it continues to be very useful. These arrays can be modified to generate many types of multifactor experiments [9] and many other orthogonal arrays can be derived from Taguchi's catalog through established mathematical procedures. Nevertheless, the catalog can now be expanded to include arrays developed after 1960. For example, Taguchi's catalog can be expanded to include $OA_{24}(4^1 \times 2^{20})$, $OA_{40}(4^1 \times 2^{36})$ and $OA_{48}(4^3 \times 2^{38})$ first developed by Dey and Ramakrishna [10] and Chacko, Dey, and Ramakrishna [11], and then re-constructed through a unified procedure by Cheng [12]. It is the authors' intent to develop an expanded and revised version of Taguchi's catalog of orthogonal arrays. A companion paper [13] limited to the fixed-element orthogonal arrays appeared in the Journal of Quality Technology.

About the authors: Raghu N. Kacker, Eric S. Lagergren, and James J. Filliben, are Mathematical Statisticians in the Statistical Engineering Division of the National Institute of Standards and Technology, Computing and Applied Mathematics Laboratory, located at Gaithersburg, Maryland.

12. References

- [1] G. Taguchi, Orthogonal Arrays and Linear Graphs, American Supplier Institute, Inc., Dearborn, MI (1986).
- [2] R. C. Bose, Mathematical Theory of the Symmetrical Factorial Designs, Sankhya 8, 107-166 (1947).
- [3] F. Yates, The Design and Analysis of Factorial Experiments, Imperial Bureau of Soil Science Technology Communication Number 35, (1937).
- [4] G. E. P. Box, W. G. Hunter, and J. S. Hunter, Statistics for Experimenters, John Wiley and Sons, Inc., New York, NY (1978).
- [5] R. L. Plackett, and J. P. Burman, The Design of Optimum Multifactorial Experiments, Biometrika 33, 305-325 (1945).
- [6] R. C. Bose, and K. A. Bush, Orthogonal Arrays of Strength Two and Three, Annals of Mathematical Statistics 23, 508-524 (1952).
- [7] M. Masuyama, On Difference Sets for Constructing Orthogonal Arrays of Index Two and of Strength Two, Report on Statistical Applications and Research, JUSE 5, 27-34 (1957).
- [8] E. Seiden, On the Problem of Construction of Orthogonal Arrays, Annals of Mathematical Statistics 25, 151-156 (1954).

- [9] G. Taguchi, *System of Experimental Design*, Vols. 1 and 2, UNIPUB/Kraus International Publications, White Plains, NY (1987).
- [10] A. Dey, and G. V. S. Ramakrishna, A Note on Orthogonal Main Effect Plans, *Technometrics* **19**, 511-512 (1977).
- [11] A. Chacko, A. Dey, and G. V. S. Ramakrishna, Orthogonal Main Effect Plans for Asymmetrical Factorials, *Technometrics* **21**, 269-270 (1979).
- [12] C. S. Cheng, Some Orthogonal Main-Effect Plans for Asymmetrical Factorials, *Technometrics* **31**, 475-477 (1989).
- [13] R. N. Kacker, E. S. Lagergren, and J. J. Filliben, Taguchi's Fixed-Element Arrays are Fractional Factorials, *J. Quality Technol.* **23**, 107-116 (1991).

A Mathematical Model for Dental Caries: A Coupled Dissolution-Diffusion Process

Volume 96

Number 5

September-October 1991

T. M. Gregory,
L. C. Chow, and
C. M. Carey

American Dental Association
Health Foundation,
Paffenbarger Research Center,
National Institute of Standards
and Technology,
Gaithersburg, MD 20899

Demineralization of tooth mineral in the caries process was studied using a computer model that simulates a diffusion controlled dissolution process. The model consists of a two-compartment system. An acidic solution in the outer ("plaque") compartment was assumed to be large in volume so that its composition remained constant during the process. The solution in the inner ("lesion") compartment was in equilibrium with the tooth mineral, but its composition changed in response to diffusion of ions between the two solutions through an infinitely thin barrier. The permselectivity of the diffusion barrier to cations and anions can be modified as desired thus allowing the effects of membrane on the diffusion-dissolution process to be examined. Because the losses of calcium (Ca) and phosphate (P) from the "lesion" to the "plaque" generally does not occur at a molar ratio of 5/3, the Ca to P ratio of the dis-

solving mineral, the composition of the "lesion" fluid can change significantly from the starting composition, and this in turn modifies the Ca and P fluxes. A steady state condition is eventually reached under which the ratio of flux of Ca to that of P becomes 5/3. The results of the simulation show that for a given "plaque" pH, the rate of demineralization at steady state was the highest for cation and the lowest for anion permselective membranes. These results were in good agreement with those from an experimental study under comparable conditions.

Key words: Ca flux; computer simulation; coupled dissolution-diffusion; dental caries; hydroxyapatite; P flux; permselective diffusion.

Accepted: August 1, 1991

1. Introduction

In the early stages of tooth decay, the affected tooth enamel usually is in the form of a subsurface lesion, Fig. 1. The outstanding features of a lesion are: (1) the "intact layer," a layer of relatively sound enamel at the tooth surface, (2) the "body of the lesion" consisting of partially demineralized enamel, and (3) the "advancing front" where active demineralization occurs. The subsurface demineralization of tooth in the caries process requires diffusion of acid ions into, and of solubilized mineral ions out of the lesion. Even when highly simplified, it is a relatively complex physicochemical process.

Results from recent studies have shown that during the demineralization process, the solution within the lesion is approximately saturated with respect to the tooth mineral at all times [1,2]. These results indicate that the rate of dissolution of tooth mineral in the lesion is faster than the rate of transport of the mineral ions out of the lesion. Thus, the process of subsurface demineralization is diffusion controlled, and the rate of lesion progression may be expected to be strongly dependent on factors that govern the diffusion process.

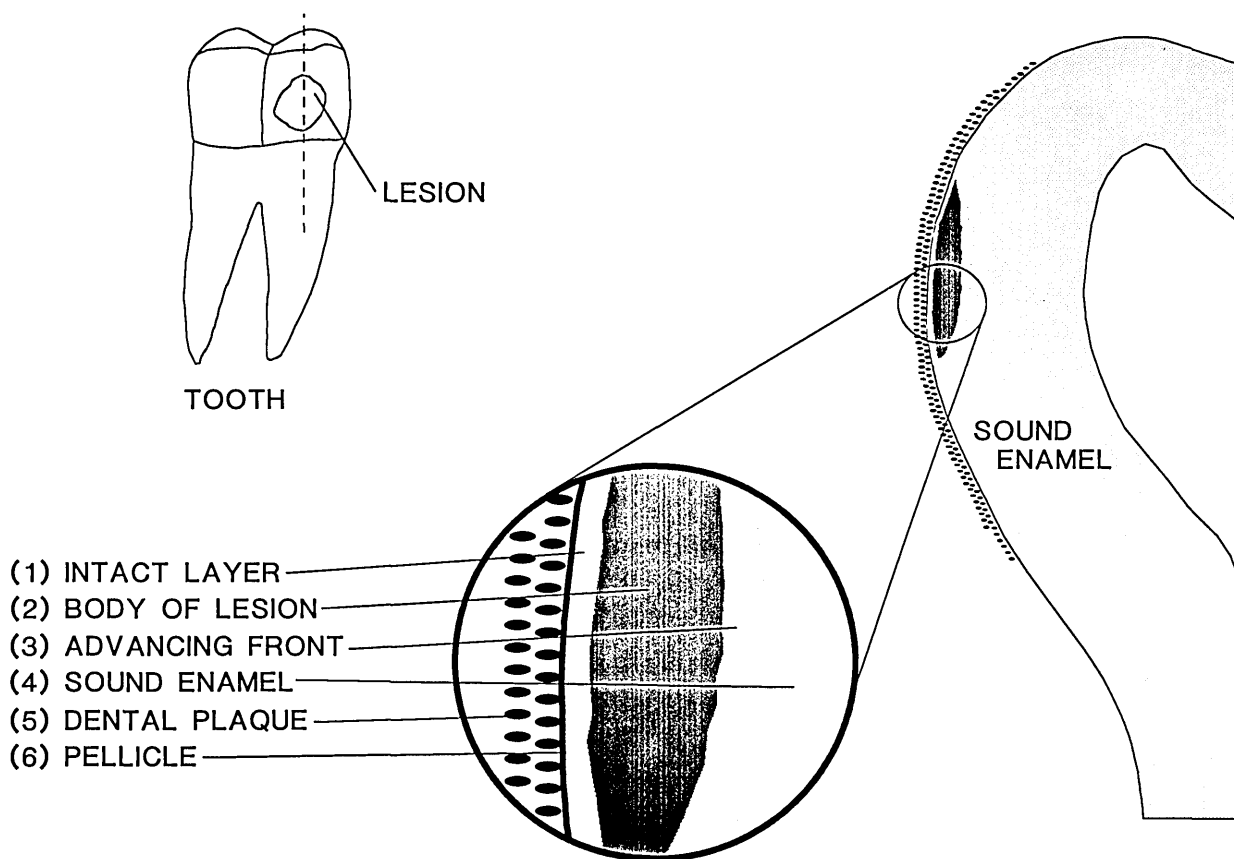


Figure 1. A schematic drawing of a typical dental caries lesion showing (1) an intact layer at the surface, (2) body of the lesion consisting of partially demineralized enamel, (3) the "advancing front" where active demineralization occurs, (4) sound enamel, (5) dental plaque covering the tooth, and (6) pellicle, adsorbed proteinaceous material on the tooth surface.

Several mathematical models have been proposed to describe the diffusion process during lesion formation [3–7]. In the present study the caries process was also assumed to be controlled by the diffusion of ions, but it takes into consideration a most important phenomenon which has not been addressed in previous studies: the interaction between the permselective diffusion of ions and the dissolution of tooth mineral as described below.

The dissolution of tooth mineral at the advancing front (Fig. 1) adds calcium (Ca) and phosphate (P) ions to the solution within the lesion at a molar ratio of 5/3, the Ca/P ratio of the solid. On the other hand, the relative rates of the loss of Ca and P from the lesion to the plaque generally is not at a ratio of 5/3. This is because diffusion of the various Ca and P containing ions (Table 1) is largely controlled by factors such as the electrochemical potential gradients and the permselectivity of the diffusion barrier, which may consist of the body of the lesion, the intact layer, and the pellicle, etc. [8]. The unequal rates of addition and removal of Ca or

P by the dissolution and diffusion processes, respectively, would lead to a change in the composition of the lesion fluid. This in turn modifies the driving forces for diffusion of all the ions. Thus, subsurface demineralization may be described as a coupled dissolution-diffusion process in which the composition of the saturated solution in the lesion changes in response to the diffusion of ions until a steady state is reached.

In previous studies [9–11] a diffusion cell comprising two compartments separated by an artificial membrane of known ion permselectivity was used as an experimental model to explore factors that may affect caries formation. One compartment (the "lesion") contained an excess of hydroxyapatite (OHAp), $\text{Ca}_5(\text{PO}_4)_3\text{OH}$, crystals, and its solution was kept at or near saturation by stirring. An undersaturated acidic calcium phosphate solution flowed continuously through the other compartment (the "plaque"), thus providing the driving force for dissolution of the crystals as modified by the permselectivity of the membrane. As described

above, when the steady state is reached the composition of the "lesion" solution will become constant and the ratio of the flux of Ca to P will be 5/3. The results from the bench-scale caries model studies demonstrated that the composition of the saturated solution in the "lesion" can undergo great changes prior to attainment of steady state [9,10]. Furthermore, the large changes in the concentrations of the various ions in the "lesion" fluid, as affected by the permselectivity of the diffusion barrier, significantly increased or decreased the rate of mineral loss at steady state [11]. In the present paper we describe a mathematical model that simulates this bench-scale caries model so that the dynamics of diffusion-dissolution interactions may be more fully understood. The model also makes it possible to more rapidly survey the effects of a number of different variables on demineralization.

Table 1. Diffusing species and diffusion coefficients at 25 °C

Species	$D^0 \times 10^5$ cm ² /s	Species	$D^0 \times 10^5$ cm ² /s
H ⁺	9.3 ^a	OH ⁻	5.28 ^a
K ⁺	1.96 ^a	Cl ⁻	2.03 ^a
Ca ²⁺	0.79 ^a	H ₂ PO ₄ ⁻	0.88 ^b
CaH ₂ PO ₄ ⁺	0.62 ^c	CaPO ₄ ⁻	0.29 ^c
CaOH ⁺	1.03 ^a	HPO ₄ ²⁻	0.44 ^b
H ₃ PO ₄	1.61 ^b	PO ₄ ³⁻	0.61 ^b
CaHPO ₄	0.28 ^c		

^a D_s^0 calculated from values given in [12].

^b D_s^0 calculated from values given in [13].

^c D_s^0 calculated from values given in [12] and [13].

2. Methods

2.1 Overview

In this computer simulation of the caries-forming process, the transport of all solution species (Table 1) is tracked between a "plaque" compartment and a "lesion" compartment, separated by a barrier which blocks the free flow of fluids and is selectively permeable to all solution species. The "plaque" compartment is treated as a large reservoir of invariant composition with a fixed degree of under-saturation with respect to the dissolving mineral, OHAp. This composition can be selected to simulate various oral environments. The "lesion" compartment is visualized as a suspension of OHAp crystals maintained at or near saturation by dissolution or precipitation which is assumed to be more rapid than the diffusion process.

The computations proceed to convergence through a number of cycles, each consisting of two

phases or loops. In the first phase ("diffusion loop"), diffusion across the barrier for a specified small time interval results in concentration changes in the "lesion" compartment. In the second phase ("dissolution loop"), saturation of the "lesion" solution is re-established. When the system has converged to a steady state, the composition of the "lesion" compartment becomes invariant with time, and concomitantly the molar ratio of the total flux of calcium $J(\text{Ca})_T$ to the total flux of phosphate $J(\text{P})_T$ attains the value 5/3, the Ca/P of the dissolving solid.

The model approximates continuous diffusion across an infinitely thin barrier separating the "lesion" from the "plaque." Under this restriction the diffusion potential (ΔE) and the fluxes (J_s) of the individual solution species are approximated [14] by the following equations:

$$\Delta E = -(RT/F) \sum_s (t_s/z_s) \ln(a_s^L/a_s^P) \quad (1)$$

and

$$J_s = -D_s C_s [\ln(a_s^L/a_s^P) + z_s(F/RT)\Delta E] \quad (2)$$

where

T = Temperature (K)

R = The gas constant (8.314×10^7 J · mol⁻¹ · K⁻¹)

F = Faraday constant (9.649×10^{11} J · V⁻¹ · mol⁻¹)

and for the s th species, with the compartment designated by superscript,

t_s = transference number

z_s = valence

D_s = diffusion coefficient within the barrier (cm²/s)

$C_s = (C_s^L + C_s^P)/2$ (mol/L); the average concentration across the membrane

a_s = thermodynamic activity (mol/L).

It may be observed that the flux, J_s , of any charged species is influenced by both chemical and electrical (membrane) potentials as indicated by the two terms in Eq. (2).

2.2 Characterization of the Barrier

For the barrier to exhibit the permselectivity of tooth enamel to individual ions, the diffusion constants, D_s^0 , can be modified by arbitrary scaling factors. For example, to simulate an anion perm-

selective membrane, the diffusion constants of all cations may be reduced by a common scale factor, f , using the equation,

$$D_s = f |z_s| \cdot D_s^0 \quad (3)$$

where D_s^0 is the diffusion coefficient of species s in water (Table 1). D_s^0 for the ions was calculated from the ionic mobility (μ_s) using the Nernst-Einstein relation [$D_s^0 = (RT/F)\mu_s$] and for ion pairs, the Nernst method for the average diffusion coefficient [12]. Values of f of 1.0 (nonselective membrane) or 0.01 for either cations (anion permselective membrane) or anions (cation permselective membranes) were used in this study. The diffusion coefficients for H^+ and OH^- were allowed to be invariant to account for the Grotthuss mechanism of H^+ and OH^- association with the solvent (H_2O) across the membrane [12].

2.2.1 Input and Initial conditions

1. All constants in the preceding list from R (gas constant) to D_s^0 (diffusion coefficients) were stored as functions of temperature in the program. Also stored were dissociation and association constants of all partially dissociated species such as weak acids, ion pairs, etc.
2. The temperature, T , was input for each run and was the same for both the "lesion" and "plaque" compartments.
3. For the "plaque" compartment, the composition of the solution was chosen to represent a fixed degree of undersaturation with respect to tooth mineral, OHAp, at the given temperature. This solution retained these initial concentrations.

Table 2 lists the compositions of five "plaque-saliva" compositions that had been used in the previous experimental study and

were used in the present simulation study. The solutions all contained 1 mmol/L HCl, 30 mmol/L KCl, with various amounts OHAp dissolved such that the pH of the solution ranged from 3.2 to 5.0 and $pLAP_{OHAp}$ (LAP = ion activity product) ranged from 82.55 to 65.1.

4. For the initial solution in the "lesion" compartment, the composition was chosen to be the "plaque" solution that was made saturated with respect to OHAp (Table 2). This solution can be represented as a point on the $pU(-)$ isotherm, e.g., point A, in the phase diagram shown in Fig. 2. The generalized fourth component [$U(\pm)$] in the system is defined in Appendix A.
5. Compositions of solutions in both compartments were initially adjusted to assure electroneutrality by an iteration procedure that finds the appropriate $[H^+]$ value (see Sec. 2.2.2,1 below).

2.2.2 Diffusion Loop of Calculation Objective: Compute state of the system in the "lesion" after an interval of mass flow.

1. Concentrations and activities of all species C_s (except $[H^+]$) listed in Table 1 were calculated by an iterative process [15,16] using known equilibrium constants and a suitable approximation (Debye-Hückel) for the activity coefficients [15]. All constants were determined at the temperature of interest and are given in Table 3 for 25 °C. The computations were done just once for the "plaque" compartment because this compartment is held at fixed concentrations.
2. Next the diffusion potential, ΔE , was calculated according to Eq. (1); ΔE is a linear function of the terms consisting of logarithmic ratios of the

Table 2. Composition and $pLAP_{OHAp}$ of the "plaque" and initial lesion solutions

	pH	Tot Ca mmol/L	Tot PO ₄ mmol/L	K mmol/L	Cl mmol/L	$pLAP_{OHAp}$ ^a
Plaque solutions						
A	3.194	0.741	0.444	30.0	31.0	82.55
B	3.503	0.185	0.111	30.0	31.0	77.17
C	4.003	0.630	0.378	30.0	31.0	72.48
D	4.503	0.689	0.413	30.0	31.0	68.66
E	4.998	0.709	0.425	30.0	31.0	65.10
Initial lesion solution						
	5.929	0.741	0.444	30.0	31.0	58.55

^a $pLAP_{OHAp}$ values calculated at 25 °C, appropriate constants given in Table 3.

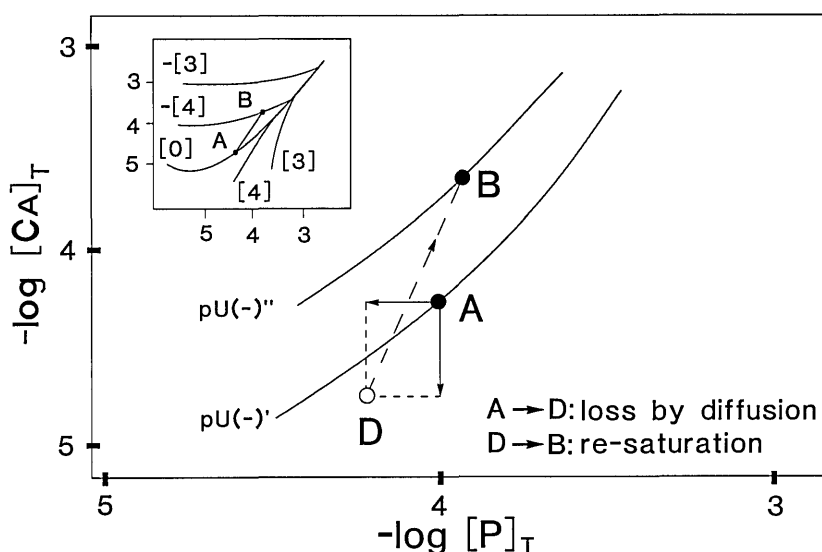


Figure 2. A schematic representation of the changes in the composition of the "lesion" solution, expressed in a $-\log[P]_T$ vs $-\log[Ca]_T$ phase diagram, during a computation cycle. See Appendix for the definition of U.

Table 3. Constants at 25 °C

Equilibrium constant (K)		
Reaction	K	Ref.
K_{P1} : $H_3PO_4 \rightleftharpoons H^+ + H_2PO_4^-$	7.11×10^{-3}	[17]
K_{P2} : $H_2PO_4^- \rightleftharpoons H^+ + HPO_4^{2-}$	6.31×10^{-8}	[18]
K_{P3} : $HPO_4^{2-} \rightleftharpoons H^+ + PO_4^{3-}$	4.52×10^{-13}	[19]
K_w : $H_2O \rightleftharpoons H^+ + OH^-$	1.01×10^{-14}	[20]
Debye (A)	0.5115	[21]
Association constant (K_a)		
Ion pairs	K	Ref.
$K_{CaH_2PO_4^+}$: $Ca^{2+} + H_2PO_4^- \rightleftharpoons CaH_2PO_4^+$	8.45	[22]
$K_{CaHPO_4^0}$: $Ca^{2+} + HPO_4^{2-} \rightleftharpoons CaHPO_4^0$	265.0	[22]
$K_{CaPO_4^-}$: $Ca^{2+} + PO_4^{3-} \rightleftharpoons CaPO_4^-$	2.90×10^7	[23]
K_{CaOH^+} : $Ca^{2+} + OH^- \rightleftharpoons CaOH^+$	20.0	[24]
Solubility product (KSP)		
Ca- PO_4 salt	K	Ref.
KSP_{OHAP} : $Ca_5(PO_4)_3OH$	2.79×10^{-59}	[25]
KSP_{OCP} : $Ca_8H_2(PO_4)_6 \cdot 5H_2O$	3.71×10^{-49}	[26]
KSP_{DCPD} : $CaHPO_4 \cdot 2H_2O$	2.51×10^{-7}	[22]
KSP_{BTCP} : $Ca_3(PO_4)_2$	1.22×10^{-29}	[27]
KSP_{ACP} : $Ca_3(PO_4)_2$	5.89×10^{-26}	[28]

activities in the two compartments, $\ln(a_s^L/a_s^R)$, and the transference numbers as shown in Eq. 1.

- Calculation of mass flows was conducted as follows.

- The fluxes, J_s , were computed using the modified Nernst-Planck flux equation [Eq. 2]; the approximations used in deriving this equation as well as Eq. (1) for the diffusion potential require that all the quantities remain constant over a certain small time interval, Δt . It was thus necessary to limit the magnitude of concentration changes by adjusting the size of Δt .
- The material flows are $\Delta C_s = J_s \Delta t$, and the resulting new concentrations are $C_s' = C_s + \Delta C_s$. These two quantities were used in the following constraints to assure that the changes in the state of the system were so small that the assumption in 3a holds.
 - $|\Delta C_s|/C_s$ must lie between predetermined limits.
 - For the new system composition, $|\Delta E_{new} - \Delta E_{old}|$ must not exceed a predetermined limit.

If either (i) or (ii) was not satisfied, a new smaller Δt was chosen and ΔC_s , etc., were recalculated.
- Using the new ion concentrations, C_s' , new total concentrations of the various components resulting from the mass flow were calculated. The value of $[Ca]_T$ for the calcium component is the sum of all calcium-containing species and similarly for P, K, Cl and other components. The

system will now be at a point "D" in the phase diagram (Fig. 2), representing a condition of undersaturation.

- d. The total flux for each component was calculated for later use to check steady state condition. In particular, for the Ca and P components:

$$J(\text{Ca})_T = J(\text{Ca}^{2+}) + J(\text{CaH}_2\text{PO}_4^+) + \dots$$

$$J(\text{P})_T = J(\text{H}_3\text{PO}_4) + \dots + J(\text{CaH}_2\text{PO}_4^+) + \dots$$

where $J(\text{Ca})_T$ and $J(\text{P})_T$ are the sums of the flux for all species containing Ca and P, respectively.

2.2.3 Dissolution Loop of Calculation The next stage of the calculation was to re-establish saturation in the "lesion" compartment. This feature is a crucial part of the model that has not been implemented successfully in previous literature reports.

Objective: Drive the solution in the "lesion" from the undersaturated state (point D, Fig. 2) reached at (Sec. 2.2.2,3c) to a new equilibrium (saturated) condition. The position in the new composition will then be at point B, lying on an isotherm $pU(-)'$ (Fig. 2).

Method: With the total phosphate concentration, $[\text{P}]_T$, and $[\text{H}^+]$ as variables, a nonlinear least squares procedure [29,30] was used to satisfy the conditions of electroneutrality and saturation (Eqs. (4) and (5)), forcing congruent dissolution/precipitation, i.e., $\Delta[\text{Ca}]_T = (5/3)\Delta[\text{P}]_T$.

$$\sum_i z_i C_i = E \rightarrow 0 \quad (4)$$

$$pIAP_{\text{OHAp}} - pKSP_{\text{OHAp}} = S \rightarrow 0 \quad (5)$$

where IAP_{OHAp} is the ionic activity product and KSP_{OHAp} is the solubility product for OHAp (Table 3).

The least squares procedure utilizes an iterative process to achieve convergence to a minimum where the sum of $E^2 + S^2$ approaches zero. The resulting composition is represented by a new point, B, on an isotherm $pU(-)'$ (Fig. 2). The isotherm $pU(-)'$ is different from the isotherm $pU(-)$ in the previous cycle because of the change in the value of "electroneutrality unbalance" [8]. This is caused by the diffusion of non-consumed anions (e.g., Cl^-) and cations (e.g., K^+) [10] that occurred during the time interval Δt . The composition at point B was then compared to the composition at the commencement of the preceding mass flow stage (Point "A" in the diagram). If B differed from A, the steady state had not been reached and the system returned to step 2 in Sec.

2.2.2 until convergence, i.e., the steady state was attained.

2.2.4 Steady State At steady state the difference between points "A" and "B" in Fig. 2 becomes negligible. This implies that mass changes due to diffusion are exactly compensated by mass changes due to dissolution/precipitation reactions. Under these conditions $J(\text{Ca})_T/J(\text{P})_T = 5/3$. The total fluxes were calculated at step 3d in Sec. 2.2.2 and the ratio was monitored throughout successive iterations.

3. Results

The composition of the "lesion" solution and the fluxes of the various components were found to change significantly from the starting point to the steady state. The rates of demineralization, expressed in the units $\mu\text{g OHAp}/\text{cm}^2 \text{min}$, calculated from the steady state $(\text{Ca})_T$ or the $(\text{P})_T$ flux at various "plaque" pH values are given in Table 4. It can be seen that for a given type of membrane the rate of demineralization increased as the "plaque" pH decreased. For a given "plaque" pH the rate of demineralization is the highest with the cation permselective membrane and is the lowest with the anion permselective membrane. Although the effects of membrane permselectivity on rate of demineralization were similar in trend at the various "plaque" pH values, the effects became progressively greater as the "plaque" pH was decreased. For example, at pH 5.0 the relative rates of demineralization for the three membranes were nonselective: cation: anion = 100: 241: 1.5, whereas at pH 3.2 the relative rates were 100: 258: 0.064. For comparison purposes the experimental values of Chow and Brown [11] are also given. It can be seen that the effects of pH and membrane permselectivity on the demineralization rate are similar between the computer simulation and the bench-scale experiments. The simulation and the experimental flux values were found to be strongly correlated with the correlation coefficients being equal to 0.995, 0.996, and 0.999 for the nonselective, cationic permselective, and anionic permselective membrane systems, respectively. As shown in Table 4, the average ratios of the simulation and experimental flux values for the three groups are 29.0, 43.0, and 1.3, respectively. The ratio, 29.0, for the nonselective membrane system may be taken as a proportionality constant needed to account for the inherent differences in the two models. The higher ratio, 43.0, for the cationic permselective membrane system and the lower ratio, 1.3, for the

anionic permselective system suggest that the simulation model magnified the effects of the membrane, probably due to the high degree of permselectivity assigned to the membranes (0.01). The effects of membrane permselectivity on the rate of demineralization shown in Table 4 are in fact a result of the significant changes in the composition of the "lesion" solution that occurred from

Table 4. Rate of demineralization obtained from the experimental bench-scale model and the computer simulation of caries

Membrane	Rate of demineralization of OHAp ($\mu\text{g OHAp}/\text{cm}^2 \text{min}$)					
	"Plaque" pH					
	3.2	3.5	4.0	4.5	5.0	
<i>Non-selective</i>						
Simulation ^a	265.3	105.1	28.11	7.54	2.66	
Experimental ^b	10.4	3.08	0.88	0.28	0.10	
Ratio ^c	25.5	34.1	31.9	26.9	26.6	avg = 29.0
<i>Cationic</i>						
Simulation	683.7	294.7	79.64	22.48	6.42	
Experimental	15.7	8.08	2.31	0.62	0.10	
Ratio	43.5	36.5	34.5	36.3	64.2	avg = 43.0
<i>Anionic</i>						
Simulation	0.17	0.14	0.09	0.06	0.04	
Experimental	0.19	0.14	0.07	0.03	0.00	
Ratio	0.89	1.00	1.29	2.00		avg = 1.30

^a Calculated from the flux of calcium or phosphate from the computer simulation.

^b Experimental bench-scale data from [11].

^c Ratio of the simulation and experimental flux values.

the beginning of the process to the time when steady state was reached. For the purpose of illustrating the dynamic nature of the diffusion-dissolution interactions, results from the simulations with a "plaque" pH of 4.5 are described in greater detail below.

Figure 3a shows the $[\text{Ca}]_T$, $[\text{P}]_T$, $[\text{K}]_T$, $[\text{Cl}]_T$, and the pH of the "lesion" solution as a function of time for the system with the nonselective membrane. The fluxes of these components and the membrane potential during the same time period are shown in Fig. 3b. It is noted that although a total of seven phosphate-containing species (Table 1) were considered in the calculations, in the pH range used, H_2PO_4^- is the predominant phosphate species and its diffusion accounts for the bulk of the P flux. Similarly, the diffusion of the free Ca^{2+} , K^+ , and Cl^- ions accounts for nearly all of the Ca, K and Cl fluxes, respectively. Consequently, the changes in the total concentrations and total fluxes shown in Figs. 3a and 3b can be adequately understood by examining the diffusion of the corresponding predominant ions. At the beginning of the process, driving forces existed for the inward diffusion of H^+ ions and outward diffusion of Ca^{2+} and H_2PO_4^- ions. The diffusion of these ions produced a slight negative membrane potential (-0.07 mV), which induced a short burst of K^+ and Cl^- diffusion in opposite directions (Fig. 3b) even though no concentration gradient existed for either ion initially. The K^+ and Cl^- diffusion ceased as the concentrations of these ions in the

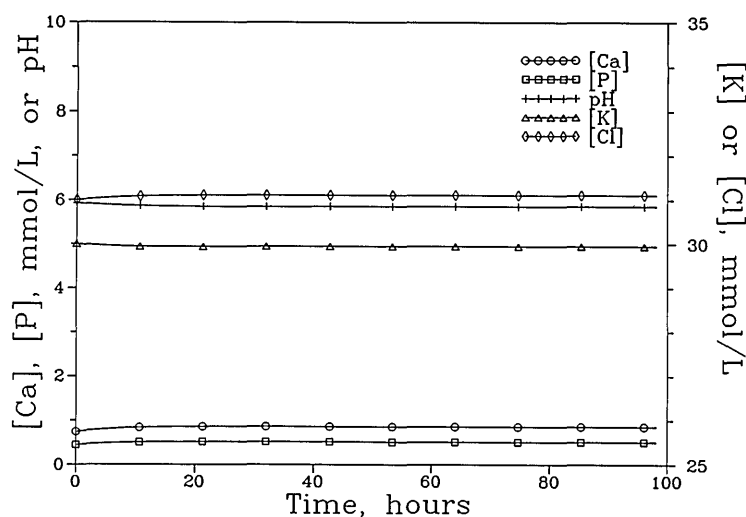


Figure 3a. The $[\text{Ca}]_T$, $[\text{P}]_T$, $[\text{K}]_T$, and $[\text{Cl}]_T$ of the "lesion" solution as a function of time for the system with the nonpermselective membrane and a "plaque" pH of 4.5.

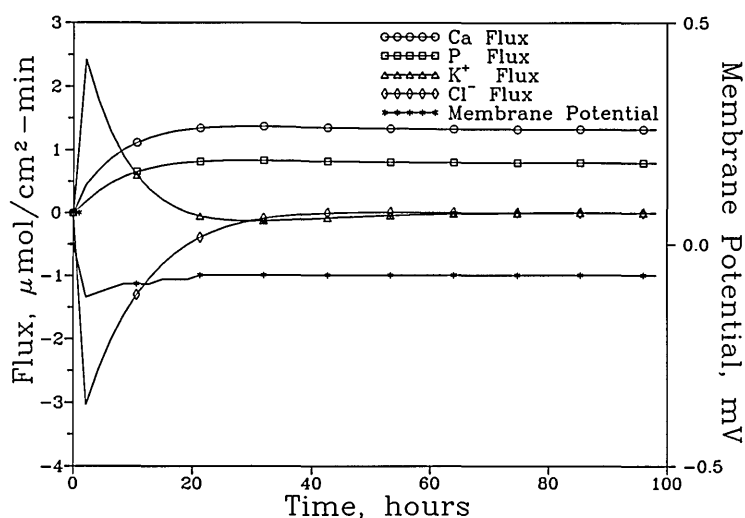


Figure 3b. The fluxes of these components and the membrane potential over the same time period.

“lesion” solution approached those prescribed by the membrane potential following the Nernst Equation [14]. In approaching the steady state, the $[Ca]_T$ and $[P]_T$ increased slightly, from 0.741 and 0.444 mmol/L to 0.855 and 0.513 mmol/L, respectively, and the pH decreased slightly, from 5.929 to 5.855. The $[K]_T$ decreased slightly, from 30.00 to 29.95 mmol/L, and the $[Cl]_T$ increased slightly from 31.00 to 31.11 mmol/L. The $(Ca)_T$ and $(P)_T$ fluxes increased steadily to 1.324 and 0.795 mmol/cm² sec, respectively, when the steady state was reached.

Figure 4a shows the $[Ca]_T$, $[P]_T$, $[K]_T$, $[Cl]_T$, and the pH of the “lesion” solution as a function of time for the system with the cation permselective membrane. The fluxes of these components and the membrane potential during the same time period are shown in Fig. 4b. It is seen from Fig. 4b that the cation permselective nature of the diffusion barrier allowed Ca^{2+} ions to diffuse out of the “lesion” rapidly during the early period, i.e., the first 20 h of the process. Although the flux of H^+ was not followed in the calculations, the presence of a negative membrane potential at this time period would indicate that the inward diffusion of H^+ was in fact more rapid than the outward diffusion of Ca^{2+} . The negative membrane potential brought

about a burst of outward diffusion of K^+ , an ion which did not have a concentration gradient at the start. The membrane potential reached a minimum of -0.9 mV at approximately 50 h and started to increase steadily in approaching the steady state. The change in the sign of the membrane potential can be attributed to a decreased inward diffusion of H^+ because the “lesion” pH has been reduced from 5.93 to 5.45, diminishing the driving force for proton diffusion. The change in the sign of the membrane potential led to a corresponding change in the direction of K^+ diffusion. After the rearrangement of dominant driving forces in the initial stage of the process (the first 200 h), the fluxes and concentrations of all ions approached the steady state values asymptotically. When the steady state was reached, the $[Ca]_T$ increased significantly from 0.741 to 1.417 mmol/L, the $[P]_T$ increased substantially from 0.444 to 9.576 mmol/L, the $[K]_T$ increased from 30.00 to 34.61 mmol/L, and the $[Cl]_T$ decreased from 31.00 to 27.70 mmol/L. It is interesting to note that at steady state the $[Ca]_T/[P]_T$ ratio was 0.148, which is drastically reduced from the initial value of 1.67. The $(Ca)_T$ and $(P)_T$ fluxes at steady state were 3.719 and 2.164, nearly triple the corresponding fluxes in the system with the nonselective membrane.

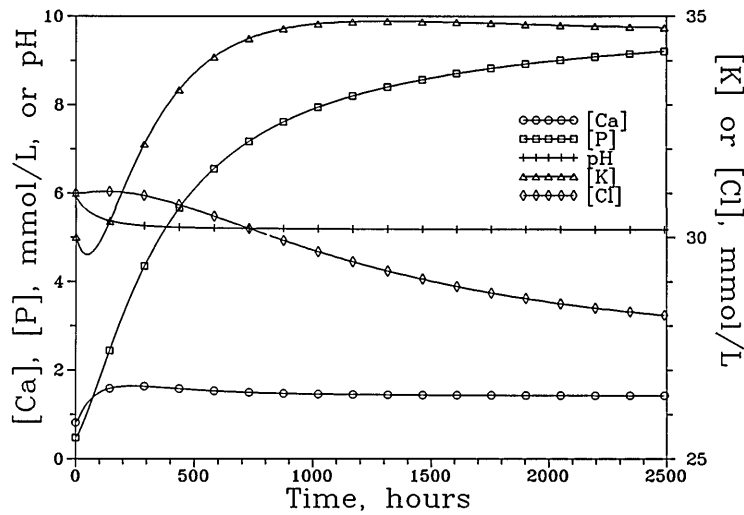


Figure 4a. The $[Ca]_T$, $[P]_T$, $[K]_T$, and $[Cl]_T$ of the "lesion" solution as a function of time for the system with the cation-permselective membrane and a "plaque" pH of 4.5.

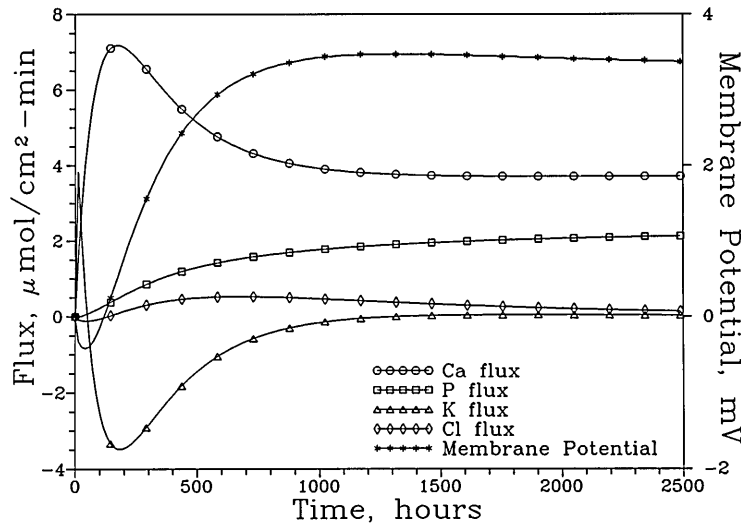


Figure 4b. The fluxes of these components and the membrane potential over the same time period.

Figure 5a shows the $[Ca]_T$, $[P]_T$, $[K]_T$, $[Cl]_T$, and the pH of the "lesion" solution as a function of time for the system with the anion permselective membrane. The fluxes of these components and the membrane potential during the same time period are shown in Fig. 5b. It is seen from Fig. 5b that during the initial period, e.g., the first 5 h, the anion permselective nature of the membrane allowed the P ions to diffuse out readily. This and the inward diffusion of H^+ (as described in "Methods," in the present model H^+ ion transport was

not impeded by the anion permselective membrane) produced a negative membrane potential. The negative potential prompted an inward diffusion of Cl^- ions which gradually diminished as the steady state was approached. The changes in concentrations of the various components were relatively small. At steady state the $[Ca]_T$ increased slightly from 0.741 to 0.861 mmol/L, and the $[P]_T$ decreased from 0.444 to 0.425 mmol/L, resulting in an increase in $[Ca]_T/[P]_T$ ratio from 1.67 to 2.03. The $[K]_T$ decreased from 30.00 to 29.90 mmol/L,

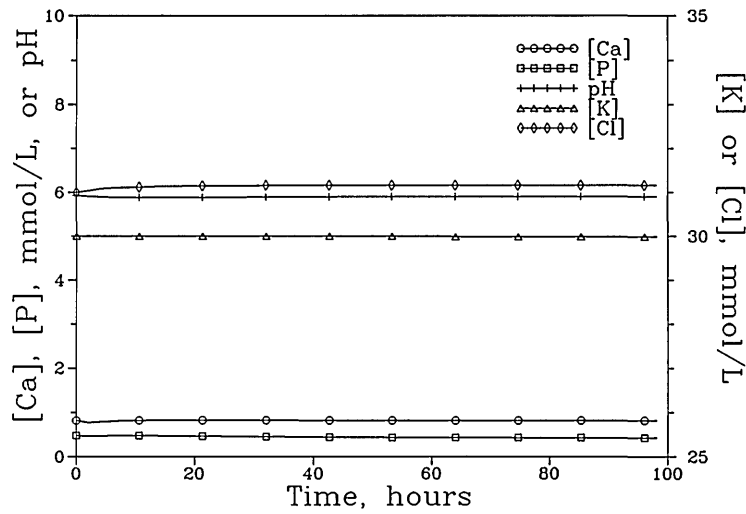


Figure 5a. The $[Ca]_T$, $[P]_T$, $[K]_T$, and $[Cl]_T$ of the “lesion” solution as a function of time for the system with the anion-permselective membrane and a “plaque” pH of 4.5.

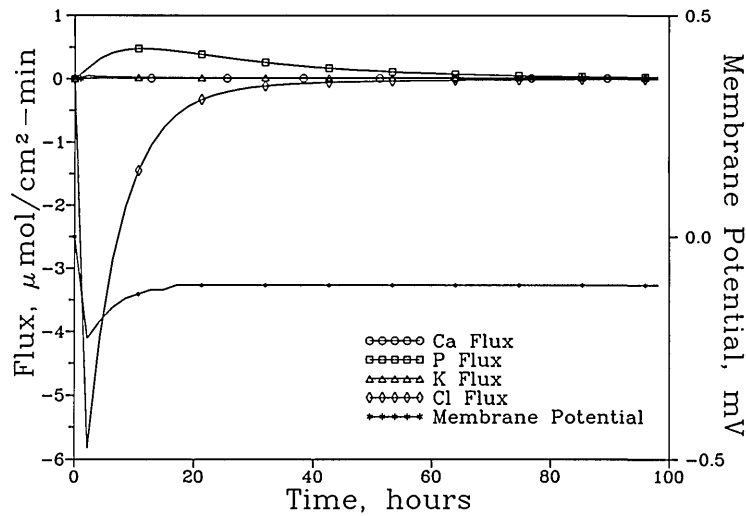


Figure 5b. The fluxes of these components and the membrane potential over the same time period.

and $[Cl]_T$ increased from 31.00 to 31.17 mmol/L. The fluxes of $(Ca)_T$ and $(P)_T$ were 0.00963 and 0.00665, respectively. These values are over 100 times smaller than those in the system with the non-selective membrane.

4. Discussion

The mathematical caries model described in the present study is a simulation of the experimental bench-scale caries model reported previously

[9–11]. The model was aimed at examining the interactions between the diffusion and dissolution processes that occur during the caries progression. Because in this model the solution species were allowed to diffuse across an infinitely thin barrier separating the “lesion” from the “plaque,” the model is inherently limited in that it does not address certain characteristics of a true lesion such as the presence of concentration gradients within the lesion. The present model also does not describe the mechanism for the formation of the mineral

dense surface layer. On the other hand, the model clearly demonstrated the effects of membrane permselectivity on lesion composition and rate of demineralization. The results of the simulations parallel closely those obtained in the bench-scale caries model in several ways as described below.

As described in Sec. 2, the compositions of the "plaque" solutions are such that they had the same HCl and KCl concentrations as those of the initial saturated solution in the "lesion" compartment but had lower amounts of OHAp dissolved (Table 3). Consequently, if one were to dissolve OHAp in any of the "plaque" solutions until saturation was reached, the solution would be the same as the initial "lesion" solution. The fact that in many cases the steady state $[Ca]_T$ and/or $[P]_T$ of the "lesion" solution became greater than the corresponding values in the initial "lesion" solution demonstrates the importance of the membrane effects on OHAp dissolution.

The $[Ca]_T/[P]_T$ ratio of the "lesion" solution at steady state was significantly lower than the initial ratio of 5/3 for the system with the cation-selective membrane and higher for the system with the anion-selective membrane [9,10]. Although the membrane potentials were relatively small due to the presence of a background electrolyte [10], i.e., 30 mmol/L of KCl, the redistribution of $[K]_T$ and $[Cl]_T$ in accordance with the membrane potential led to the significant change in $[Ca]_T/[P]_T$ as mentioned above.

For a given cariogenic challenge, i.e., a given "plaque" pH, the rate of demineralization is highly dependent on the membrane permselectivity (Table 4). It is worth noting that although the cationic permselective membrane reduces the diffusion of all anions, it actually led to significantly increased fluxes of Ca and P when compared to those obtained with the nonselective membrane. On the other hand, the anionic permselective membrane, which reduces the diffusion of all cations (except H^+), decreased the fluxes by a hundred fold.

The above findings, which are in good agreement with the experimental data, are a direct consequence of the diffusion-dissolution interactions. Previously reported mathematical models for caries [3-7,31,32], although possibly more sophisticated in some respects, have not been able to demonstrate this important phenomenon that has been confirmed in both bench-scale [9-11] and microanalytical [1,2] caries models. One model [31,32] utilizes coupled diffusion as a basis for describing the effects of diffusion on dissolution. This model, which

becomes mathematically complicated when the number of components is three or higher, was not developed to study the effects of membrane permselectivity on rate of demineralization.

In this initial assessment of the simulation model, the same "plaque" solutions as those employed in the bench-scale model were used. In future studies, "plaque" solutions with compositions that mimic more closely those of real plaque under cariogenic conditions should be used. The effect of weak acids such as lactic or acetic acid in the "plaque" compartment will differ from that of HCl because the weak acid will be only partially dissociated in the pH range associated with cariogenic conditions. The presence of fluoride in the "plaque" solution or the presence of fluorapatite (FAP) in the enamel "lesion" should produce significant effects on the composition of the lesion and the rate of demineralization [33].

Since the demineralization occurs primarily at the advancing front of the lesion, the demineralizing acid must be transported from the plaque through the diffusion barrier (the intact layer and the body of the lesion) to the advancing front in order to effect demineralization. Similarly, the solubilized ions, e.g., Ca^{2+} , $H_2PO_4^-$, etc., must be transported from the advancing front of the "lesion" towards the plaque. Thus, concentration gradients of all the diffusion species exist within the barrier. Although the present model is an approximation of the diffusion process taking place during subsurface demineralization, it clearly demonstrated the results of the interactions between the diffusion and dissolution processes. A model that allows for a diffusion barrier with a finite thickness such that concentration gradients of the diffusing species may exist within the barrier should further improve the ability to predict the effects of various factors on the caries process.

5. Appendix A

Figure 2 shows the solubility isotherms of OHAp expressed as the logarithms of the Ca and P concentrations of a series of saturated solutions. The curve labeled [0] (Insert) represents the isotherm in the 3-component system, $Ca(OH)_2-H_3PO_4-H_2O$, where no "foreign" (noncalcium, nonphosphate) ions are present. $U(-)$ [34] represents the concentration of a foreign acidic component such as Cl^- . Similarly $U(+)$ denotes the concentration of Na^+ if NaOH is a foreign component. Thus the label " $-[3]$ " (" $+[3]$ ") is to be interpreted as the sum of the dissociated foreign acid

(base) ions and charged ion-pairs at a concentration of 10^{-3} eq/L, i.e., $pU(-) = 3$. If several foreign components $U(\pm) = |\sum_i z_i C_i|$ represents a net "fourth component," where C_i is the concentration of the i th "foreign" ion or ion-pair, z_i is its valence, and $pU(\pm) = -\log U(\pm)$. $U(+)$ denotes an excess of foreign base over acid in the summation and contrariwise for $U(-)$. Each curve in Fig. 2 represents the applicable solubility of OHAp for a given pU value.

Acknowledgments

This investigation was supported, in part, by USPHS Research Grant DE05354 to the American Dental Association Health Foundation from the National Institutes of Health—National Institute of Dental Research and is part of the dental research program conducted by the National Institute of Standards and Technology in cooperation with the American Dental Association Health Foundation.

6. References

- [1] G. L. Vogel, C. M. Carey, L. C. Chow, and W. E. Brown, *Caries Res.* **21**, 310 (1987).
- [2] G. L. Vogel, C. M. Carey, L. C. Chow, T. M. Gregory, and W. E. Brown, *J. Dent. Res.* **67**, 1172 (1988).
- [3] S. O. Zimmermann, *Bull. Math. Biophys.* **28**, 443 (1966).
- [4] F. J. Holly and J. A. Gray, *Arch. Oral Biol.* **13**, 319 (1968).
- [5] J. D. B. Featherstone, J. F. Duncan, and T. W. Cutress, *Arch. Oral Biol.* **24**, 101 (1979).
- [6] J. W. E. Van Dijk, J. M. P. M. Borggreven, and F. C. M. Driessens, *Caries Res.* **13**, 169 (1979).
- [7] J. Christoffersen and J. Arends, *Caries Res.* **16**, 433 (1982).
- [8] W. E. Brown, *J. Dent. Res.* **53**, 204 (1974).
- [9] L. C. Chow and W. E. Brown, *J. Dent. Res.* **63**, 868 (1984).
- [10] W. E. Brown and L. C. Chow, *J. Dent. Res.* **65**, 1115 (1986).
- [11] L. C. Chow and W. E. Brown, *IADR Progr. Abst.* **61**, #488 (1982).
- [12] K. J. Laidler and J. H. Meiser, *Physical Chemistry*, Benjamin/Cummings Publishing Co., Inc., 1982, pp. 281–3.
- [13] R. C. Weast, *CRC Handbook of Chemistry and Physics*, 66th Edition, CRC Press, Inc., Boca Raton, FL (1986) p. D168.
- [14] N. Lakshminarayanaiah, *Transport Phenomena in Membranes*, Academic Press, New York, 1969.
- [15] E. C. Moreno, W. E. Brown, and G. Osborn, *Soil Sci. Soc. Am. Proc.* **24**, 97 (1960).
- [16] E. C. Moreno, T. M. Gregory, and W. E. Brown, *J. Res. Natl. Bur. Stand. (U.S.)* **70A**, 545 (1966).
- [17] R. G. Bates, *J. Res. Natl. Bur. Stand. (U.S.)* **47**, 127 (1951).
- [18] R. G. Bates and S. F. Acree, *J. Res. Natl. Bur. Stand. (U.S.)* **30**, 129 (1943).
- [19] N. Bjerrum and A. Unmack, *Kgl. Danske Vidensk. Selskab. (Mat.-Fys.)* **9**, 5–206 (1929).
- [20] H. S. Harned and B. B. Owen, *The Physical Chemistry of Electrolytic Solutions*, Reinhold Publishing Corp., New York (1958) Chap. 15.
- [21] R. G. Bates, *Determination of pH: Theory and Practice*, John Wiley & Sons, Inc., New York (1973) p. 450.
- [22] T. M. Gregory, E. C. Moreno, and W. E. Brown, *J. Res. Natl. Bur. Stand. (U.S.) Part A Phys. Chem.* **74A**, 461 (1970).
- [23] L. G. Sillen and A. E. Martell, *Stability Constants of Metal-ion Complexes, Supplement No. 1, Special Publication No. 25*, The Chemical Society, Burlington, London (1971).
- [24] L. G. Sillen and A. E. Martell, *Stability Constants of Metal-ion Complexes, Special Publication No. 17*, The Chemical Society, Burlington, London (1964).
- [25] H. McDowell, T. M. Gregory, and W. E. Brown, *J. Res. Natl. Bur. Stand. (U.S.) Part A Phys. Chem.* **81A**, 273 (1977).
- [26] M. S. Tung, N. Eidelman, B. Sieck, and W. E. Brown, *J. Res. Natl. Bur. Stand. (U.S.)* **93**, 613 (1988).
- [27] T. M. Gregory, E. C. Moreno, J. M. Patel, and W. E. Brown, *J. Res. Natl. Bur. Stand. (U.S.) Part A Phys. Chem.* **78A**, 667 (1974).
- [28] J. L. Meyer and E. D. Eanes, *Calcif. Tiss. Res.* **25**, 59 (1978).
- [29] K. Levenberg, *Q. Appl. Math.* **2**, 164 (1944).
- [30] D. W. Marquardt, *J. Soc. Ind. Appl. Math.* **11**, 431 (1963).
- [31] P. Anderson and J. C. Elliott, *Caries Res.* **21**, 522 (1987).
- [32] D. G. Leaist, P. Anderson, and J. C. Elliott, *J. Chem. Soc. Faraday Trans.* **86**, 3093–3095 (1990).
- [33] H. C. Margolis, E. C. Moreno, and B. J. Murphy, *J. Dent. Res.* **65**, 23 (1986).
- [34] W. E. Brown, *Environmental Phosphorus Handbook*, E. M. Griffith, A. Beeton, J. H. Spencer, and D. T. Mitchell, Eds., Wiley & Sons, New York, 1973.

About the authors: Mr. Thomas M. Gregory (retired) was Project Leader, Dr. Laurence C. Chow is Chief Research Scientist, and Mr. Clifton M. Carey is Research Associate in the Dental Chemistry Program with the Paffenbarger Research Center, American Dental Association Health Foundation at NIST.

Program Report

The Advanced Technology Program: A New Role for NIST in Accelerating the Development of Commercially Important Technologies

Volume 96

Number 5

September–October 1991

**Brian C. Belanger,
George A. Uriano, and
Raymond G. Kammer**

National Institute of Standards
and Technology,
Gaithersburg, MD 20899

The Advanced Technology Program (ATP) is a new extra mural program operated by the National Institute of Standards and Technology (NIST) for the Department of Commerce's Technology Administration. The ATP will help enhance U.S. competitiveness by funding the development of pre-competitive, generic technologies in partnership with industry. This paper

describes the ATP, the first ATP awards made by NIST, and the prognosis for the success of the ATP.

Key words: advanced technology; cooperative agreements; extra mural; generic technology; industrial competitiveness.

Accepted: July 18, 1991

1. Introduction

The National Institute of Standards and Technology (NIST), formerly the National Bureau of Standards (NBS), has a well-deserved reputation for working effectively with industry. However, until recently, NIST assistance to industry involved primarily measurement and standards expertise developed within NIST laboratories and disseminated via mechanisms such as calibration services, standard reference materials, standard reference data, and information needed for the establishment of technical specifications. As a result of the Omnibus Trade and Competitiveness Act of 1988, NIST now has an augmented role in enhancing industrial competitiveness and promoting U.S. economic growth. The Advanced Technology Program is one of several new responsibilities assigned to NIST that contribute to this increased emphasis on industrial competitiveness. (Others

include the Malcolm Baldrige National Quality Award, the Manufacturing Technology Centers Program, and the State Technology Extension Program.)

The ATP provides research and development grants in the form of cooperative agreements to individual companies, independent research institutes, or joint ventures. Awards are for the development of precompetitive, generic technology. These terms are defined as follows:

Generic Technology: A concept, component, or process, or the further investigation of scientific phenomena, that has the potential to be applied to a broad range of products or processes. A generic technology may require subsequent research and development for commercial application.

Precompetitive Technology: R&D activities up to the stage where technical uncertainties are sufficiently reduced to permit assessment of commercial potential and prior to development of application-specific commercial prototypes. At this stage, for example, results can be shared within a consortium that can include potential competitors without reducing the incentives for individual firms to develop and market commercial products and processes based on the results.

During the Congressional deliberations on the Omnibus Trade and Competitiveness Act of 1988, there was considerable debate regarding the proper role for the Federal government in supporting civilian technology R&D. Today there is a consensus within both the Administration and the Congress that support for precompetitive, generic technology development is an appropriate role for the Federal government. For example, the September 26, 1990 report, "U.S. Technology Policy," prepared by the President's Office of Science and Technology Policy, stated (p. 5) that it is the responsibility of the Federal government to "participate with the private sector in precompetitive research on generic, enabling technologies that have the potential to contribute to a broad range of government and commercial applications."

In a March 7, 1990 speech to the American Electronics Association, President Bush said, "This Administration is also committed to working with you in the critical precompetitive development stage where the basic discoveries are converted into generic technologies that support both our economic competitiveness and our national security. Here again we can help to level the international playing field on which you compete." At the November 13, 1990 ceremony to present the National Medals of Science and of Technology, the President said, "Today our government must help carry that research forward and contribute to the development of generic technologies that build on basic discoveries. If America is to maintain and strengthen our competitive position, we must continue not only to create new technologies but learn to more effectively translate those technologies into commercial products. In this way, we can help leverage the R&D of the private sector, helping whole industries advance in an increasingly competitive global market."

In keeping with these guidelines, projects supported by the ATP involve R&D at a stage between basic research and specific commercial product development. To be appropriate for ATP funding, a project must be characterized by challenging technical problems that must be solved before further steps towards commercialization can take place. While the ATP supports projects having high technical risk, the potential benefits to the U.S. economy must be commensurate with that high risk.

2. ATP Eligibility

Two categories of applicants may apply for ATP awards: single applicants (U.S. companies or independent research institutes), and joint ventures. The rules for participation differ for the two types of applicants as noted below. (Most features of the ATP rule reflect explicit provisions of the ATP legislation.)

2.1 Single Applicants

Single applicants may be either companies or "independent research institutes." (Examples of well-known independent research institutes are the Stanford Research Institute (SRI), the Battelle Memorial Institute, and the Southwest Research Institute.) Universities and government laboratories may not apply directly to the ATP, although they may participate as subcontractors to single applicants or in joint ventures—assuming the minimum joint venture eligibility requirements have been met, as described in the next section.

Awards to single applicants cannot exceed \$2 million over a 3-year period. NIST cannot pay indirect costs for single applicants, therefore they must absorb overhead costs themselves or find other sponsors willing to cover these costs.

2.2 Joint Ventures

The ATP may fund joint ventures for up to 5 years. The dollar amount of any joint venture award is limited only by the total funding available for the ATP in any given year. Joint ventures must provide matching funds of at least 50% of the total cost of

the project.¹ Federal funds, whatever the source, do not count toward the matching funds requirement for joint ventures. Accordingly, the matching funds must be provided by the participants, by state and local governments, by private investors, or by some combination of these sources.

To be eligible for ATP awards, joint R&D ventures must consist of at least two organizations that agree to work together on the proposed R&D program. Both must be eligible to apply alone, and both must contribute toward the matching funds. Thus, a minimum-size joint venture must have at least two companies, two independent research institutes, or one of each, both of which are doing R&D and contributing toward the match. Joint ventures may also include any number of additional companies or independent research institutes, universities, and/or government laboratories, each of which may or may not contribute to the matching funds requirement and/or participate in the research.

2.3 NIST Participation in ATP-Funded Projects

NIST encourages its scientists and engineers to collaborate with joint venture or single applicant projects funded by the ATP, but NIST's intramural laboratory programs cannot receive funds from an ATP-funded project.² Although encouraged, collaboration with NIST is not a selection criterion, so a proposal featuring such collaboration will not score higher than one that does not.

¹ The term "matching funds" includes the following: 1) dollar contributions from state, county, city, company, or other sources; 2) the applicant's share of revenue from licensing and royalties; 3) fees for services performed; 4) in-kind contributions of full-time personnel; 5) contributions of a pro rata share of part-time personnel that the Program deems essential to carrying out the proposed experimental work program and who devote at least 50% of their time to the program; and 6) in-kind value of equipment that the Program deems essential to carrying out the proposed experimental work program, which may include either the purchase cost of new equipment or the depreciated value of previously purchased equipment. (Refer to the ATP Rule, 15 CFR 295.2(e), for additional restrictions on matching funds.)

² Legislation has been considered by the Congress that would permit the NIST Director to utilize a small portion of the ATP budget to support work inside NIST to foster collaboration with projects selected for funding, where such work would enhance the chances for success of the ATP project and complement NIST's internal R&D programs.

2.4 Participation in the ATP by Foreign-Owned Companies

Congress has debated whether foreign-owned firms should be allowed to compete for ATP awards, and if so, under what conditions. No restrictions regarding the nationality of corporate ownership were included in the legislation that established the ATP other than statements to the effect that the program was intended to help "U.S. businesses." The legislation did not define "U.S. business." During the first competition, NIST interpreted this provision of the law such that companies committed to conducting the proposed R&D in the United States and providing evidence that they would also carry out in the U.S. subsequent manufacturing resulting from the R&D, were eligible—whatever the corporate owners' nationality.

The Fiscal Year 1991 Department of Commerce Appropriations Bill contained language that placed additional restrictions on foreign-owned companies that wished to participate in the ATP. Since an appropriation bill is only valid for the year of the appropriation, this legislative language will not apply to future ATP appropriations unless the Congress includes it in future authorization and/or appropriations bills (which seems likely). The language says that the ATP can fund only companies that make investments in the United States in research, development, and manufacturing; make significant contributions to employment in the United States; and agree to promote manufacturing within the United States of products resulting from the ATP-funded project.

Such companies must either 1) be a U.S. company (meaning more than 50%-owned by U.S. citizens), or 2) the Secretary of Commerce must determine that the applicant has a parent company incorporated in a country that affords U.S. companies equal access to programs analogous to the ATP, and affords adequate and effective protection for the intellectual property rights of U.S.-owned companies.

3. Proposal Evaluation

3.1 Selection Criteria

ATP proposals are judged on five selection criteria:

- Scientific and technical merit (20%)
 - Quality and innovativeness of the proposal
 - Appropriateness of the technical risk and feasibility of the project (This factor addresses whether the degree of risk is commensurate with the potential payoff. Note that the ATP is not adverse to high risk where the payoff is correspondingly high.)
 - Coherency of technical plan
 - Systems integration and multi-disciplinary planning (This factor involves the appropriate use of “concurrent engineering.”)
- Broad-based (commercial) benefits (20%)
 - Potential broad impact on U.S. technology and knowledge base
 - Potential to improve U.S. economic growth and productivity of a broad spectrum of sectors or businesses
 - Timeliness of the proposal
- Technology Transfer Benefits of the Proposal (20%)
 - Evidence that if the project is successful, the participants will pursue further development of the technology toward commercial application
 - Addresses technology transfer requirements to assure prompt and widespread use
- Experience and Qualifications of Proposing Organization (20%)
 - Staffing, facilities, equipment, other resources
 - Quality and appropriateness of full-time technical staff
 - Design and manufacturing tools adequate for laboratory prototype development
- Proposer’s Level of Commitment and Organizational Structure (20%)
 - Level of commitment (contribution of personnel, equipment, facilities, etc.)
 - For joint ventures, appropriateness of structure (i.e., horizontal vs. vertical integration)
 - For joint ventures, appropriate participation by small businesses.
 - Evidence of commitment to complete program and continue beyond period of Federal funding
 - Potential return to the Government (royalty and licensing fees)

3.2 The Selection Process

The “Selecting Official” for the first competition was Dr. John W. Lyons, NIST’s Director. He appointed a 10-person Source Evaluation Board (SEB). The SEB was responsible for ranking the proposals against the selection criteria and recommending those most deserving of funding.

The SEB included senior level NIST technical managers whose backgrounds reflected the disciplines represented by the proposals, (e.g., chemistry, physics, electrical engineering, computer science, materials science, etc.), as well as managers with considerable experience in business planning, business development, finance, and intellectual property. The SEB used technical experts and business experts to prepare written reviews of proposals. All reviewers were screened carefully to eliminate conflicts of interest and were required to sign non-disclosure agreements.

The SEB considered carefully the recommendations made by the technical and business reviewers, but was not bound by them. In ranking proposals, the SEB discussed each reviewer’s comments on the merits (or lack thereof) of each proposal, but exercised its independent judgment as well.

In the first competition, 249 proposals were received. As a first step, the SEB screened them to ensure compliance with the solicitation requirements. For example, proposals submitted directly by universities were rejected because the ATP legislation does not allow direct funding of universities. Similarly, proposals submitted by joint ventures not providing more than 50% matching funds were rejected, as were proposals from single applicants that did not agree to pay indirect costs. Forty proposals were rejected during the initial screening stage.

The remaining proposals were subjected to a thorough technical review by 397 different technical experts from NIST, other government agencies and laboratories, universities, and the private sector. Federal agencies and laboratories that helped with the reviews included the Defense Advanced Research Projects Agency (DARPA), the Naval Research Laboratory, the Goddard Space Flight Center, the Department of Energy (DOE) and the DOE national laboratories, the Air Force Office of Scientific Research, the Army Corps of Engineers, the Office of Naval Research, and the National Institutes of Health.

The proposals with the highest technical merit (approximately the top third) were submitted to the business reviewers. Most business reviewers,

while drawn from different backgrounds than the technical reviewers, also had strong technical qualifications. They included: a retired dean of a business school, high-tech venture capitalists, vice presidents of engineering or R&D for large, high-tech corporations, and presidents of smaller technology-intensive companies. These individuals generally had considerable experience in transferring technologies from the R&D laboratory to production.

Twenty-one proposals that scored highest in both the technical and business reviews were designated as semifinalist proposals. Each semifinalist proposer presented an oral defense at NIST. During the oral defense, the SEB asked questions raised by the technical and business reviewers and requested clarifications of points not completely addressed in the written proposals. These oral defenses proved very helpful to the SEB in preparing the final rankings, because information surfaced that strengthened the case for funding certain proposals and weakened the case for others. While the SEB reserved the right to make site visits where appropriate, none were needed for any of the semifinalists.

4. Intellectual Property

Awardees are generally granted full title to intellectual property developed during ATP-funded projects. The Federal government retains a royalty-free, non-exclusive license to use the technology for government purposes, as is generally the case with Federally-funded programs. Current Federal laws and policies³ give the Federal government "march-in rights" that allows NIST to intercede if, after a reasonable period, the ATP awardee has failed to use the technology developed under the ATP project. There are also some restrictions under this act that limit the ability of the company or companies holding title to intellectual property developed during an ATP project to license it overseas without the permission of the Federal government.

³ Awards under the program will follow the policies and procedures on ownership to inventions made under grants and cooperative agreements that are set out in the Bayh-Doyle Act—Public Law 96-517 (35 U.S.C. Chapter 18), the Presidential Memorandum on Government Patent Policy to the Heads of Executive Departments and Agencies Dated February 18, 1983, and Part 401 of Title 37 of the Code of Federal Regulations, as appropriate.

5. Awards

The ATP announced its first awards on March 5, 1991. Appendix A provides a listing of the 11 projects selected in the first competition. They included five joint ventures and six single applicants. Small businesses participate in all of the joint ventures (and lead two of them), and four of the six single applicant awardees are small businesses. In the press release announcing the first awards, Commerce Secretary Robert A. Mosbacher said the awards "could lead to the birth of revolutionary products and processes in key U.S. industries and help boost the country's trade and competitiveness."

Several new joint R&D ventures formed specifically in response to the ATP solicitation. Because of the matching fund requirement (for joint ventures) and the indirect cost contribution (for single applicants), the approximately \$9 million provided by NIST for the first year of the projects selected is highly leveraged. A total of \$45.8 million was requested from the ATP over the duration of the 11 projects selected. The applicants' cost-sharing amounted to an additional \$51.7 million. Thus R&D valued at nearly \$100 million will result from these awards over a 5-year period.

6. The Future

Congress appropriated \$35.9 million for the ATP in Fiscal Year 1991 and the President's budget for FY 1992 also requests \$35.9 million. Initial reactions to the ATP's first competition by the Congress and U.S. industry appear favorable, and thus the program appears to have a bright future. The next request for proposals will be issued in the summer of 1991. Some of the \$35.9 million in FY 1991 funds will be used to fund the second year of the ongoing projects, but there should be approximately \$20 million available for beginning new projects.

By the mid-1990s, an assessment will be available of the degree of success of the first ATP-funded projects. Certainly, not all ATP projects will be successful. Since the ATP intentionally funds high-risk, potentially high-leverage projects, a number will undoubtedly fail. However, NIST is optimistic that enough will succeed to justify the expenditures. NIST is currently developing measures of success for the ATP. As experience is gained, NIST should become increasingly proficient at identifying and selecting high leverage projects that will

contribute to enhanced competitiveness of U.S. businesses and promote U.S. economic growth.

For more information on the Advanced Technology Program, contact:

Advanced Technology Program,
A402 Administration Bldg.,
National Institute of Standards and Technology,
Gaithersburg, MD 20899
(301) 975-5187

8. Appendix A. – The Eleven Proposals Selected for Awards in Competition 90-01

Volume Holographic Mass Storage Subsystem Microelectronics & Computer Technology Corporation (MCC)

Radically new form of dense, ultra-fast computer memory storage (potentially replacing disk drives and magnetic tape) would have applications from laptop computers to super-computers. Data stored as holographic images in photorefractive crystals.

First-year request: \$823 K

Nonvolatile Magnetoresistive Semiconductor Technology

Nonvolatile Electronics, Inc.

Magnetoresistive memory (MRAM) for computers is nonvolatile—the information is not lost when the power is shut off. Has applications across entire spectrum of microelectronic design.

First-year request: \$599 K

Short-Wavelength Sources for Optical Recording National Storage Industry Consortium

Program to develop unique integrated, solid-state laser source for read/write heads of optical memory devices (like CDs). Identified in the Technology Administration's Emerging Technologies report as key technical barrier. \$50,000 initial grant contingent on further development of the joint venture, including Applied Magnetics, Bernoulli Optical Systems, Eastman Kodak, IBM, Maxoptix Corp., and the University of Arizona.

Initial \$50 K Planning Grant Awarded

Tunable Deep UV and VUV Solid-State Laser Source

Light Age, Inc.

Application of recent developments in laser technology to produce high-average-power ultraviolet lasers for medical, electronic materials processing, and scientific applications that are cheaper, safer, more reliable, and easier to use than current products. Light Age is an EPIC 100 firm, selected by the Commerce Department's International Trade Administration for special export promotion.

First-year request: \$627 K

New User-Interface for Computers Based on On-Line Recognition of Natural Handwriting Communication Intelligence Corporation (CIC)

Cursive handwriting input for computers "could well be as revolutionary as the original PC" (Fortune, 11 Feb 91). CIC plans a robust, natural handwriting-recognition system that is user-independent, a key limitation of most current systems.

First-year request: \$671 K

Printed Wiring Board Interconnect Systems

National Center for Manufacturing Sciences, Inc. (NCMS)

Used in virtually all electronics equipment. AT&T, Texas Instruments, Digital Equipment Corporation, and Hamilton Standard Interconnect are joined through NCMS to develop new PWB materials and production technology for a \$25 billion world market.

First-year request: \$2,370 K

Advanced Manufacturing Technology for Low-Cost Flat Panel Displays

Advanced Display Manufacturers of America Research Consortium

A joint venture by several relatively small U.S. producers of flat-panel displays for computers—competing against large, vertically integrated Japanese firms—to develop key production and testing technologies for a multi-billion-dollar industry.

First-year request: \$1,251 K

**Fabrication and Testing of Precision Optics
for Soft X-Ray Projection Lithography**

AT&T Bell Laboratories

Attacking a key problem limiting projection x-ray lithography (needed for future generations of very compact integrated circuits): the manufacture, testing, and assembly of relatively large-scale x-ray optics. An estimated 75 percent of the ATP funds will go to small-business subcontractors.

First-year request: \$955 K

About the Authors: Brian C. Belanger is the Deputy Director of the Advanced Technology Program. George A. Uriano is the Director of the ATP. Raymond G. Kammer, the Deputy Director of NIST, chaired the first ATP Source Evaluation Board.

**Solid-State Laser Technology for Point-Source
X-Ray Lithography**

Hampshire Instruments, Inc. & McDonnell
Douglas Electronic Systems Co.

Joint venture led by a small business to exploit recent developments in laser technology for a low-cost, high-performance x-ray source suitable for microlithography and the design and production of advanced integrated circuits.

First-year request: \$1,090 K

**Advanced Compensation Techniques for
Enhancing Machine-Tool Accuracy**

Saginaw Machine Systems, Inc.

Seeks more general, economical solution to problem of correcting for errors in machining caused by thermal expansion and contraction of the machine tool. Wide potential applications in U.S. machine tool industry. Cost and accuracy are the two key selling points in machine tools.

First-year request: \$266 K

Advanced Thallium Superconductor Technology

E. I. du Pont de Nemours & Co.

Development of thin-film fabrication techniques for a new, proprietary high-temperature superconductor invented by Du Pont. Project includes developing fabrication techniques and creating representative superconducting electronic devices to demonstrate feasibility.

First-year request: \$370 K

Letter to the Editor
A List of New Group Divisible Designs

Volume 96

Number 5

September–October 1991

Kishore Sinha

Birsa Agricultural University,
Department of Statistics,
Ranchi-834006, India

Group divisible designs are the most important class of partially balanced incomplete block (PBIB) designs. A list of new group divisible designs with $r, k \leq 10$ is provided.

Key words: experimental design; group divisible design; partially balanced designs.

Accepted: June 13, 1991

1. Introduction

Group divisible designs are the most important class of partially balanced incomplete block (PBIB) designs. Clatworthy, Cameron, and Speckman at the National Bureau of Standards [3] tabulated group divisible designs with $r, k \leq 10$. Since then, a good number of new group divisible designs not listed in reference [3] have been reported by various authors in different journals. Here, a list of

new group divisible designs not found in the tables in reference [3] is provided.

2. New Group Divisible Designs

Table 1 gives new group divisible designs with $r, k \leq 10$.

Table 1. New group divisible designs with $r, k \leq 10$

No.	v	r	k	b	m	n	λ_1	λ_2	E^a	Source ^b
1	16	9	3	48	8	2	4	1	0.69	BP[1]
2	18	10	3	60	9	2	4	1	0.69	F[7]
3	12	7	4	21	6	2	1	2	0.82	F[7]
4	12	7	4	21	2	6	3	1	0.79	JT[8]
5	12	8	4	24	4	3	3	2	0.82	JT[8]
6	12	9	4	27	2	6	3	2	0.82	JT[8]
7	12	9	4	27	6	2	7	2	0.75	F[7]
8	12	10	4	30	6	2	0	3	0.81	F[7]
9	14	10	4	35	7	2	6	2	0.80	F[7]
10	16	6	4	24	8	2	4	1	0.78	BP[1]
11	18	10	4	45	6	3	0	2	0.80	F[7]
12	20	8	4	40	10	2	6	1	0.76	BP[1]
13	22	8	4	44	11	2	2	4	0.77	F[7]
14	24	9	4	54	12	2	5	1	0.77	F[7]
15	26	10	4	65	13	2	6	1	0.76	F[7]
16	14	10	5	28	7	2	4	3	0.86	JT[8]
17	15	8	5	24	3	5	3	2	0.86	JT[8]
18	15	8	5	24	5	3	4	2	0.85	JT[8]
19	15	10	5	30	3	5	5	2	0.84	S[10]
20	22	10	5	44	11	2	0	2	0.84	F[7]
21	12	7	6	14	6	2	5	3	0.91	JT[8]
22	12	9	6	18	6	2	5	4	0.91	F[7]
23	12	9	6	18	3	4	7	3	0.89	BP[2]
24	12	10	6	20	3	4	6	4	0.91	JT[8]
25	16	9	6	24	4	4	7	2	0.86	S[10]
26	12	7	7	12	3	4	6	3	0.92	BP[2]
27	16	7	7	16	4	4	2	3	0.91	JT[8]
28	16	7	7	16	8	2	0	3	0.91	D[4]
29	21	7	7	21	7	3	3	2	0.90	F[7]
30	24	7	7	24	8	3	0	2	0.89	F[7]
31	35	7	7	35	7	5	3	1	0.87	F[7]
32	45	7	7	45	15	3	0	1	0.88	DR[6]
33	42	8	8	42	7	6	4	1	0.88	F[7]
34	16	9	9	16	4	4	4	5	0.95	JT[8]
35	18	10	9	20	3	6	4	5	0.79	JT[8]
36	20	9	9	20	4	5	3	4	0.94	JT[8]
37	20	9	9	20	10	2	0	4	0.93	D[4]
38	24	9	9	24	6	4	4	3	0.93	S[9]
39	38	9	9	38	19	2	0	2	0.91	DR[6]
40	40	9	9	40	10	4	0	2	0.91	DN[5]
41	49	9	9	49	7	7	5	1	0.89	F[7]
42	21	10	10	21	7	3	9	4	0.94	F[7]
43	21	10	10	21	3	7	8	3	0.93	BP[2]
44	24	10	10	24	8	3	3	4	0.94	S[9]
45	28	10	10	28	7	4	6	3	0.93	F[7]
46	56	10	10	56	7	8	6	1	0.89	F[7]

^a E stands for average efficiency factor.

^b The abbreviations BP, D, DN, DR, F, JT, and S stand for Bhangwandas and Parihar, Dey, Dey and Nigam, De and Roy, Freeman, John and Turner, and Sinha, respectively.

3. References

- [1] Bhagwandas and Parihar, J. S., Some new group divisible designs, *J. Statist. Plan. Inference* **4**, 321–323 (1980).
- [2] Bhagwandas and Parihar, J. S., Some new series of regular group divisible designs, *Commun. Statist., Th. Method* **11**, 761–768 (1982).
- [3] Clatworthy, W. H., Cameron, J. M., and Speckman, J. A., Tables of two-associate-class partially balanced designs, *Natl. Bur. Stand. (U.S.), Appl. Math. Ser.* **63** (1973).
- [4] Dey, A., Construction of regular group divisible designs, *Biometrika* **64**, 647–649 (1977).
- [5] Dey, A. and Nigam, A. K., Construction of group divisible designs, *J. Indian Soc. Agric. Statist.* **37**, 163–166 (1985).
- [6] De, A. K. and Roy, B. K., Computer construction of some group divisible designs, *Sankhya (B)* **52**, 82–92 (1990).
- [7] Freeman, G. H., A cyclic method of constructing regular group divisible incomplete block designs, *Biometrika* **63**, 555–558 (1976).
- [8] John, J. A. and Turner, G., Some new group divisible designs, *J. Statist. Plan Inference* **1**, 103–107 (1977).
- [9] Sinha, K., A method of construction of regular group divisible designs, *Biometrika* **74**, 443–444 (1987).
- [10] Sinha, K., A method of constructing PBIB designs, *J. Indian Soc. Agric. Statist.* **41**, 313–315 (1989).

About the author: Dr. Kishore Sinha is an Associate Professor in the Department of Statistics, Birsa Agricultural University, Ranchi, India.

Letter to the Editor

*Silicon Reference Materials Certified
for Isotope Abundances*

Volume 96

Number 5

September–October 1991

S. Valkiers and P. De Bièvre

Central Bureau for Nuclear
Measurements,
Commission of the European
Communities,
Joint Research Centre,
B-2440, Geel, Belgium

G. Lenaers

University of Antwerpen,
Chemistry Department,
B-2610 Antwerpen-Wilrijk,
Belgium

and

H. S. Peiser

National Institute of Standards
and Technology,
Gaithersburg, MD 20899

In a series of gas mass-spectrometric measurements performed near the highest attainable accuracy, samples from two highly homogeneous batches of silicon crystals and silica powder were compared directly with a synthetic mixture of the three stable isotopes of silicon. Thereby, this work not only established the “absolute” atomic weight of these batches, but also makes portions of these batches available as an Isotopic Reference Material for accurate isotopic abundance measurements in geochemical and other isotope-abundance studies of silicon.

Key words: absolute abundances; atomic weights; isotope abundances; isotopic mass spectrometry; isotope reference materials; silicon; silicon tetrafluoride.

Accepted: July 16, 1991

A precise determination of differences of a property between similar specimens is more easily achieved than absolute accuracy in the measurement. In mass-spectrometric determinations of isotope abundances, variations are often small—but significant relative to achievable precision—between specimens from differing chemical, physical, geological, or biological processes. It is just these variations that open new fields of study in geochemistry, chemical technology, solid-state physics, archeology, analysis of trace elements, etc. Thus, as in other fields, credible isotope reference materials

(IRMs) are needed which must fulfill the following criteria:

- i) near perfect homogeneity within and between samples of the IRM;
- ii) wide and open availability of IRM samples in adequate amounts so that different laboratories can refer to the “same” material;
- iii) full chemical and physical characterization of the IRM; and
- iv) direct absolute measurement of the isotopic composition of the IRM near the highest contemporary accuracy.

The fourth criterion demands a direct atomic-weight and isotopic composition determination recognized to have been carried out near the highest accuracy so far achieved. That in turn implies the preparation of synthetic mixtures from highly enriched isotope constituents. During the past 25 years such measurements have been rarely made and only on a total of about 15 elements. The introduction therefore of two new silicon IRMs is an event of note.

A smaller batch of small silicon single crystals (total mass ~ 10 g) and a larger batch of SiO₂ grains (10 kg Optipur Merck¹) have been characterized for their isotopic homogeneity, isotopic composition and relative atomic weight, $A_r(\text{Si})$. This has resulted in two IRMs: IRM-017 (Si) and IRM-018 (SiO₂), portions of which are now available from the Central Bureau for Nuclear Measurements (CBNM).

The isotopic measurements on the three stable isotopes of silicon were performed by gas isotope mass spectrometry [1] on samples which were converted to SiF₄ gas by the following chemical steps carried out on a large number of portions. In step 1 samples of the silicon candidate reference material were dissolved in warm dilute sodium hydroxide, and the solution of sodium silicate was converted to aqueous silicic acid in an acidic ion exchanger. Water from that solution was evaporated and the residue heated to 950 °C to form silica (SiO₂). Steps 2 and 3 were applied to samples of both candidate reference materials. In step 2 the silica was dissolved in hydrofluoric acid from which barium hexafluorosilicate was precipitated. In step 3 the barium salt was heated to 540 °C in an evacuated vessel, and the silicon tetrafluoride was frozen out.

The isotope-abundance ratio measurements on SiF₄ (²⁹SiF₃⁺/²⁸SiF₃⁺, ³⁰SiF₃⁺/²⁸SiF₃⁺) were calibrated by means of a gravimetric mixture of the three enriched isotopes [2]. The amounts of the enriched isotopes used to prepare the mixture were chosen such that the prepared ratios were close to those for natural silicon. With this synthetic isotope mixture the mass-spectrometric correction factors K ($K = \text{ratio as prepared}/\text{ratio as observed}$) for the observed ratios were determined. The IRMs were measured in the same series of tightly controlled

measurements from which the effect of any inevitable instrumental drift could be minimized. In this way the above correction factors could be applied to these IRM measurements, resulting in "absolute" isotope abundances and atomic weights for both materials (Table 1). The measurement technique for gas isotopic measurements as it was developed by the authors for this work will be described in more detail in other future publications.

Table 1. Isotopic Composition and $A_r(\text{Si})$ for both IRMs. Uncertainties are indicated under the digits to which they relate and are computed on a two-standard deviation basis. (The mass spectrometric measurements on isotopic reference materials 017 and 018 were carried out during a period just before a filament change became necessary. An increasing instability of the old filament was mainly responsible for the larger uncertainties when compared with those for an entirely different silicon crystal that happens to have a virtually identical relative atomic weight.)

	CBNM-IRM-017 Si	CBNM-IRM-018 SiO ₂
Molar isotope abundance ratios		
²⁹ Si/ ²⁸ Si	0.050 69 12	0.050 83 12
³⁰ Si/ ²⁸ Si	0.033 52 10	0.033 60 10
Molar abundances (fractional)		
²⁸ Si	0.922 33 14	0.922 14 14
²⁹ Si	0.046 75 11	0.046 88 11
³⁰ Si	0.030 92 8	0.030 98 8
Mass percentages		
²⁸ Si	91.877 14	91.857 14
²⁹ Si	4.823 11	4.836 11
³⁰ Si	3.300 8	3.307 8
Relative atomic mass (atomic weight)		
$A_r(\text{Si})$	28.085 40 19	28.085 65 19

¹ Certain commercial equipment, instruments, or materials are identified in this paper to specify adequately the experimental procedure. Such identification does not imply recommendation or endorsement by the National Institute of Standards and Technology, nor does it imply that the materials or equipment identified are necessarily the best available for the purpose.

Similarly, the required chemical preparation techniques of the samples deserve fuller description and critical analysis elsewhere. The atomic-weight measurements here described are in experimental agreement with the previously recognized best silicon measurements by Barnes et al. [4]. It was possible to include a sample from those earlier measurements in the self-same series described above. The consistency of all these measurements was thereby further established.

References

- [1] S. Valkiers, G. Lenaers, and P. De Bièvre, Isotope Abundance Ratio Measurements of Si, CBNM/GE/R/MS/13/89, Internal Report.
- [2] G. Lenaers, T. J. Murphy, S. Valkiers, and P. De Bièvre, Synthetic Si Isotope Mixtures for Absolute Abundance Ratio Measurements, Proc. 37th ASMS Conf. on Mass Spec. and Allied Topics, Miami Beach, FL, p. 422–424, May 1989.
- [3] S. Valkiers, G. Lenaers, and P. De Bièvre, Characterization of Two Silicon Isotope Reference Materials: CBNM IRM-017 and CBNM IRM-018, CBNM/GE/R/MS/11/89, Internal Report.
- [4] I. L. Barnes, L. J. Moore, L. A. Machlan, T. J. Murphy, and W. R. Shields, J. Res. Natl. Bur. Stand. (U.S.) 79A, 727 (1976).

About the authors: S. Valkiers received a degree in chemical engineering in 1976 from Hik University, Geel, Belgium. P. De Bièvre is a PhD from Gent University and also Professor in Isotope Mass Spectrometry at Antwerpen University in addition to his position at CBNM. G. Lenaers received his PhD from Antwerpen University in 1990 with a dissertation on the chemical procedures summarized in this paper. H. S. Peiser, now retired, was at one time Chief of the Crystal Chemistry Section at the National Bureau of Standards (now the National Institute of Standards and Technology).

Letter to the Editor
Slovak Metrological Society

Volume 96

Number 5

September–October 1991

Josef Mandak

Slovak Metrological Society,
Bratislava, CSFR – Czechoslovakia

I should like to bring to the attention of the many readers of the *Journal of Research of the National Institute of Standards and Technology* the establishment of the Slovak Metrological Society (SMS).

SMS came into being on October 16, 1990, as the result of a special founding Congress held in DT Žilina with 137 delegates from the whole of Slovakia in attendance. It brings together individuals involved in both the technical and legal aspects of metrology and its aim is to help in developing metrology and measurement in Slovakia. SMS functions under the direction of the Czechoslovak Metrological Institute (ČSMÚ), the center of Czechoslovak metrology. Together with the Federal Weights and Measures Office (FÚNM), state metrological centers, centers of the calibration service, and production plant metrological centers, it establishes the principal tasks of present-day metrology in the Czechoslovak Federal Republic (CSFR).

The Congress was opened by Dr.-Ing. Weidlich, who presented a paper concerning the aims and tasks of the Slovak Metrological Society. Next on the agenda was the presentation of papers with the titles: "Future Organization of Czechoslovak Metrology and Calibration Service," "Legal Adjustment of Metrology After 1990 and Its Impact upon Users' Organizations," and "Metrology—a Tool for Achieving Quality in Production and Services." These papers were read by Ing. Brezina, director of ČSMÚ and member of the commission IMEKO PC 14, and others.

Attention was principally paid to: looking for ways to cooperate with organizations such as WECC, EUROMET, CEN/CENELEC, and others, as well as how to participate in activities within the framework of ISO and IEC; the unfinished state of the law "On Metrology: Parts I–VI"; different models to achieve quality, how to choose among them, how to demonstrate and document quality as recommended by the 9000 series of ISO quality standards; problems associated with the complex system for educating metrologists in the CSFR; and others.

The papers presented at the Congress together with a listing of the Congress participants are contained in the Congress proceedings titled: Foundation Congress of the Slovak Metrological Society, DT Žilina, 1990.

The Congress developed the rules of the Slovak Metrological Society as well as its activities for the coming 3 years. The emphasis will be on the following: the possibility of bringing together individuals and groups that are active in the field of metrology and measurement, or which show interest in the results of metrology; diffusing knowledge of metrology; protecting, representing, and safeguarding the interests of

metrologists; providing special counseling, consultations, and expert service; cooperating to secure the training of new metrologists; and developing and introducing advanced certificate systems and procedures, especially from the standpoint of their metrological aspects. In summary, the management principles and tasks of the SMS have been established; a committee of 15 members, with Dr.-Ing. Weidlich as its head and a control board of three members, has been elected.

The establishment of SMS will support the growth of metrology in Slovakia, especially as the national economy is transformed into a market economy. The ultimate goal is to incorporate the CSFR into the community of developed countries of Western Europe.

Those interested in cooperation with or further information about the SMS should write to the author at the following address:

Associate Professor Josef Mandak
Slovak Metrological Society,
Tr. L. Novomeského IV/487,
842 55 Bratislava,
Czechoslovakia

Conference Report

SECOND INDUSTRY WORKSHOP ON POLYMER COMPOSITE PROCESSING Gaithersburg, MD May 18, 1990

Report prepared by

S. S. Chang and D. L. Hunston

Polymers Division,
National Institute of Standards and Technology,
Gaithersburg, MD 20899

1. Introduction

The issue of international competitiveness has received much attention lately, and rightly so. One example is a recent Department of Commerce (DOC) study that was conducted to identify emerging technologies since they are critical tools for the development of better, more competitive products in the future. The results, which are detailed in a report [1] entitled "Emerging Technologies—A Survey of Technical and Economic Opportunities," have identified Advanced Materials as one of the key technologies. This same conclusion was reached by a number of other industry and Government sponsored studies including those by the Aerospace Industries Association [2], "Key Technologies for the 1990s" and the Department of Defense [3], "Critical Technology Plan." The Congress's Office of Technology Assessment

(OTA) reports \$2 billion worth of advanced materials are currently replacing conventional materials annually [4] and predicts this will rise to \$20 billion by the year 2000. The OTA study warns, however, that the emphasis on commercialization by Japan and Europe could put them in a very good position to compete for these markets. This warning is echoed by the DOC report which concludes that the United States is rapidly losing its lead in advanced materials.

The largest single item in the advanced material category is polymer based composites. The annual growth rate for polymer composites [5,6] is very high, 16%, but the continuation of this growth requires the expanded use of composites in mass-market, civilian applications. The major barrier to this is the high cost, and this is increasingly a concern for military and aerospace applications as well. A report [7] by Kline & Co. estimated that more than 70% of the cost for advanced composites is in the fabrication and, like a similar report [5] by Business Communications Co., concludes that improvements must be made if the potential of these materials is to be realized. The problem has arisen because the pressure for rapid implementation of composites has led the applications to outstrip the development of a corresponding science and technology base in fabrication. It is now generally recognized that a major effort is needed to correct this problem.

1.1 Purpose of Workshop

The field of composite fabrication is very complex with many potential areas to study, and thus, to be effective, the research activities must be focused on those aspects of the science base which will have the most direct impact on the development of cost effective processing. To identify these

areas, an Industry Workshop on Polymer Composite Processing was held at the National Institute of Standards and Technology on October 7, 1987. The recommendations [8] from that meeting were used in planning a major expansion of the NIST composites program in 1988.

After more than 2 years, it was felt that the recommendations of the 1987 Workshop should be updated and refined so a second Industry Workshop was held at NIST on May 18, 1990. This Workshop also provided an opportunity to tell industry about the progress made by NIST's composites research program since 1987. Of particular interest were the projects designed to address the recommendations of the 1987 meeting. A final objective of the Workshop was to seek industry's advice and guidance for planning an expansion of the NIST effort. Such an expansion would address the scientific and technical questions associated with testing and prediction of performance properties in composites. To examine this area, the Workshop was asked to identify and discuss the performance issues that are most important to their industries. The results and discussions of the second Industry Workshop are summarized in this Report.

1.1.1 Information Sought To accomplish these goals, the attendees were asked to consider the time period from 5 to 15 years from now and answer three questions. First, what are the generic processing methods that will be of most interest to industry during this time period? Second, what are the scientific and technical barriers that hinder the implementation and effective use of these methods? Third, what are the performance issues that are most important for your industry?

1.1.2 Workshop Composition The meeting involved only industrial participants so that the results would reflect the position of industry. There were a total of 26 attendees representing 24 different company organizations. The attendees were asked to indicate which industry sectors they could represent and the breakdown was: 35% aerospace, 21% automotive, 15% electronics, 11% marine/hydrospace, 6% construction, and 12% other which includes prepreg fabrication, industrial applications, general part manufacturing, and database/design management. The attendees were split about evenly among users, suppliers, and those involved in both. The suppliers included manufacturers of resins and fibers as well as starting materials, such as preimpregnated fiber tape and cloth, and fabricators of small parts for the larger industrial users. A full attendance list was given elsewhere [9]. In addition, comments were sup-

plied by scientists from two companies that could not participate in the Workshop but expressed great interest in the NIST research effort.

2. Workshop Program

The Workshop was a day long meeting whose agenda was given elsewhere [9]. It began with a review of the conclusions of the 1987 Workshop, and a brief overview of the NIST's composites research program with emphasis on how it had responded to the 1987 recommendations. This was followed by presentations from representatives of four industry sectors: automotive, electronics, aerospace, and database/design. Each speaker reviewed the current relevance of the conclusions from the 1987 Workshop for their industries and suggested where revisions were needed for the 1990's. Knowledgeable members of the audience augmented the presentation with comments based on their own experience and expertise.

After the industry presentations, a questionnaire was given to each attendee. This questionnaire, which is described below, provided an opportunity for each person to answer the questions posed in the Workshop and furnish other comments as well. While the attendees were completing this form, a more detailed look at the NIST research program was provided with presentations on six processing related projects. This occupied the remainder of the morning and early afternoon schedule. The questionnaires were collected before lunch and the evaluation begun at once so their results would be available for discussions in the afternoon.

During the last part of the meeting, Carl Johnson of Ford led discussions on processing methods, technical barriers, and performance issues. The preliminary results from the questionnaire were used to focus the deliberations. The goal was to reach a consensus among all industry sectors on answers to the three Workshop questions and other issues raised during the discussions. To a large extent, this was achieved although in a few cases, the answers were industry dependent. In addition, the issue of technologies that complement processing produced a large number of new ideas which made it difficult to finalize priorities during the discussions. As a result, a second questionnaire was sent to attendees by mail following the meeting so they could assign priorities to the topics in this area. The Workshop was closed with a summary of the discussions and conclusions by Carl Johnson.

2.1 Review of 1987 Workshop

Industry representatives at the 1987 Workshop were asked to determine the processing methods that would be the most important in the future (5 to 15 years) and the scientific and technical barriers that prevent the optimal use of these methods today. The results are briefly outlined below and in Table 1.

Table 1. Conclusion of 1987 workshop

Most important processing methods (rank)	
Pressure molding	(1)
Transfer molding	(2)
Filament winding	(3)
Thermoforming	(4)
Pultrusion	(5)
Important technologies that complement processing	
Alternate sources of energy	
Resin coating of fibers: Preparation and processing	
Most important scientific and technical barriers (rank)	
Inability to understand and control	
Resin flow—fiber orientation	(1)
Heat flow	(2)
Morphology	(5)
Surface quality—dimensional Tolerances	(6)
Fiber-matrix adhesion	(3)
Data validation—test standardization	(4)
Potentially important materials for the future	
Thermoplastics	
Liquid crystalline polymers	
Molecular composites	

2.1.1 Processing Methods The 1987 Workshop produced a consensus among the industry representatives on five processing methods. In order of decreasing priority they are: pressure molding, transfer molding, filament winding, thermoforming, and pultrusion. Pressure molding included both compression molding and autoclave processing. The first two methods were ranked about evenly and were rated significantly higher than the other three.

2.1.2 Technologies that Complement Processing In addition, two other technologies were identified as very important, but they can not really be classified as processing methods. Consequently, a new category was defined, namely technologies that complement processing. The first of two items in this list was alternate sources of energy input.

This included heating by microwaves, lasers, hot gas jets, and similar techniques which have the potential for highly controlled energy input. The second technology was resin coating of fibers. Powder prepregging, commingled fibers, and similar methods for combining the two constituents in unique ways were included in this item.

2.1.3 Scientific and Technical Barriers In the area of scientific and technical barriers, the Workshop developed a list of six problem areas. Four of them involved the inability to understand and control various processing events: resin flow and fiber orientation (rated first), heat flow (rated second), morphology in partially crystalline systems and in multiphase toughened resins (rated fifth), and surface quality and dimensional stability (rated sixth). These areas are particularly important since they provide the targets for on-line process control which the Workshop regarded as the key to more rapid and reliable processing. The third most important area was fiber-matrix adhesion. It was felt that the measurement techniques for fiber-matrix adhesion needed to be improved while the factors which determine the bond strength must be better understood and controlled during processing. The problem area listed as fourth most important was data validation and test standardization. Of interest here were quality control tests, materials acceptance tests, and performance prediction tests.

2.1.4 Material Systems with Potential for the Future The final topic discussed in the 1987 Workshop was material systems. Although thermosetting resins were felt to be the most important at the present time, the attendees suggested three classes of materials that have great potential for the future and should be closely watched. These are thermoplastics, liquid crystal polymers, and molecular composites.

3. NIST Research Program

Only a brief summary of the NIST composite program will be presented here. Complete details on the program can be found in the Polymer Division's Annual Report [10]. The focus of the program is material science. The program generally uses existing materials, often model systems, and studies the changes that occur during processing. Processing invariably introduces microstructure which influences properties and so a second portion of the program concentrates on developing techniques to characterize this microstructure.

Finally, the properties of the finished test piece are determined. The NIST program generally does not include synthesis of new materials although there are cooperative efforts with universities and industries where the co-participant performs the synthesis. At the other extreme, the performance of large structures is also outside the scope of the NIST effort which usually stops at the level of plates, tubes, or other very simple structures.

The two major program goals are: (1) to monitor, model, and ultimately control the chemical and physical changes that occur during processing in order to develop the tools needed for more rapid and reliable fabrication, and (2) to establish processing-microstructure-property relationships so improved performance and performance prediction can be achieved. As outlined in Table 2, the projects are divided into three tasks: Processing science, Microstructure characterization, and Laminate performance.

Table 2. NIST Composite Research Program

Processing science	
Process monitoring—10 monitoring techniques	
Processing facilities	
Resin transfer molding (RTM)	
Automated press	
Autoclave/prepregger	
Process modelling—RTM	
Computation	
Flow visualization	
Process control	
Microstructure characterization	
Resin	
Thermoset—network structure	
Undeformed state	
Deformed state	
Thermoplastic—crystallinity	
Fiber	
Gel spun fiber—gel structure	
Interface	
Structure of glass/resin interface	
Composite—thick section	
Through thickness variations	
Laminate performance	
Test methods	
Delamination	
Fiber-matrix interface strength	
Modelling	
Delamination	
Buckling in compression	
Failure mechanisms—resin, adhesive, composite	
Crack-tip visualization	
Toughening	
Physical aging	

4. Result and Discussion of Second Workshop

Following the industry overviews, the first questionnaire was distributed, and while attendees filled it out, presentations were made on six NIST projects related to processing science. These presentations will not be described here, but are covered in the Polymer Division's Annual Report [10]. The remainder of the meeting was then directed to a general discussion of the three questions the Workshop was asked to address. The results of the questionnaire formed the basis for the discussions.

4.1 Questionnaire

4.1.1 First Questionnaire The first questionnaire was divided into four sections. The initial page requested information on which industry sector/sectors the attendee could represent. The first section asked each respondent to identify and rank the most important scientific and technical barriers that hinder cost effective processing in their industry. The second section expanded each barrier by listing four to six subtopics so attendees could specify in more detail exactly where they saw the biggest challenges. The third section asked the respondent to identify and to assign priorities on the performance issues that are of most concern to their industry. The final section requested an update on the ranking of items in three categories: processing methods, important technologies that complement processing, and materials with potential for the future.

Each section of the questionnaire contained a list of possible answers based on the results of the 1987 Workshop and suggestions made by the attendees on their meeting registration forms. In addition, space was provided so last minute items could be added, and the attendees took advantage of the opportunity to include several important new topics, particularly in the area of technologies that complement processing.

4.1.2 Second Questionnaire The second questionnaire contained a list of all the suggestions for technologies that complement processing. It was mailed to each Workshop attendee, and they were asked to indicate their priorities and return the list for evaluation.

4.2 Questionnaire Analysis

The results from the questionnaire provide a good representation of the discussion and consensus in the Workshop. The questionnaires were evaluated with a point system. Each attendee was asked to rank in order of importance the answers to each question. Multiple answers could be given the same rank if they were equally important. The first place ranking for each question was given 4 points while the second place received 3 points, the third place 2 points, and the fourth place 1 point. The total points for each answer was then divided by the maximum points possible (i.e., if ranked number one by everybody) and multiplied by 100. This produced a scale which ranged from 100 to 0, where 0 indicated no one ranked the item in their top four. Since the questionnaire contained information on which industry sector the respondent represented, the results could be analyzed for differences between specific industries as well as general trends. The Workshop composition permitted examination of four industries: automotive, electronics, aerospace, and marine. Because the number of respondents in each sector is limited, the industry specific analysis is regarded as qualitative. Nevertheless, the results are quite informative.

4.2.1 Processing Methods The first issue addressed in the discussion was the selection of the most important processing method. A suggestion was made that the category of resin transfer molding be expanded to include related processes such as structural RIM (SRIM). Such fabrication methods are very closely related, share the same problems, and are appropriate to consider together. The term liquid molding was recommended as a more inclusive term. This change was made and is reflected in Table 3 which summarizes the results of the first questionnaire.

Table 3. Processing methods

Method	Score
Pressure molding	84
Liquid molding	82
Filament winding	39
Thermoforming	29
Pultrusion	21

An analysis of the results by industry sector indicates that automotive listed liquid molding as most important method with pressure molding a second.

Electronics listed press molding as the dominate area, but expressed interest in autoclave (pressure molding) and liquid molding as well. Aerospace listed autoclave as first but other methods, particularly liquid molding, were listed quite high. Marine also had a broad range of interests in all methods but listed pressure molding and liquid molding highest.

The general list of priorities is almost identical to that obtained at the last Workshop. Only two changes of any significance were noted. First, there was considerably more interest in fabrication by press under the category of pressure molding. Although led by the electronics industry, other sectors also expressed a stronger interest in this method than they did at the last Workshop. The second difference is the relative importance given to the top two ranked items, pressure molding and liquid molding, relative to the method ranked third. At the last Workshop pressure molding and liquid molding were clear winners, but now the advantage over the third place method is even greater than before. The high ranking given to these two methods reflects the fact that a broad range of industries considers them very important. The increased interest in press molding mentioned above is one example. Moreover, both the aerospace and marine industries expressed interest in a broader range of methods than was the case 2 years ago and liquid molding and press molding receiving much of the increased attention. In the last survey aerospace ranked transfer molding as 10th and liquid molding was not listed at all. This time liquid molding ranked a close second. The potential cost advantages of these methods obviously pays a major role here.

4.2.2 Scientific and Technical Barriers The second item discussed were the scientific and technical barriers to utilization of improved processing methods. The results of questionnaire one are shown in Table 4.

Table 4. Processing barriers

Barriers	Score
Resin flow / fiber orientation	69
Process monitoring and control	52
Fiber-matrix interface	44
Data validation / test standards	33
Morphology understanding and control	28
Surface quality / dimensional tolerance	23
Heat flow	21

An analysis of the results by industry indicates that aerospace rated the first four topics in this order while electronics rated the first two in this order but lists fiber-matrix adhesion, morphology, and surface quality/dimensional tolerance as tied for third. Automotive listed resin flow/fiber orientation as one, surface quality/dimensional tolerance as two, data validation/test standards as three and process monitoring and control as four. Marine listed process monitoring and control as one, fiber-matrix adhesion as two and resin flow/fiber orientation as three.

The results here were very similar to those in the last Workshop including the interest of automotive and electronics in surface quality and dimensional tolerance. There were, however, two important changes. First, heat flow and temperature gradients fell from number two to number seven. One possible explanation for this is that improvements in modeling capabilities have made the prediction of heat flow more accurate and reliable than it was 2 years ago. The second major change was the inclusion of process monitoring and control as a separate item rather than have it included implicitly as was done last time. The reason for this was that the technology had developed to the place where it is now useful to address this topic directly. When listed in this way, every industry sector rated it as either first or second in importance.

An important point mentioned several times during the discussion was the trend toward more complex parts. Current production often involves fabrication of large, three-dimensional components. In addition, there is much interest in thick section composites (25 cm or more) for a number of applications. This increases the need to address the barriers above both because the processing is more complex and the costs associated with failure are far greater.

After an overall ranking of the barriers, the questionnaire asked attendees to explore the importance of specific topics related to each barrier. The results of detailed analysis of these barriers from the second questionnaire and associated discussions during the meeting were given elsewhere [9].

4.2.3 Technologies that Complement Processing The Workshop discussed the technologies that complement processing and identified a number of areas that had not been mentioned either at the previous Workshop or in suggestions offered on the meeting registration forms. Consequently, a second questionnaire which included these new technologies was developed and completed by mail.

For several of the technologies, a number of specific topics were listed, and attendees were invited to indicate if they considered any of these topics to be particularly important. The results of the questionnaire are given in Table 5. For those cases where a number of attendees indicated a high degree of interest in a specific topic for a technology, these topics are also included in Table 5.

Table 5. Technologies that complement processing

Technology	Score
Fiber placement	53
Prepreg preparation	47
Powder prepegging	
Commingled fibers	
Joining	40
Adhesive bonding	
Preform preparation	33
Recycling	23
Environmental safety	21
Tooling	21
Alternate sources of energy	17
Microwave	
Heat assisted fiber placement	

The highest ranked technology is fiber placement. This refers to an advancement on filament winding in which a number of toes are applied simultaneously. Each toe has its own pressure roller that positions and attaches it to the part using either tack (thermosets) or on-line consolidation (thermoplastics). This makes it possible to do complex shapes with concave regions and other desirable features. The individual toes can be cut and stopped or restarted when desired during processing. The result is a very versatile and rapid fabrication process. The second technology is alternate forms of prepreg preparation. This includes a number of new technologies, but the attendees selected powder prepegging and commingled fibers as particularly important. Joining is the technology rated third. Joining can mean thermoplastic welding, adhesive bonding, mechanical fasteners, etc. A number of attendees singled out adhesive bonding as particularly important for the future. The technology ranked fourth was preform preparation which includes trimming, stitching, braiding, etc., as well as automation of these processes. This technology was followed by recycling, environmental safety, and tooling in the list of priorities. The final technology listed was alternate sources of energy. A number of examples were discussed

during the Workshop, but the responses to the questionnaire gave special attention to microwave radiation and heat assisted fiber placement.

Relative to the results in the 1987 Workshop, the major difference is the increased number of technologies with high interest. Only two topics, prepreg preparation and alternate sources of energy, were chosen in 1987. A detailed analysis for specific industry sectors indicates that the top four aerospace priorities were in agreement with this list. The highest rated automotive items differ in that preform fabrication was listed number one and recycling was rated number four instead of prepreg preparation. Electronics ranked prepreg preparation, joining, and alternate sources of energy as top priorities. In the list for marine, preform preparation was not ranked highly while fiber placement, environmental safety and tooling were.

The high ranking given to preform fabrication by the automotive sector was expected although some attendees from this sector rated it rather low. Perhaps, this reflects the difference between those interested in primary structure applications and those involved in sheet molding compound for body panels. A high rating was given to recycling by both automotive and marine, but this was counterbalanced by aerospace where everyone rated this topic quite low. This is understandable in light of the production volumes involved for the different industries.

4.2.4 Materials with Potential for the Future

The Workshop also discussed material systems that have potential for the future and therefore should be watched closely. Everyone agreed that thermosets are very important today and will continue to be widely used in the future. Some attendees felt that thermoplastics (TPs) were also viable candidate materials at present, while others believe the cost effectiveness of TPs is still unproven. There was general agreement, however, that TPs had great potential. Both amorphous and partially crystalline TPs were considered and no distinction was made during the discussions.

In addition to TPs, four other material systems were identified as having great potential. All five are listed in Table 6. The first three were included in the initial questionnaire and the ranking by attendees was equally distributed among them. During the discussions, two additional items were added. These items were also considered as very important so no effort was made to prioritize this list.

Table 6. Materials with potential for the future

Liquid crystal polymers
Thermoplastic polymers
Molecular composites
Smart materials
Specialized polymer systems

The term smart materials was used to designate a variety of material systems which are either active, i.e., piezoelectric, pyroelectric, etc., or contain built-in sensors, i.e., fiber optics, piezoelectric layers, etc. The category of specialized polymer systems includes blends, interpenetrating networks, cyclic oligomers, etc. Such systems have the potential for significantly improved properties relative to simple polymers. The area of molecular composites was also discussed, and it was concluded that they have much potential but cost and processing difficulties present barriers to their use. Finally, liquid crystal polymers were considered, and there was much excitement about their potential to build-in specific properties, i.e., anisotropy generated by controlled molding. The ability to obtain excellent properties in one direction, however, can be compromised if the properties on other directions are poor. A better understanding of these materials and their processing was viewed as the key to realizing their potential.

4.2.5 Performance Properties The final issue addressed by the Workshop was performance properties. The list of possible problem areas included on the questionnaire began with the four topics identified by the Automotive Composites Consortium and then added items known to be of interest to aerospace and electronics as well as topics suggested by attendees on their registration forms. Table 7 shows the results from the questionnaire for the seven topics rated as most important.

Table 7. Performance properties

Property	Score
Impact	61
Environmental effects	57
Delamination	43
Dimensional changes	43
Thermal stability	31
Fatigue	27
Creep	21

A detailed analysis by industry sector shows that automotive listed impact and environmental effects as one and two while thermal stability was third and dimensional stability fourth. Electronics listed environmental effects first with impact and dimensional stability tied for second. Thermal stability tied delamination for fourth. Aerospace listed delamination as first while electronics listed it as fourth. This is the main reason delamination appears so high since others ranked it quite low. Aerospace listed impact as second, environmental effects as third, and dimensional and thermal stability as tied for fourth. Marine listed fatigue and impact as first with creep and environmental effects tied for third.

The results showed impact (which probably includes crash worthiness for automotive) and environmental effects as high priorities for all industry sectors. Beyond that the need depended on the industry. In aerospace the overriding concern was delamination; in electronics it was dimensional stability, and in marine, it was fatigue. There was also concern in a number of industries about creep, particularly for applications using thermoplastics, and thermal stability in applications where dimensional stability (thermal expansion) or high temperature are important. The discussion suggested, however, that these differences between industries may become less important as time passes. For example, the reason fatigue was not ranked higher in automotive and aerospace is that the designs are now dominated by crash worthiness and delamination. Once these problems are solved, fatigue may become an important concern. The discussion also emphasized the importance of processing in determining the microstructure that controls performance. The lack of understanding in this area was considered an important problem.

5. Conclusions

Two processing methods were selected as by far the most important fabrication techniques for the future: pressure molding and liquid molding. Pressure molding was defined to include flat bed press molding, compression molding, and autoclave molding. The term liquid molding was used to describe resin transfer molding (RTM) and structural reaction injection molding (high speed RTM).

The marine industry expressed a broad range of interests, while automotive's primary focus is liquid molding, aerospace's is autoclave molding, and electronic's is press molding. Surprisingly, however,

all industry sectors expressed interest in a variety of pressure and liquid molding techniques.

Three additional processing methods were identified as being important for the future: filament winding, thermoforming, and pultrusion.

Seven scientific and technical barriers to the full exploitation of the processing methods outlined above were identified. The highest priority was the need to understand and control resin flow and fiber orientation. The importance of resin flow was associated with the problems of void formation, mold filling, and edge and corner flows. In connection with fibers, the major concerns were fiber wetting, fiber alignment, and orientation control.

The second highest priority barrier was the need for process monitoring sensors for on-line process control. This included the development of new techniques and the improvement of existing methods. Current sensors and electronics need to be made more rugged to operate effectively on the factory floor, and the output of the sensors must be better understood and more closely linked to process control.

The third highest ranked barrier was the need to understand and control the fiber-matrix interface. Of particular concern is the area of test methods where current techniques are difficult to use and interpret, or not developed to the point where clear correlations with composite properties exists. Another area where it was felt that more understanding was needed was surface treatment.

Data validation and testing standards was another area that needed more study. Measurements related to performance were a particular concern, but quality control testing was also of great interest. Measurement of viscosity and degree of cure were particularly important here since the focus was processing.

The inability to determine the optimum morphology and achieve it during processing was another area of great concern. All industry sectors felt this was important since morphology often plays a significant role in toughness. The aerospace and automotive industries also expressed a concern about the control of crystallinity in partially crystalline thermoplastics.

The sixth most important barrier was the inability to adequately control surface quality and dimensional stability. Although all industry sectors had concerns in this area, automotive and electronics rated this area as second and tied for third respectively in their priority lists.

The final barrier selected was heat flow. This area was second on the priority list generated at

the 1987 Workshop. This change may be due to the improvements that have occurred during the past several years that now make modelling of heat flow easier and more accurate.

The Workshop also identified and assigned priorities to eight technologies that complement processing and are important for the future. The two highest ranked items were fiber placement and new methods to prepare prepreg, i.e., powder prepregging, commingled fibers, etc. Joining was listed as third, and although both adhesive bonding and mechanical fasteners were mentioned, the former received by far the most attention. Preform preparation was listed next primarily on the strength of the number one ranking given by automotive. Recycling, environmental safety and tooling were listed next in that order. As might be expected, the greatest interest in these topics was for mass production markets, i.e., automotive and marine. Alternate sources of energy, which includes microwave heating, heat assisted fiber placement, etc., was ranked eighth but had several strong supporters in electronics and marine.

The majority of people at the Workshop felt that thermosets were still the dominant resin system in their applications. A number of attendees, however, were actively engaged in thermoplastic development and everyone felt these materials had great potential for the future if their cost effectiveness could be established. Thermoplastics were therefore classified as a material to be watched closely for future development. Four other classes of materials were also included on this list: liquid crystal polymers, molecular composites, smart materials, and specialized polymer system. Smart materials include systems with either built-in sensors or active components such as piezoelectric layers. Specialized systems include blends, interpenetrating networks, cyclic oligomers, etc. The last two categories were not on the this list at the Workshop 3 years ago and represent new technologies. In addition, the interest in liquid crystal polymers was somewhat greater than it was 3 years ago.

The Workshop also selected seven performance issues that they felt were critical to the future use of composite materials. In order of priority they are: impact, environmental attack, delamination, dimensional changes, thermal stability, fatigue, and creep. For the highest ranked topics there was a surprising consensus with all industry sectors ranking impact and environmental attack in their top three items. For automotive impact included crash worthiness. Beyond this point, the priorities differed for each industry. Aerospace listed

delamination as their highest priority and dimensional changes as fourth. Automotive added thermal stability and dimensional changes as third and fourth. Electronics was similar to automotive with slight differences in ordering. Marine listed fatigue and impact as first with creep and environmental attack as tied for third. The differences generally reflect one or two overriding concerns for the particular application, for example, delamination in aerospace. As these concerns are successfully addressed, other problem areas will become more important, i.e., fatigue will become more of a concern to aerospace if and when the delamination problem is solved.

6. References

- [1] Emerging Technologies—A Survey of Technical and Economic Opportunities, U.S. Department of Commerce (1990).
- [2] Aerospace Industries Association, Key Technologies for the 1990s, 1988; and Key Technologies for the 1990s Targeted, Chem. Eng. News 66 (1), 18 (1988).
- [3] Technologies Vital to U.S. Defense Selected, Chem. Eng. News 67 (14), 24-25 (1989).
- [4] Naj, A., U.S. Loses Edge in Composite Materials, Wall Street Journal, December 26, 1989.
- [5] Study sees High-Volume Advanced Composites Use in 1990s, Advanced Composites 3 (5), 18-20, September/October (1988).
- [6] McDermott, J., Assessing the Advanced Composites Market, Advanced Composites 3 (2), 47-52, March/April (1988).
- [7] Fabrication 70 percent of Cost for Advanced Composites, Advanced Composites 3 (4), 12 July/August (1988).
- [8] P. Beardmore, and D. Hunston, Polymer Composite Processing, an Industry Workshop, NBSIR 87-3686, National Bureau of Standards (U.S.), Gaithersburg, MD, February, 1988.
- [9] C. Johnson, S. S. Chang, and D. Hunston, Polymer Composite Processing 2nd Industry Workshop, NISTIR 4461 (1990).
- [10] Polymers: Technical Activities 1989, Polymers Division, National Institute of Standards and Technology, NISTIR 89-4150 (1990).

change implications that determine how quickly and smoothly an organization can begin to achieve the benefits of CASE and methodology.

“The impact of implementing a new information architecture.” Ron Shelby of Connecticut Mutual highlighted the role of information-driven planning, analysis, and system development techniques in organizations which use information technology to cut costs, improve client services, and react to changes in their environment. He discussed the impact of implementing an information architecture which shares data upon work process and structure.

Fred L. Forman of American Management Systems presented a fable which described what happened when data planning became an end unto itself in Dataland. Data modelers sometimes spend years without adding business value to their organization. But that could change with little or no warning. Be prepared!

“Data modeling from the data administration viewpoint,” by Joseph H. Oates of Life Cycle Technology. A data sharing environment raises many issues that have not been a concern to application developers in the past. Data administrators follow a much more rigorous set of rules in developing a global data model than is required for the data models of systems which do not share data.

“Data management and information proficiency: a vision for the future,” by Thomas J. Buckholtz of the General Services Administration. Information proficiency is the effective use of information to accomplish an individual’s job and an agency’s mission. Essential to this process is the successful management of data to maximize accessibility, accuracy, consistency, relevance, and strategic use. Vision, technology, people, organizations, and tools are critical elements in the equation of effective data management.

“Information reengineering,” presented by William R. Durell of Data Administration, Inc. Unfortunately, most data reengineering efforts result in minor or cosmetic improvements to data quality. Cosmetic, moderate, and reconstructive (severe) methods may be applied by resorting to a variety of strategies. A set of risks and benefits attends each method.

Graham W. Thompson of Manager Software Products discussed “Managing information across multiple CASE tools.” The open tool architecture concept within AD/Cycle calls for the sharing of information via the repository between your organization’s tools of today and tomorrow. He

addressed the practicality of this vision and the steps that individual organizations and the industry as a whole must take to make this concept a reality.

“Implementing data architecture,” by William H. Inmon. Five years ago, data architecture was an interesting idea. Three years ago, there were perhaps five companies in the process of implementing an architected approach to data. Today, there are many companies either in the process of completing their first thrusts into data architecture or actually using their first implementation. Some success stories and lessons learned along the way were presented.

“Data Management and customer satisfaction.” Karen Lindsay of Blue Cross and Blue Shield of Georgia discussed the importance of customer satisfaction in the corporate culture. Business success can be achieved through refocusing on working with customers versus around them. Data professionals must monitor performance and continually be working to improve the process which will allow data administration and customers to achieve long-term goals and avoid short-term frustrations.

“Data administration, the IBM repository, and CASE technology at Depository Trust Company.” Emmanuel Ackerman presented his views on the state of the IBM repository in the short and long term, the DTC’s experience working with it, and the steps being taken to position for future releases. The most important step has been an effort to implement an application development methodology and Knowledgeware’s Information Engineering Workbench (IEW/ADW).

“Status and application of standards for data administration,” Bruce K. Rosen, Computer Systems Laboratory, NIST. There are many data processing related standards in the world today. Sorting through these standards and applying them is often a difficult task, complicated by a lack of knowledge about the current status of different standards. Identification and proper application of data administration related standards is essential.

“The need for future vision in a data management program.” Reed Phillips of the Department of Commerce presented examples of future vision in the public and private sectors as representative of global vision statements that are indicative of problems and issues in their respective communities. He discussed data management as it relates to major Department of Commerce missions, together with vision statements that reflect individual bureau and department-wide perspectives.

Conference Report

DATA ADMINISTRATION MANAGEMENT ASSOCIATION SYMPOSIUM Gaithersburg, MD May 14–15, 1991

Report prepared by

Judith Newton

Information Systems Engineering,
Computer Systems Laboratory,
National Institute of Standards and Technology,
Gaithersburg, MD 20899

1. Introduction

Data administration has evolved from the need for improved planning and management of information into a resource recognized today by successful organizations as a strategic value. A primary goal of data administration is to improve the planning, organization, and management of data resources. Achieving this goal requires a clear vision for the future.

Limited resources, shifting priorities, and evolving technologies are just a few of the constraints that must be faced as data administrators attempt to translate the vision for improved data management into a reality.

The Data Administration Management Association (DAMA) is the professional organization for Data Administrators. An international board over-

sees a loose federation of local chapters in the United States and Australia. The National Capital Region Chapter (NCR DAMA) has monthly meetings from September through April, as well as a Symposium in May.

NCR DAMA held its fourth annual Symposium at NIST on May 14-15, 1991. The theme this year was "Managing Data—From Vision to Reality." Attended by 225 Federal and private industry data administrators, the Symposium was cosponsored by NIST and NCR DAMA.

This year's Symposium continued the tradition, begun with the 1990 event, of distributing the program over 2 days. However, instead of concurrent sessions, the planning committee decided on a straightforward format. In addition to the speakers, awards were presented and a report on the progress of the DAMA Working Group on Standards and Procedures was given.

2. Speakers

The key topics covered by the speakers included: "Achieving the data management reality." Arnold Barnett of Barnett Data Systems described the goals of data management, the factors which limit achievement, and the planning activities needed to accomplish the goals. One must ascertain the problems to be solved, develop a realistic plan, obtain approval to proceed, and execute the plan by building the necessary infrastructure.

"The road map for CASE implementation," by Ian Palmer of James Martin Associates, Inc. The road map provides a variety of pathways, but generally begins with the careful selection of a pathfinder project and leads through the planned fan-out of CASE workstations backed by the necessary infrastructure development and organizational adjustments. It explicitly recognizes the cultural

3. Working Group Report

The Working Group on Standards and Procedures has been meeting monthly during the past year. It has produced a draft Model Data Administration Standards Manual, which was distributed for comment. This document, when in final form, will be circulated as a guide to the administration of information standards and the procedures for implementation. The group plans to resume monthly meetings in the fall.

4. Proceedings

The proceedings of this Symposium will be released as a NIST publication. The Proceedings of the First¹ and Second² Annual DAMA Symposia were published by NIST and copies are still available. The Fifth Annual Symposium will be held at NIST May 12-13, 1992.

¹Judith J. Newton and Frankie E. Spielman, eds., *Data Administration: Management and Practice*, Proceedings of the First DAMA Symposium, NIST Special Publication 500-159, National Institute of Standards and Technology, Gaithersburg, MD, October 1988.

²Judith J. Newton and Frankie E. Spielman, eds., *Data Administration: Standards and Techniques*, Proceedings of the Second Annual DAMA Symposium, NISTIR 90-4292, National Institute of Standards and Technology, Gaithersburg, MD, April 1990.

News Briefs

General Developments

Inquiries about News Briefs, where no contact person is identified, should be referred to the Managing Editor, Journal of Research, National Institute of Standards and Technology, Administration Building, A635, Gaithersburg, MD 20899; telephone: 301/975-3572.

NIST HELPING IN SEARCH FOR A MORE FIRE-SAFE CIGARETTE

As part of a team of experts from government, industry, and public health and safety organizations, researchers from NIST are working to help reduce the losses from fires started by cigarettes. The work is being done under the Fire Safe Cigarette Act of 1990 with funding from the U.S. Consumer Product Safety Commission. According to the National Fire Protection Agency, each year cigarettes start more than 230,000 fires and cause more than 1,600 deaths, 4,300 serious injuries, and \$443 million of property damage. NIST researchers will develop a standard test method that can be used to measure how likely a cigarette is to ignite soft furnishings, such as mattresses. The researchers also will use their expertise in computer modeling to learn more about the physics of ignition and to build a user-friendly model to predict ignition propensity. The project will be completed in August 1993. In an earlier, related study, NIST tested thousands of commercial and experimental cigarettes and identified changes that could significantly reduce the chance of igniting soft furnishings.

SCIENTISTS TRACK POLLUTANTS WITH RARE ISOTOPE TAGS

From the Blue Ridge Mountains to the Grand Canyon, visibility-reducing haze is clouding views in our national parks. Many are quick to blame coal-fired power plant emissions as the main cause

of this problem. Researchers now can use a technique developed cooperatively by NIST and the University of Maryland to evaluate how power plant emissions affect air quality up to hundreds of miles away from the source. Scientists spike power plant emissions with rare-earth elements, such as neodymium or samarium, that have an isotopic abundance different from that occurring in nature. These tags attach to fly ash particles and can be collected downwind from the power plant. Laboratory analysis can confirm whether the particles actually came from the suspect power plant. The tags tell scientists not only where the particles originate but also how concentrated they are. The July 1 issue of *Analytical Chemistry* describes this work in greater detail.

FIRST LABS ACCREDITED FOR GOSIP CONFORMANCE TESTING

NIST has announced the first laboratories to be accredited to test Open Systems Interconnection (OSI) products for conformance to the U.S. Government OSI Profile (GOSIP). GOSIP, issued as Federal Information Processing Standard (FIPS) 146, defines a set of data communications rules called "protocols," which enable computer systems developed by different vendors to communicate and the users of different applications on these systems to exchange information. The National Voluntary Laboratory Accreditation Program (NVLAP), administered by NIST, accredited the laboratories in the field of computer communications software. The use of NVLAP-accredited laboratories is required by the U.S. GOSIP Testing Program for testing products for conformance to GOSIP. Laboratories are accredited for 1 year, and accreditation is renewable annually. For information on NVLAP, contact Jeffrey Horlick, A124 Building 411, NIST, Gaithersburg, MD 20899, 301/975-4020. For information on the U.S. GOSIP Testing Program,

contact Jean-Philippe Favreau, B141 Technology Building, NIST, Gaithersburg, MD 20899, 301/975-3634.

1991 ANNUAL DIRECTORY OF ACCREDITED LABS AVAILABLE

Manufacturers, exporters, builders, and procurement and regulatory officials will want a copy of 1991 Directory of Accredited Laboratories (SP 810). The directory lists more than 1,000 domestic and foreign laboratories accredited by the NIST National Voluntary Laboratory Accreditation Program (NVLAP) for specific test methods as of July 1, 1991. Current fields of testing: acoustics, asbestos fiber analysis, carpet, commercial products (paint, paper, plastics, and seals and sealants), computer applications, construction materials, electromagnetic compatibility and telecommunications, personnel radiation dosimetry, solid fuel room heaters, and thermal insulation. The labs are listed alphabetically, by field of testing, and by state. Send a self-addressed mailing label to NVLAP, A124 Building 411, NIST, Gaithersburg, MD 20899, 301/975-4016, fax: 301/975-3839.

GETTING MORE X-RAY DIAGNOSTIC POWER

Researchers from NIST and industry have begun a cooperative research and development agreement to support the development of new x-ray instruments for industrial and medical applications. NIST will help test patented prototypes of a new computerized tomography (CT) x-ray scanner and an enhanced-power x-ray tube. Based on a novel design using Compton-scattered x rays, the scanner will be part of a portable CT system that is cheaper and more versatile than current models. The new tube is anticipated to be more than twice as powerful as current tubes, offering longer tube life and higher throughput for both medical and industrial applications. "The radiation measurement facilities at NIST are unique and have the flexibility we need, and we also benefit from the NIST expertise in radiation measurement and source characterization," according to an industry representative.

REPORT ON U.S./U.S.S.R. STANDARDS WORKING GROUP

The aim of the Standards Working Group (SWG) of the Joint U.S./U.S.S.R. Commercial Commission is to explore mutually advantageous avenues of cooperation, including promotion of international standards and product acceptance criteria. SWG, established in September 1990 by the U.S.

Commerce Department and the U.S.S.R. Ministry of Foreign Economic Relations, is co-chaired by NIST and Gosstandart. Emphasis at the first meeting in the United States was placed on exchanging information on standards and conformity assessment in both countries. First Meeting of the Standards Working Group of the Joint U.S./U.S.S.R. Commercial Commission, March 11-13, 1991 (NISTIR 4572) contains presentations by government officials and private-sector standards developers to provide Soviet members insight into U.S. standardization activities. Also included are materials submitted by the Soviets on legislative initiatives under development. Available from the National Technical Information Service, Springfield, VA 22161. Order by PB #91-194498 prepaid for \$34, foreign \$66.

CHEMICAL "DATING GAME" PINPOINTS AIR EMISSIONS

When scientists probe an air sample to determine what contaminants are present, they often face a dilemma: Where do these impurities come from? NIST is helping to answer this by refining a technique best known for pinpointing the age of archaeological objects. Called radiocarbon dating, the method compares the abundance of carbon-14 (C-14) in the sample to that of carbon-12. C-14 is naturally distributed throughout living matter, but when an organism dies, its C-14 level gradually decreases. This "yardstick" allows scientists to separate "living" carbon sources (burning wood, for example) from "dead" ones (fossil fuels such as gasoline). Recently, NIST helped the Environmental Protection Agency (EPA) sort winter pollution sources in Boise, Idaho, a city chosen for its auto emissions and many residential woodstoves. NIST researchers found that two collection sites in Boise showed high concentrations of wood-related pollution, as much as 80 percent. They are now analyzing this data for definitive conclusions and are helping the EPA conduct a similar study in Roanoke, VA.

DIRECTORY OF STATE/LOCAL LAB PROGRAMS PUBLISHED

Directory of State and Local Government Laboratory Accreditation/Designation Programs (SP 815) will help construction, building, environmental, and health and safety officials locate various state and local laboratory accreditation and similar programs. The directory is a guide to 21 state systems and 11 municipal programs across the country designated by government agencies to carry out

their responsibilities for testing products and services. Entries include information on how the laboratories are assessed. Part of a series to provide industry with information on standards-related endeavors, the directory is available by sending a self-addressed mailing label to Standards Code and Information Program, A633 Administration Building, NIST, Gaithersburg, MD 20899, 301/975-4031. A list of other standards-related and conformity assessment directories also is available.

VALIDATED PROCESSOR LIST NOW DISTRIBUTED BY NTIS

The Validated Processor List (VPL) identifies COBOL, FORTRAN, Ada, and PASCAL programming language processors that have been validated for conformance to Federal Information Processing Standards (FIPS). The List also identifies SQL (structured query language) processors that have a registered test report and references the applicable FIPS. The List includes, for the first time, GOSIP conformance testing registers as well as POSIX conformance testing laboratories and validated products. The VPL will be distributed as a standing order for \$68 annually by the National Technical Information Service, Springfield, VA 22161. Order by PB#91-937301/AS. Comments or questions on VPL should be addressed to Judy B. Kailey at NIST on 301/975-3274.

NIST SIGNS CRADA ON NETWORK MANAGEMENT

NIST has signed a cooperative research and development agreement (CRADA) with a private company to work on improving understanding of the role and effectiveness of integrated network management systems. Projects involve experimenting and monitoring key network management functions within Integrated Services Digital Network (ISDN) and local area network environments. The CRADA also covers experimentation with network management tools for exchanging and defining management information. Under the agreement, the private company and NIST will develop a proof-of-concept integrated network management system based on the NYNEX Allink Operations Coordinator and the Logica Data Architects C3 commercial products. For information, contact Patricia N. Edfors, Computer Systems Laboratory, B154 Technology Building, NIST, Gaithersburg, MD 20899, 301/975-3758.

PROPERTIES OF MATERIALS PROGRAM EXPLAINED

NIST has an active electromagnetic properties of materials program to meet the needs of the electronics and microwave industries. These companies require accurate information on dielectric and magnetic materials used in printed circuit boards, capacitors, microwave components, sensor windows and radomes, for example. Improved characterization of these materials permits closer tolerances and leads to cost savings for designers and manufacturers of electronics and microwave products that use these materials. NIST aims to develop or improve measurement methods, reference materials, and a database on commonly used materials. NIST also participates in national and international intercomparison. Paper No. 22-91 explains the program and is available from Jo Emery, Div. 104, NIST, Boulder, CO 80303, 303/497-3237. Technical information is available from Claude M. Weil, Div. 813.02, NIST, Boulder, CO 80303, 303/497-5350.

SEARCHING FOR BRAKES AND ACCELERATORS IN CANCER

Scientists are sorting out subtle, but critical differences between treated and non-treated cancer cells with a new way of evaluating chemotherapy drugs. In research at NIST, the system reveals the appearance and disappearance of certain cellular proteins following treatment with interferon or tumor necrosis factor. Some of the changes occur in oncogene and suppressor gene products, the proteins which accelerate or brake the progression of cancer. The system could be used to identify protein changes for any number of chemotherapeutic agents, says a NIST biologist. The ability to identify how proteins respond to specific drugs could one day allow doctors to tailor a patient's treatment according to the sub-cellular traits of his or her tumor. The NIST scientist and his collaborators at the John Wayne Cancer Institute hope to define the basic mechanism chemotherapeutic agents use when they spring into action against a cancer cell.

NEW GUIDE CAN HELP BETTER DESIGN VAVs

A building air-delivery system known as variable air volume, or VAV, can save energy dollars by delivering just the right amount of air to areas that need it. However if a VAV is poorly designed or

improperly operated, problems can develop such as poor air circulation, noise, inadequate amounts of outdoor air, or too much hot or cold air. Researchers from NIST inspected VAV systems in numerous GSA buildings and conducted tests in three of them. The results were incorporated in a guide to the design, control and commissioning of VAV systems. The guide also includes "check lists" to help design a new VAV system or alter an existing one. While the guide was developed for GSA, it should be widely useful in the design community. Variable Air Volume System Design Guide (NISTIR 4605) is available from the National Technical Information Service, Springfield, VA 22161 for \$15 prepaid. Order by PB 91-216655/AS.

NEW PUBLICATION ISSUED ON TRANSPARENT FILE ACCESS

A new publication, Issues in Transparent File Access (NIST Special Publication 500-186), will assist managers, programmers, and users in government and industry in understanding, evaluating, managing, and using the Transparent File Access (TFA) Standard (IEEE 1003.1-1990) and system to access remote file systems. Transparent file access means remote files are accessed as though they were local. The report discusses the semantic, performance, and environmental issues met during the development of the TFA standard. The 86-page report illustrates some issues with examples and demonstrations using NFS (Network File System), the most widely used implementation for accessing remote files on a network. The publication is for sale by the National Technical Information Service, U.S. Department of Commerce, 5285 Port Royal Road, Springfield, VA 22161. Order by PB-91187831. The price is \$4.75.

UPDATE PLANNED FOR CATALOG OF CODE SETS

Users of the Catalog of Widely Used Code Sets, Federal Information Processing Standard (FIPS) 19-1, are asked to help locate organizations maintaining code sets that should be included in a planned revision. The catalog lists and describes code sets—social security numbers, zip codes, and the airport destination on luggage tags, for example—and offers users a central source for selecting needed code sets. Candidate code sets include international, national, or federal standards; those which apply throughout an industry;

or those which have a significant number of users. If your organization maintains code sets or you know of others that do, please contact Elizabeth Lennon at 301/975-2832 for submission procedures. Copies of FIPS 19-1 are available from the National Technical Information Service, U.S. Dept. of Commerce, 5285 Port Royal Road, Springfield, VA 22161; (703) 487-4650. Order number is FIPSPUB19-1 and price is \$17.00.

PYRITE ORE STANDARD AVAILABLE FOR BIOPROCESSORS

Ore producers that use microorganisms to process minerals can obtain a new reference material for determining the rate of biological attack on pyrite and as a bioleaching substrate. Reference Material (RM) 8455, Pyrite Ore for Bioleaching Studies, provides assurance to users in different laboratories that they are investigating the same material. The rate of bioleaching of iron by the microorganisms, *Thiobacillus ferrooxidans*, which attack pyrite, is 12.4 ± 4.0 mg of iron per L per h and reported for information only and not certified. The rate was determined by NIST and eight cooperating laboratories in accordance with ASTM Test Method 1357-90. RM 8455 is available for \$80 in 100 g bottles in vacuum-sealed foil pouches from the Standard Reference Materials Program, Room 204 Building 202, NIST, Gaithersburg, MD 20899, 301/975-6776, fax: 301/948-3730.

ON-LINE TECHNOLOGY HELP FOR SMALL BUSINESSES

In cooperation with the Small Business Administration (SBA), NIST has awarded six grants to establish pilot programs to give small businesses improved access to public and private technology, services, and expertise. Matching fund grants of \$200,000 will go to state Small Business Development Centers (SBDCs) in Missouri, Oregon, Pennsylvania, Texas, and Wisconsin. The Maryland SBDC, which is planning a more limited program, will receive a \$50,400 grant. The grants are for 1 year and may be renewed for an additional 2 years, depending on available funds. They are part of an SBA effort to demonstrate to small businesses the value of increased access to commercial, on-line data services and technical information services. NIST manages the program for the SBA as part of its responsibility to foster the transfer of appropriate technology to small and medium-sized businesses.

EIGHT STATES TO RECEIVE TECH TRANSFER PLANNING GRANTS

NIST has chosen eight states to receive matching fund grants to help create plans for new, statewide programs to coordinate existing state and federal technology extension services. As part of the NIST State Technology Extension Program, grants will go to Arkansas (\$23,250), Florida (\$78,200), Massachusetts (\$70,003), Mississippi (\$99,648), Montana (\$50,000), Oklahoma (\$98,010), Oregon (\$82,481), and Texas (\$98,843). The coordination programs should ease the access of small and medium-sized businesses to a variety of services that seek to improve competitiveness through the application of science and technology.

HOW TO USE DIAMOND TURNING WITH "IMPOSSIBLE" METALS

Researchers at NIST and Los Alamos National Laboratory have demonstrated the unheard-of feat of machining near-optical-quality surfaces on significant areas of stainless steel using diamond turning. Diamond-turning machines increasingly are used in manufacturing optical components used in such things as compact disk readers, bar code scanners, and other applications requiring complex shapes, but only certain materials have been considered suitable for diamond-turning. Potentially useful materials such as stainless steel, titanium, and molybdenum have been impossible to work with because the diamond-cutting tool degrades and breaks down too quickly. The new technique uses a specially modified machine with both the tool and workpiece cooled to cryogenic temperatures, suppressing chemical reactions between the steel and the diamond tool that play a major role in the degradation of the tool.

RESEARCHER CRACKS CHEMICAL MYSTERIES OF COAL

Scientists know that high temperature and pressure slowly convert decaying plants into coal, but the exact chemical mechanisms remain somewhat of a mystery. A NIST chemist has discovered clues to this mystery through studies on the thermal chemical properties of coal. He recently found a weak chemical bond that triggers coal formation, and also is studying the black, sooty byproducts of coal combustion, known as polycyclic aromatic hydrocarbons. He has found ways to predict chemical reactions for these large, complex molecules. The

chemist's research is providing information that may help energy producers find more economic and less polluting ways of converting coal into oil or natural gas. For his contributions to coal chemistry, he will receive the 1992 American Chemical Society's Henry H. Storch Award in Fuel Chemistry.

PROPOSED DIGITAL SIGNATURE STANDARD PUBLISHED

As the federal agency responsible for developing standards to assure privacy of unclassified information in federal computer systems, NIST published its proposal for a Digital Signature Standard (DSS) in the Aug. 30 Federal Register. The DSS will allow federal agencies to verify the integrity of electronic data and the sender's identity. The government has filed for a U.S. patent on this technique and plans to seek foreign patents. NIST seeks comments by Nov. 29 on the proposal from the public, industry, and federal, state and local government users. After considering the comments, NIST will submit the proposed standard to the Commerce Secretary for review and approval. Technical questions should be referred to Miles Smid, 301/975-2938.

HIGH-INTEGRITY SOFTWARE LECTURE SERIES RESUMES

Increasing reliance on computers—for example, in medical devices, automobile components, and robots in manufacturing—requires assurance that these systems will operate reliably and exactly as intended, even when other systems fail. NIST's lecture series on high-integrity systems resumed in early October with a talk by Laszlo A. Belady entitled "The Engineering of Software for High Integrity." The series focuses on problems and potential solutions in building and operating high integrity systems. Scheduled speakers will address management processes (life cycle methodology, risk management, costing), development processes (formal methods, object-oriented design), and assurance processes (software reliability, clean-room techniques, formal verification). The lecture series, open to the public free of charge, serves to alert federal and industry managers, technical staff, and users about issues they must face in managing valuable information resources. For information, contact Dolores Wallace, 301/975-3340.

ANTENNA MEASUREMENT SERVICES IMPROVED

Responding to requests from industry and other government agencies, NIST has expanded its antenna measurement services above 30 GHz. The swept frequency gain measurement service now includes the 33–50 GHz band and covers 1–50 GHz with gain values with an accuracy of ± 0.3 dB or better for this frequency range. In addition, NIST has the capability to measure fixed frequency gain and polarization for 33–65 GHz and to measure antenna patterns for 33–50 GHz. Researchers currently are working to increase the swept frequency gain service to 65 GHz; this should be available in about a year. Paper No. 36-91 outlines the high-frequency antenna measurement services and is available from Jo Emery, Div. 104, NIST, Boulder, CO 80303, 303/497-3237. For technical information, contact Michael H. Francis, Div. 813.05, NIST, Boulder, CO 80303, 303/497-5873.

NEW "USERS' GUIDE" TO NIST AVAILABLE

NIST has issued a new, comprehensive guide to the Institute's many research opportunities, facilities, and services. The guide summarizes major NIST research programs that could be the basis for cooperative research and development agreements with industry; describes the major specialized research facilities at NIST available for industrial use—several of which are unique in North America or the world; and lists services to industry offered by the Institute. Detailed descriptions, project managers, and phone numbers are given for each item. Copies of Research. Services. Facilities. are available with a self-addressed mailing label from the NIST Public Affairs Division, A903 Administration Building, NIST, Gaithersburg, MD 20899, fax: 301/926-1630.

ION MICROSCOPE HELPS MAP ATOMS IN AEROSPACE ALLOYS

NIST chemists have mapped the arrangement of lithium atoms on a speck of metal alloy approximately the width of a human hair. Lithium composition maps offer the aerospace industry an inside look at the strengths and weaknesses of alloys that may be used to manufacture the next generation of airplanes. Using the ion microscope, NIST collaborated with Lehigh University to study enrichments and depletion of lithium within an aluminum-lithium alloy. The data they collected also enabled the scientists to calculate how quickly lithium atoms diffuse through the aluminum alloy. Adding

small amounts of lithium to aluminum makes an alloy that's stronger and lighter than pure aluminum. The problem is that the high temperatures necessary for alloy processing tend to drive lithium out and weaken the alloy. Information from lithium composition maps could help the aerospace industry overcome this problem and develop effective thermal processing techniques for advanced alloys.

NIST, INDUSTRY TO PROPOSE COATINGS CONSORTIUM

A committee from NIST and industry will propose a coatings technology consortium at a workshop Dec. 3-4 at NIST in Gaithersburg, MD. Last May, NIST explored the idea of a consortium to find a new way to detect flaws on painted metal products in a production line. After discussions with manufacturers of coatings and coating equipment, automobiles, appliances, and roll-coated metal, that idea has been broadened. The proposed consortium would develop critical technologies needed to control the entire coatings process—including inspecting raw materials, controlling the application process, and evaluating the finished product. These technologies might include hardware and software for machine vision, high-speed vision processing for real-time inspection, and devices to measure the thickness of a coating. NIST has organized and managed several industry-government consortia. For information or to register for the workshop, contact Jonathan Martin at 301/975-6717 or Theodore Vorburger at 301/975-3493.

POLYMER COMPOSITES PROCESSING SENSORS IDENTIFIED

The driving force for process control sensors is the need by the U.S. polymer composites industry to improve the efficiency and reliability of fabrication to increase competitiveness. The most promising on-line sensor techniques are ultrasonic, dielectric, spectroscopic, and optical. NIST researchers identified and analyzed these process control methods in a report, *Assessment of the State-of-the-Art for Monitoring Sensors for Polymer Composites* (NISTIR 4514). While each sensor has its own research and developmental requirements, the most important technical and scientific issues are common to all methods. Major short-term needs are to build more rugged and reliable equipment that can withstand the harsh manufacturing environment and to develop better relationships between sensor data and information needed for process control. For a copy of the report, send a

self-addressed mailing label to Donald L. Hunston, A209 Polymer Building, NIST, Gaithersburg, MD 20899, 301/975-6837.

NIST UPDATES TIME SERVICES PUBLICATION

Precise time and frequency information is needed by electronic instrument and equipment manufacturers, electrical power companies, radio and TV stations, telephone companies, and air traffic controllers, to name a few. NIST has provided this information since its first shortwave radio station, WWV, went on the air in 1923. That station still operates but the range of services has been expanded. NIST Time and Frequency Services (SP 432) provides an updated summary of shortwave and low-frequency radio broadcast services, the broadcast formats for WWV, WWVB and WWVH, GOES satellite time services, the NIST frequency measurement service, and the automated computer time service. Available from the Superintendent of Documents, U.S. Government Printing Office, Washington, DC 20402. Order by stock No. 003-003-03084-8 for \$2 prepaid.

OSI ROUTER INTEROPERABILITY TESTING PERFORMED

As part of a research program to advance OSI routing technology, NIST has performed interoperability tests on equipment using the Open Systems Interconnection (OSI) Intermediate System to Intermediate System Intra-domain Routing Exchange Protocol. Several organizations participated in the Cooperative Testing Program. NIST will document the test scenarios and general results of the testing to provide comments to implementors; to guide standards communities in refining base standards, implementors' agreements, and user group profiles; and to solicit reactions on developing testing and evaluation methods. The U.S. Government OSI Profile (FIPS 146-1) provides the blueprint for federal procurement of multivendor, interoperable computer networking products. For information, contact Doug Montgomery, 301/975-3630; dougm@osi.ncsl.nist.gov.

ELECTROMETER DETECTS CHANGE IN CHARGE ONE TEN-THOUSANDTH THE CHARGE OF AN ELECTRON

NIST scientists have designed and constructed an electrometer based on the principles of single-electron counting. The device has an intrinsic

charge sensitivity of one ten-thousandth the charge of an electron, corresponding to an energy sensitivity over a 1 Hz bandwidth of $30 h/2\pi$. The scientists used a recently acquired writing scanning electron microscope to fabricate the electrometer from two very small tunnel junctions connected in series, with a third terminal capacitively coupled to a very small island in between the junctions. Each junction is only about 100 nm on a side. Electric charge applied to the third terminal controls the current-voltage characteristic of the pair of junctions in a manner that is periodic in charge, the period being equal to the electron charge. The operating temperature is nominally 40 mK. The technology offers the possibility of a quantum-based current standard to match the quantum standards for voltage (implemented by Josephson-junction arrays) and resistance (based on the quantized Hall effect).

COHERENT OSCILLATION OF JOSEPHSON-JUNCTION ARRAY DEMONSTRATED FOR FIRST TIME

A NIST scientist has demonstrated coherent oscillation of a 10×10 array of Josephson junctions, voltage tunable from 60 to 210 GHz. The maximum power generated was $0.4 \mu\text{W}$ at 150 GHz. This achievement represents the first successful operation of a phase-locked array having its power output a substantial fraction of that theoretically predicted. The significance of this fraction is that it demonstrates that phase locking among the junctions is nearly perfect. For many loads of practical interest, the resistance of a typical single Josephson junction of about 1Ω results in a very large mismatch in impedance. Coupled with the very low power level developed in a junction, the mismatch severely limits the class of loads that can be used. The new NIST work can be considered as a feasibility demonstration for the potential of larger arrays to develop significant power levels. The capability of the array to be voltage tunable offers a practical source covering frequencies for which alternatives are very expensive and very difficult to construct. For example, such an array could be used as the local oscillator for heterodyne detection. Development of coherent arrays may also provide some elucidation of the basic physics underlying Josephson oscillations. A patent application has been filed.

AUTOMATED SYSTEM DEVELOPED FOR ANALYZING PERFORMANCE OF JOSEPHSON-JUNCTION INTEGRATED CIRCUITS

A NIST scientist has devised and implemented an automated system for evaluating and testing the operation of complex superconducting integrated circuits. The system provides 96 channels that can be connected selectively to pads on a chip under test in response to operator instructions, eight of these connections being made through high-bandwidth (7 GHz) coaxial lines. Each channel incorporates a 12-bit digital-to-analog data converter that permits test currents to be applied in response to a digital control signal and a 12-bit analog-to-digital converter that reads a corresponding voltage. The system is controlled via IEEE-488 bus protocols through a personal computer that can store data from all channels simultaneously and display up to 16 independent waveforms on its monitor. Provision is made to shield the chip under test from electromagnetic noise from the digital components and other sources of noise, such as the power supply. Future plans include the addition of a word generator and a logic analyzer to permit the system to evaluate single-flux-quantum logic circuits.

ALGORITHMS DEVELOPED FOR ESTIMATING PERMITTIVITY AND PERMEABILITY OF MATERIALS

Optimized algorithms for the simultaneous estimation of the permittivity and permeability of materials have been developed by NIST scientists. When used in conjunction with network analyzers, these algorithms provide new methods that can reliably characterize high-permittivity and high-permeability materials over a frequency range of 300 kHz to 18 GHz and that are applicable to both one-port and two-port transmission lines, which serve as specimen holders for the measurements. Former methods required at least two specimens of the material to be evaluated, were limited to a single frequency, and could not measure high-permittivity or high-permeability materials because of multi-mode fields and numerical instabilities in the reduction algorithms. Network analyzers are used to measure scattering parameters of a coaxial transmission line, with and without material specimens in the line. More than one analyzer may be required depending on the frequency range of interest. The algorithms are then used to find the optimal parameter estimates in a system of non-linear equations based on the measurements. A

constrained non-linear optimization procedure forms the basis for the computation of the values of permittivity and permeability.

SONAR TRANSDUCER ARRAY ACCEPTANCE TESTS IN NIST ACOUSTIC ANECHOIC CHAMBER

NIST scientists collaborated with the Naval Underwater Systems Center (NUSC) and its contractors in performing critical (self-noise, cross-talk, etc.) pre-sea-trial acceptance tests of a sophisticated multielement passive sonar system towed transducer array. Such tests are needed to verify the absence of spurious signals which, if present, could lead to false indications of, or failure to detect, distant submarines and ships. NIST staff used the recently enhanced measurement capabilities at very low signal levels with extremely low-noise, high-sensitivity accelerometers and microphones to demonstrate that the interior of the large acoustic anechoic chamber at NIST is much quieter than sea state zero, is relatively vibration-free, and is, therefore, well-suited for the pre-sea-trial tests. These tests were so convenient and revelatory of subtle aspects of system performance that similar tests at NIST on another array of a different design will be performed.

RADIATION DOSIMETRY FOR ISOTACTIC NEUROSURGERY WITH THE LEKSELL "GAMMA-KNIFE"

A collaboration between NIST and three clinical radiation oncology centers has resulted in an improved treatment planning procedure involving radiochromic film dose mapping with high spatial resolution. It introduces a relatively new method of treating deep-seated intracranial lesions using a non-invasive technique by focusing an array of 201 gamma-ray beams from a helmet fitted to the patient. This device, now in use in several medical centers in the United States, has been called the Leksell "Gamma-Knife," after its inventor, the Swedish neurosurgeon Lars Leksell. A vital step in the procedure is the accurate and precise mapping of radiation dose distributions in a skull phantom immediately prior to radiation treatment of the patient. Two NIST scientists have pioneered the use of radiochromic films for dosimetry and clinical radiography of radiation therapy sources and are co-authors of a paper on the Gamma-Knife with other medical physicists. The paper was presented at the 1991 annual meeting of the American Association for Physics in Medicine.

MODELING OF MAGNETOCALORIC EFFECT IN NANOCOMPOSITES

NIST scientists have developed the theory and written computer programs to model the magnetocaloric effect over a wide range of magnetic fields and temperatures for two types of nanocomposites: (1) those containing non-interacting superparamagnetic nanoclusters, and (2) those in which the nanoclusters are ferromagnetically interacting. The calculations demonstrate that superparamagnetic materials offer the possibility of extending the upper useful temperature limit of paramagnetic materials for low-temperature magnetic refrigeration, such as might be needed for cooling the new high-temperature superconductors. The calculations for the ferromagnetically interacting superparamagnetic materials are carried out using both mean-field theory and Monte Carlo simulations, and demonstrate that interacting superparamagnetic clusters can give significant magnetocaloric cooling over large temperature ranges, with potential implications for room-temperature magnetic refrigeration. The results of the modeling are being used for guidance in the development of appropriate nanocomposite materials.

RESEARCH SUPPORTS THE DEPARTMENT OF DEFENSE (DoD) COMPUTER-AIDED ACQUISITION AND LOGISTIC SUPPORT (CALs) PROGRAM

Three new publications document NIST's continuing technical assistance to the DoD CALs program. NISTIR 4494, SQL3 Support for CALs Applications, focuses on Structured Query Language (SQL) 3, a planned standard for major new SQL enhancements which is expected to be adopted as a national, international, and federal standard in the mid-1990s. NISTIR 4524, Raster Graphics Conformance Testing, evaluates the alternatives for identifying and selecting a conformance testing laboratory for raster graphics in support of CALs. NISTIR 4547, A Standard Generalized Markup Language Encoding of the Office Document Architecture Document Application Profile, describes NIST's encoding of the Office Document Architecture Document Application Profile in the Standard General Markup Language to illustrate similarities between the two international standards in support of CALs.

Standard Reference Materials

MELT FLOW RATE STANDARD AVAILABLE FOR POLYMERS

Researchers now have a better way to calibrate and evaluate the performance of instruments to measure the melt flow rate of polymer materials. Standard Reference Material (SRM) 1474, Polyethylene Resin, is certified for melt flow rate using procedure A in Section 8 of ASTM Method D 1238-86. SRM 1474 is supplied as white pellets of polyethylene in a 60-gram unit. Available for \$211 per unit from the Standard Reference Materials Program, Rm. 204 Building 202, NIST, Gaithersburg, MD 20899, 301/975-6776, fax: 301/948-3730.

THIN-FILM DEPTH PROFILE STANDARD AVAILABLE

Manufacturers have a new calibration tool for determining the sputtered depths and sputter erosion rates in the surface analysis of materials on semiconductors and other substrates. The calibrated structure of Standard Reference Material (SRM) 2136, Chromium/Chromium-Oxide Marker Layer, Thin-Film Depth Profile Standard, is useful for verifying correct instrument operation, monitoring ion beam current-density stability, and producing sputtering conditions that achieve maximum interface resolution. The SRM consists of eight chromium thin-film layers on a polished silicon substrate; each interface is composed of a thin chromium oxide layer estimated to be 2 to 3 monolayers thick. The seven outermost chromium layer thicknesses are certified; the thickness of each layer is nominally 30 nm. Available for \$673 from the Standard Reference Materials Program, Room 204 Building 202, NIST, Gaithersburg, MD 20899, 301/975-6776, fax: 301/948-3730.

NEW STANDARDS CAN IMPROVE MEDICAL LAB ACCURACY

A decade after it was introduced, NIST scientists are issuing an improved version of one of medicine's most popular standard reference materials. The 10 year-old SRM, an extremely accurate yardstick for measuring cholesterol, glucose, sodium, potassium and other constituents in blood, is being replaced with an expanded set of samples to increase the reliability of laboratory test results. The new set of reference materials contains six vials of freeze-dried human serum, three with

normal levels of organic and inorganic compounds, and three with elevated levels. The original set contained only normal levels. The new SRM allows labs and equipment manufacturers to calibrate their instruments at two points rather than one. It was developed with input from the College of American Pathologists and the clinical laboratory community. SRM 909a is available for \$179 from the Standard Reference Materials Program, Building 202, Room 204, NIST, Gaithersburg, MD 20899; phone: (301) 975-6776.

NEWEST BOTANICAL STANDARDS ARE “JUST PEACHY”

Apples and peaches may make great pies, but NIST scientists favored the leaves for two new botanical Standard Reference Materials (SRMs). Ground apple and peach leaf samples will help analytical laboratories around the world improve the accuracy and reliability of their results. NIST scientists pulverized leaves from Georgia peach groves and Pennsylvania apple orchards to a fine powder and then analyzed their content of 20 chemical elements, such as aluminum, arsenic, mercury, and lead. The new SRMs were designed for laboratories that regularly measure plant samples, agricultural products, living tissues, or similar biological compounds. Laboratories use the SRMs, which come with certified chemical composition values, as control samples and to evaluate the reliability of their methods. The apple leaf SRM (1515) and peach leaf SRM (1547) are available for \$174 each from the Standard Reference Materials Program, Room 204 Building 202, NIST, Gaithersburg, MD 20899, 301/975-6776.

COMMON COMMERCIAL ASBESTOS STANDARD, SRM 1866a

The Standard Reference Materials Program announces the renewal certification of SRM 1866a, Common Commercial Asbestos. This NIST certified SRM consists of a set of three common bulk mine-grade asbestos materials and one synthetic glass fiber sample. The three asbestos types in the SRM set are chrysotile, grunerite (Amosite), and riebeckite (crocidolite) and are typical of the asbestos found in bulk samples during routine asbestos inspections of building materials. The glass fiber sample serves as non-asbestos-containing material (blank) to check for contamination that would affect the accuracy and limits of detection of asbestos analyses. The optical properties of this SRM were characterized by light microscopy so that it may serve as a primary

calibration standard in the identification of asbestos.

These samples will be particularly useful to laboratories involved in the National Voluntary Laboratory Accreditation Program Bulk Asbestos Analysis Accreditation Program for developing and evaluating techniques for identifying the various types of asbestos commonly found in building materials.

TRACE ELEMENTS IN WATER, SRM 1643c

The Standard Reference Materials Program announces the renewal certification of 1643c, Trace Elements in Water. The SRM, certified by NIST, is intended primarily for use in evaluating the accuracy of trace element determinations in filtered and acidified fresh water and in calibrating instruments used for making these determinations. This SRM consists of 500 mL of water in a polyethylene bottle that simulates the elemental compositions of fresh water. It is certified for 24 elements at the trace level, including most of the elements listed on the U.S. Environmental Protection Agency (USEPA) toxic substance list. The determination of trace constituents in a simple matrix such as water at the 10^{-9} g level is very difficult. This SRM is required to provide comparability of measurements made by the USEPA, regulatory agencies (state and local), and industrial laboratories. SRM 1643c also can be used in baseline studies to determine whether a fresh water aquatic environment has been degraded.